A Study of the Normal Injection of Hydrogen into a Heated Supersonic Flow Using Planar Laser-Induced Fluorescence

by

Andrew D. Rothstein

B.S., Massachusetts Institute of Technology (1991)

Submitted to the Department of Aeronautical and Astronautical Engineering
in partial fulfillment of the requirements for the degree of

Master of Science

at the

MASSACHUSETTS INSTITUTE OF TECHNOLOGY

February 1992

Signature of Author .....
Department of Aeronautical and Astronautical Engineering
January 17, 1992

Certified by .....
Professor Manuel Martinez-Sanchez
Thesis Supervisor (MIT)

Certified by .....
Dr. Paul J. Wantuck
Thesis Supervisor (Los Alamos National Laboratory)

Accepted by .....
Professor Harold Y. Wachman
Chairman, Department Graduate Committee

A Study of the Normal Injection of Hydrogen into a Heated Supersonic Flow Using Planar Laser-Induced Fluorescence

by

Andrew D. Rothstein

Submitted to the Department of Aeronautical and Astronautical Engineering
on January 17, 1992, in partial fulfillment of the
requirements for the degree of
Master of Science

Abstract

A sonic, highly under-expanded, jet of hydrogen was injected transversely into a supersonic (Mach 1.5), high-temperature (static temperature $\approx$1400 K) argon-oxygen free stream. Laser-based diagnostics were utilized to non-intrusively probe the combustion of oxygen-hydrogen. Planar laser-induced fluorescence (PLIF) was used to image the flow. The images were used to determine both H_2 jet penetration depth profiles and two-dimensional temperature maps of the combustion region. The hydroxyl radical (OH) was used as the PLIF target species in the flow because it is an important and prominent intermediary of the hydrogen-oxygen combustion reaction and it has many strong ro-vibrational lines suitable for laser excitation. The very short gate width of the camera used ($\approx$30 nsec) results in images that are well resolved temporally. Good spatial resolution (51 $\times$ 22 μm) was achieved with a uv-intensified CCD camera and suitable optics.

Jet boundary penetrations are measured for a range of injection (450-1000 torr) and free stream (12-55 torr) pressures. The primary parameter that determines the jet trajectory is the ratio of the dynamic pressures of the jet to the free stream, labeled q. Previous experiments dealt with values of q on the order of one, but this study involves values between 5.9 and 38.6. The penetration profiles are compared where appropriate to previous results for both reacting and nonreacting flows. Despite the large extrapolation, reasonable agreement between the results established in the present study and those of other investigators is found.

Two different equation forms were used in an attempt to empirically relate the jet pemetration, y, to the downstream distance, x, in a manner that holds true for all values of q. The two equations were found to be, $y/d = 2.173q^{0.276}(x/d)^{0.281}$, and $y/d = q^{0.312}ln(4.704[(x/d) + 0.637])$.

The temperature maps calculated in this study show temperatures in the reacting shear layer that range from 880 K up to 2600 K. The shear layer between the hydrogen jet and the free stream burns as the injected jet is turned, and then it cools, extinguishing combustion in a short section. Further downstream, the jet re-ignites and temperatures rise again. This type of structure has been predicted by computer calculations.

Thesis Supervisor (MIT): Professor Manuel Martinez-Sanchez

Thesis Supervisor (Los Alamos National Laboratory): Dr. Paul J. Wantuck

Contents

List of Figures

List of Tables

Acknowledgments

The author would like to thank both David Gallegos and Paul Wantuck, comprising the Aerochemistry Laboratory at Los Alamos National Laboratory, for their help in every aspect of this thesis. And Andrew Sappey's expertise in spectroscopy and laser hardware was invaluable.

Because the research for this thesis was done at Los Alamos National Lab, I am indebted to all of the people who administer the internship program: Professor Ballinger from MIT, Mary Anne With from the Los Alamos Special Employment Group, William H. Ramsey, the director of the program at MIT, and Jay Elson and John Ruminer who help coordinate the program from Los Alamos .

The author is also grateful to Professor Martinez-Sanchez for his long distance guidance, and to the Communications Groups of the Chemical and Laser Sciences division of Los Alamos National Lab for their help in putting this thesis on paper.

List of Symbols

A Cross sectional area of jet element

A_{ij} Einstein A coefficient

A_e Exit area of supersonic nozzle

A^* Throat area of supersonic nozzle

a Adjustable parameter in empirical relations

B_{ij} Einstein B coefficient

b Adjustable parameter in empirical relations

b_{ij} Einstein B coefficient multiplied by the laser intensity

C Constant

C_1 Constant

C_2 Constant

C_D Drag coefficient of a jet element

c Adjustable parameter in empirical relations

D_j Local thickness of jet

D (in graphs) injector orifice diameter

d_i Diameter of injector orifice

E_i Energy of level i

F Normal force acting on a jet element

f Fractional population function

g_i Degeneracy of level i

h Local width of the injected jet

I Current

I_ν Laser intensity

I_ν^{sat} Saturation laser intensity

i Labels a ro-vibrational state

j_i Total angular momentum of level i

k Boltzmann constant

L Length of gas feed line

M_a Mach number of free stream

M_i Mach number of injected jet

m Adjustable parameter in empirical equation

m_j Mass of jet element

N_i Number density in level i in the four-level model

N_P Number of photons recorded by detector

n Adjustable parameter in empirical equation

n_i Population number density in energy level i

P Pressure

ΔP Pressure drop along gas feed line

$\Delta \bar{P}$ Average pressure difference between the two faces of a jet element

P_{FS} Free stream pressures used in present study

P_{H2} Hydrogen injection pressures used in present study

p Dynamic pressure

Q Volumetric gas flow

Q_{ij} Quenching rates

q Dynamic pressure ratio

q_i Relative line strength from transition labeled i

R Ratio of fluorescence signals

R_c Radius of curvature of jet trajectory

R_g Radius of gas feed line

R_R Resistance

R_{ij} Rotational energy transfer rate coefficient

R_{ij}^T Overall rate coefficient

s Arc length of jet trajectory path

$\bar{s}$ Arc length of jet trajectory normalized by d_i

s_m Arc length of jet trajectory from injector to the Mach disk

T Temperature

T_{ij} Downward transfer rates

t Time

V_c Collection Volume

v Velocity of jet element

v_i Relative velocity between two species in a gas

x Downstream distance measured from injector orifice

x_0 Downstream location of Mach disk

y Distance measured vertically from injector orifice

y_0 Vertical distance to Mach disk

α Local angle of inclination of jet element

γ Specific heat ratio

η Transmission efficiency of collection optics

ρ_a Gas density in free stream

ρ_i Gas density of injected gas at injector orifice

σ_i Collisional quenching cross section of species i

μ Gas viscosity

χ_m Mole fraction

Ω Collection solid angle

Chapter 1

Introduction

The recent push towards the development of aircraft capable of hypervelocity flight [*e.g.* the National Aerospace Plane (NASP)] has once again stimulated research into supersonic, air breathing ramjet (scramjet) engines. A simple schematic of such an engine is diagrammed in Figure 1-1 (on page 2). The air inlet is generally made up of a series of wedges so that the shock system produced slows and compresses the air. Downstream of the wedges, both parallel and transverse[1] fuel injectors are use to maximize mixing (and hence combustion efficiency) throughout the entire flight regime. The ingested air stream is still supersonic, and hence it has a very short residence time in the expansion section of the engine. To maximize efficiency, optimizing the fuel-air mixing is crucial. This study examines the normal injection of a fuel into a supersonic free stream.

Understanding the fundamental physical processes that govern the mixing and the combustion of the fuel, typically hydrogen, and air at such conditions is critical for efficient engine design. With such engines the fuel and air stream move and intermix at supersonic speeds. Computational modeling of the mixing and reaction phenomena has been done, but the experimental data base to support these computational fluid dynamics (CFD) codes' predictions remains limited. NASP is proposed to fly at very high ($\approx$18) Mach numbers through the upper atmosphere. Experimental testing in such regimes is extremely difficult, placing a heavy burden on computational simulations for system design. The extreme reliance on CFD for hypersonic aircraft design mandates a quality experimental database for code validation.

There are two main areas of study that are important to scramjet designs. One can study mixing

[1] Transverse injection is also called normal injection.

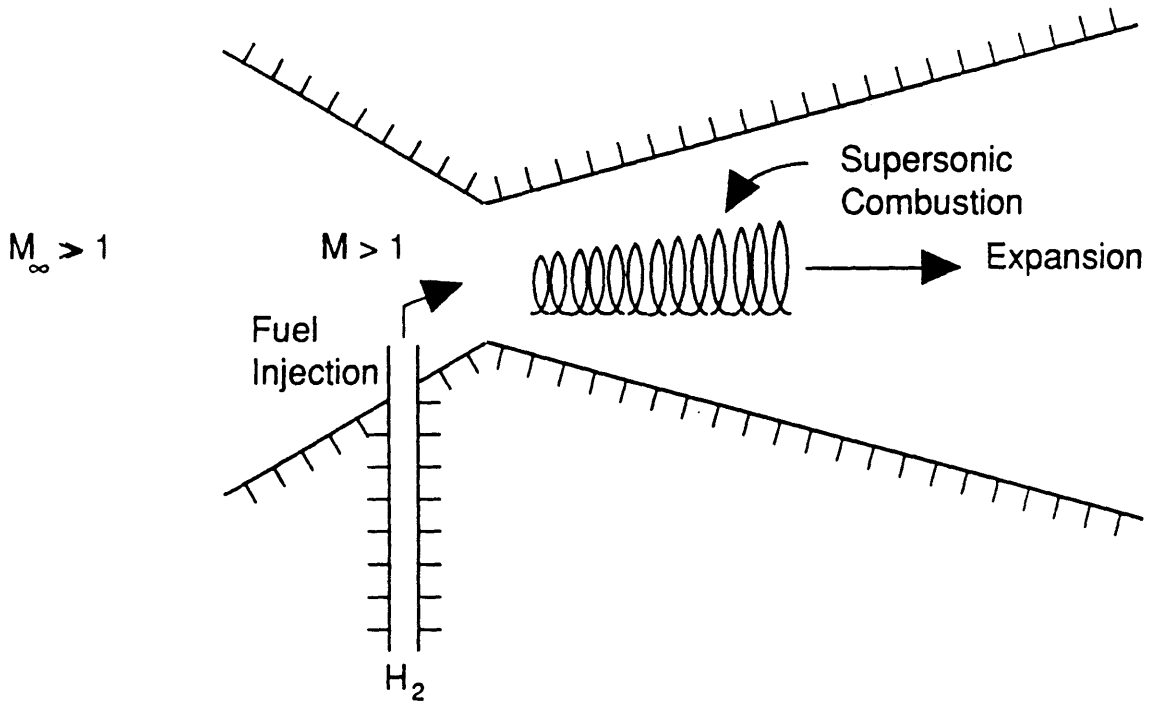

Figure 1-1: Schematic of a Scramjet Engine

phenomena, where the gases are not reacting, or experiments with reacting flows can be examined. The former of these would concentrate on the effects of various injector designs, orientations, and injection pressures on mixing rates. Because of the very short residence time of the combusting gases in the scramjet engine, optimized mixing is essential for maximum engine performance.

The second area, involving reacting flows, is a much more complicated problem. The gases are still mixing, but finite rate chemistry causes non-equilibrium temperatures and species concentrations. The high temperatures in a combustion environment (with typical temperatures above 1000 K), and the importance of very small scale and very fast phenomena, make reacting flows (and especially supersonic, reacting flows) more difficult to probe.

This work examines a supersonic, reacting flow: the transverse injection of hydrogen at sonic speeds into a heated, supersonic free stream comprised of 20% oxygen in argon. The flow characterization goals in this study are to relate the penetration depth of the hydrogen jet into the free stream as a function of injection and free stream pressure, and to map the local, two-dimensional temperature distributions. The jet penetration study is compared to results obtained in both non-reacting flows, which have been widely studied, and reacting flows, where little data exists. The temperature mapping demonstrates the utility of a new, powerful, non-invasive diagnostic technique for supersonic, reacting flow studies.

Planar laser-induced fluorescence (PLIF) was utilized as the primary diagnostic technique for this study. The PLIF technique is ideally suited for the study of high-speed reacting flows because it allows for non-intrusive probing,[2] and the establishment of two dimensional flowfield parameter maps with good spatial ($\approx 50\mu$m) and temporal (≈ 30 nsec) resolutions.

The PLIF technique involves exciting a target molecule or atom present in the flow with a sheet of laser light and imaging the resultant emission pattern. The point-by-point intensity of the fluorescence signal can be used to determine local gasdynamic properties such as species concentration and temperature. The PLIF diagnostic has several advantages over other laser-based techniques. For example, PLIF signals are generally stronger than Raman scattering signals,[1] and because it can use indigenous species as targets, PLIF can avoid the uncertainties in flow tracking involved with using seed particles, such as would be used in laser Doppler velocimetry.

This work uses PLIF to image the fluorescence emitted by hydroxyl radicals produced through the supersonic combustion of oxygen and hydrogen and excited by a sheet of laser light. The images captured give a two dimensional, temporally resolved picture of the relative concentration of the hydroxyl radical, which is then used to measure the jet's penetration into the free stream as well as the temperature field

[2] Classical intrusive probes such as pitot tubes have trouble surviving in the harsh environment: high temperatures and a strongly oxidizing flow stream.

in the reacting flow.

Chapter 2

Background

2.1 Normal Injection

Because of its importance to scramjet operation and thrust vector control of rocket motors, much work has been done on the transverse injection of a sonic or supersonic jet into a supersonic free stream. A typical flowfield for an under-expanded jet being transversely injected into a supersonic free stream is shown in Figure 2-1. As is illustrated there, the under-expanded jet enters the free, or main stream, and is accelerated and bent by the momentum of the free stream. As the jet expands to local pressures, a normal shock or Mach disk is formed. A large amount of research has been done correlating the Mach disk location to various flowfield parameters. Such a correlation is used for this study for the theoretical calculations,[1] but the primary focus is on the location of the reacting shear layer (the region in the flowfield where the hydrogen and oxygen mix and combust) between the jet and the free stream.

The exact shape and structure of the flow pictured in Figure 2-1 is thought to be mainly determined by the Mach number of both streams, the dynamic and total pressures of both streams, and the boundary layer thickness. The effects of these parameters in the injection process are discussed in detail in both the theory and the experimental sections of this chapter.

Primarily three techniques have been used to study the flowfield associated with normal injection. Early studies (typically done in the 1960s and 70s) relied upon schlieren photographs and/or sampling probes, while more recent efforts use PLIF imaging.[2] The schlieren photographs clearly show the shock

[1] The Mach disk location becomes the origin for the theoretical calculations of the jet's penetration.

[2] The imaging aspects of these works are discussed more fully in Section 2.2.4. Here, only the results of their imaging are examined.

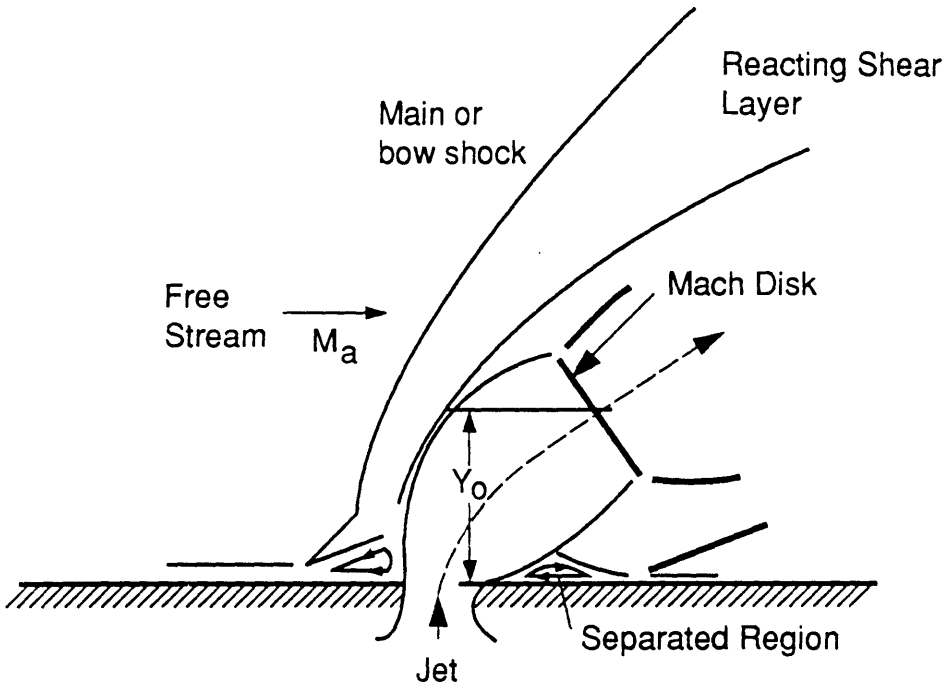

Figure 2-1: Schematic of the Flow Field Around the Injection Orifice for a Typical Under-Expanded Jet

structure (the Mach disk being the one of primary interest) in the flow, whereas the probes are usually not sensitive enough.[3] With PLIF imaging, shock structure such as the Mach disk may not be visible. If the species being imaged is present in the jet fluid, then the Mach disk is typically visible, but if the species represents an intermediary product of the chemical reaction between the two streams (as in this study), then the Mach disk and other shock structure (such as the bow shock) will not be seen.

2.1.1 Cold Flow Theory

Schetz and Billig[2] analyze the trajectory of a supersonic jet entering a supersonic cross flow by modeling the jet as a "solid" body that is bent by drag and distorted by pressure differences. The following analysis is based on their work.

The area of interest for this analysis is the flow is close to the injection port. Here the flow is still being accelerated and bent; and this stage is considered to be separate and distinct from the coaxial turbulent mixing that occurs farther downstream. The following derivation assumes that the jet injection pressure is "matched"[4] with that of the free stream; but it is assumed to hold true for the under-expanded case[5] as well, with the initial conditions becoming the conditions immediately downstream of the shock (the Mach disk), and the location of the Mach disk being superposed on the penetration profile.

Referring to Figure 2-2, consider the forces acting on an infinitesimal trajectory length element ds. First balancing the forces in a direction parallel to the trajectory:

$$m_j \frac{dv}{dt} = \Delta\overline{P}A, \tag{2.1a}$$

where $\Delta\overline{P}$ is the difference in average static pressures acting on the cross section between s and $s+ds$, A is the local cross-sectional area of the jet, and dv/dt is the acceleration of the element. Balancing the forces acting on the element of mass m_j in a direction perpendicular to the trajectory, the normal force is set equal to the centripetal force due to the curvature of the jet's trajectory

$$F = \frac{m_j v^2}{R_c}, \tag{2.1b}$$

where R_c is the radius of curvature of the trajectory. Now dt is related to the distance ds by $dt = ds/v$, and $ds = Rd\alpha$, while $F \equiv C_D p_a sin^2\alpha h ds$, where C_D is the drag coefficient on the element, α is the local angle of inclination of the trajectory, $h = h(s)$ is the local width of the jet, and p_a is defined as the

[3] They are too large to pick up the small scale structure of the Mach disk.

[4] Here, "matched" is defined as the injection pressure that minimizes the shock structure in the flow. A more thorough definition of the matched conditions is given later in this section.

[5] The current study involves a highly under-expanded jet, and so that is the case of interest.

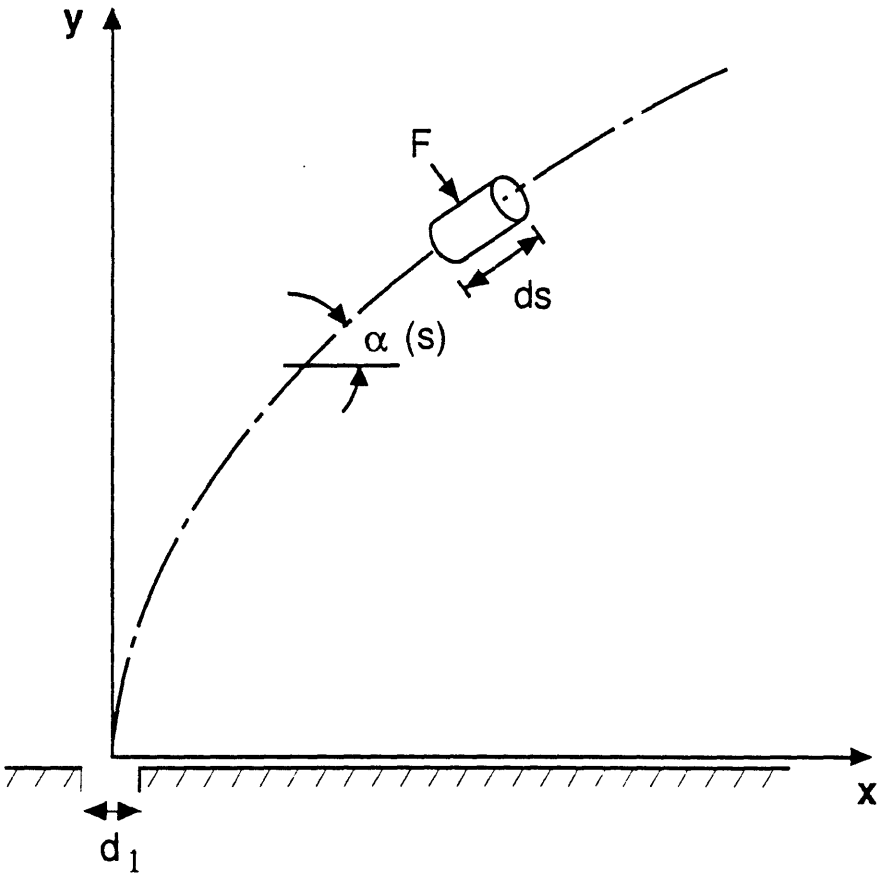

Figure 2-2: Schematic of the Jet Centerline Trajectory

dynamic pressure of the free stream ($p_a \equiv \frac{1}{2}\rho_a v_a^2$). Making these substitutions into Equations. 2.1a and 2.1b yields,

$$\rho v dv = -\Delta\overline{P} \tag{2.2a}$$

$$\frac{d\alpha}{ds} = -\frac{C_D h p_a sin^2\alpha}{\rho v^2 A}. \tag{2.2b}$$

The subscript a denotes values of the variables in the free stream, and variables without subscripts represent local conditions. Now using the fact that the total mass in the jet is conserved we can substitute,

$$v = \frac{\rho_i v_i A_i}{\rho A}, \tag{2.3}$$

where the subscript i denotes the initial conditions of the jet, at the injector orifice for a matched case or just behind the Mach disk for the under-expanded case. Making this substitution into Equation 2.2b, and replacing p_a by its definition gives,

$$\frac{d\alpha}{ds} = -\frac{C_D h \rho_a v_a^2 sin^2\alpha}{2\rho_i^2 A_i^2 v_i^2/\rho A}. \tag{2.4}$$

With v eliminated from Equation 2.2b in this way, Equation 2.2a is not needed if $h(s)$, $A(s)$, $\rho(s)$, and $C_D(s)$ are known. C_D can be determined by assuming that each element acts like a segment of an infinite cylinder aligned at the local angle to the flow. From experimental data,[3] there are simple curve fits for C_D,

$$C_D = 1.2 + (M_a sin\alpha)^{\frac{3}{2}} \qquad 0 \leq M_a sin\alpha \leq 1 \tag{2.5a}$$

$$C_D = 1.06 + 1.14(M_a sin\alpha)^{-3} \qquad M_a sin\alpha \geq 1. \tag{2.5b}$$

By assuming that the width of the jet is comparable to the subsonic case, an empirical formula for $h = h(s)$ has been established by Abramovich,[4]

$$h = 2.25 d_i + 0.22 s, \tag{2.6}$$

where d_i is the diameter of the injection orifice. Abramovich also suggests that the shape of the jet's cross section be taken as an ellipse with major axis length 5 times the minor axis. From this and Equation 2.6, $A(s)$ can be found to be,

$$A(s) = \frac{\pi h^2}{20} \tag{2.7}$$

and,

$$\frac{hA}{A_i^2} = \frac{(2.25 + 0.22\frac{s}{d_i})^3}{2.5\pi d_i}. \tag{2.8}$$

And finally, combining Equations 2.8 and 2.4 results in

$$\frac{d\alpha}{d\bar{s}} = -\frac{C_D(\alpha)sin^2\alpha}{2.5\pi}\left(\frac{\rho_a v_a^2}{\rho_i v_i^2}\right)\left(\frac{\rho}{\rho_i}\right)(2.25 + 0.22\bar{s})^3, \tag{2.9}$$

where $\bar{s} \equiv s/d_i$, and $C_D(\alpha)$ is defined in Equation 2.5a. The only unknown quantity remaining is $\rho(s)$, the local density. For this analysis, ρ will be assumed to remain constant and equal to either its value at the jet orifice for the matched situation, or to that density just downstream of the normal shock for the under-expanded case.[2] The quantity $(\rho_i v_i^2/\rho_a v_a^2)$ will be defined as q, the injection dynamic pressure ratio. A more easily used form of this definition is,

$$q = \frac{\gamma_i P_i M_i^2}{\gamma_a P_a M_a^2}, \tag{2.10}$$

with $M_i = 1$ for the present study. Integrating Equation 2.9 yields

$$0.88(2.5\pi)q\int_{\alpha}^{\frac{\pi}{2}} \frac{d\alpha'}{C_D(\alpha')sin^2(\alpha')} = (0.22\bar{s} + 2.25)^4 - 2.25^4. \tag{2.11}$$

The integral in Equation 2.11 must be evaluated from some value of α of interest to $\alpha_1 = sin^{-1}M_a^{-1}$ using Equation 2.5a (found on page 9) for C_D, and then from α_1 to $\pi/2$ (since the injection is normal to the free stream, the initial α is 90°) using Equation 2.5b.

Table 2.1: Empirical Power Law Equations for Jet Centerline Penetration

Researcher(s)	m	n
Abramovich	1.00	0.392
Abramovich	0.769	0.333
Schetz & Billig	1.00	0.435

Because there had been no supersonic experiments done at matched conditions when Schetz and Billig[2] did their work, they initially had to look to subsonic data to substantiate their theoretical work[6]. Abramovich[4] established the power law equation,

$$\frac{y}{d_i} = q^m\left(\frac{x}{d_i}\right)^n, \tag{2.12}$$

[6] Later they conducted their own experimental investigation with Orth.[5]

where m and n are adjustable parameters, as providing a suitable empirical fit for the centerline trajectory data for a transversely injected gas into a subsonic free stream.

Abramovich found two separate fits using this equation. Schetz and Billig used this equation to fit their theoretical predictions. Their results as well as those of Abramovich are summarized in Table 2.1. The similarity between their values of m and n and those found by Abramovich supports their theory.

In a direct comparison of their theory and subsonic injection data, Scheta and Billig found that the predictions of the centerline trajectory where about 40% lower than the experimental data for a high value of q ($q = 16.35$). The graph they made of their theory and two subsonic cases is shown in Figure 2-3 on page 12.

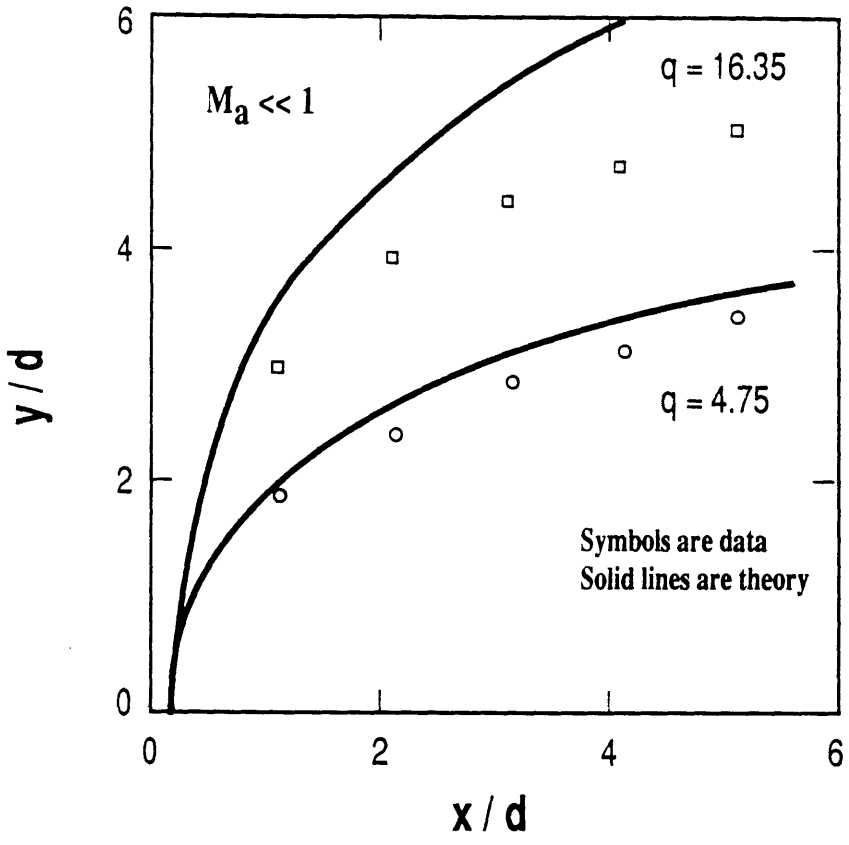

Figure 2-3: Comparison of Theory (Schetz and Billig) to Subsonic Experiments (Reference 2)

In a later paper, Billig *et al.*[6] report a relation for the total thickness of the jet, D_j. The jet penetration boundary can then be computed by adding this thickness to the centerline trajectory (as calculated from Equation 2.11). The relation they found for D is,

$$D_j = D_{j2}\left[1 + 1.45ln\left(\frac{p_{eb}}{p_a}\right)\left(1 - \epsilon xp\left[-0.322\frac{s - s_2}{D_{j2}}\right]\right)\right], \tag{2.13}$$

where the subscripts 2 refer to conditions at the Mach disk, and p_{eb} is the effective back pressure that the jet encounters in the free stream. Effective back pressure is a concept introduced by Schetz and Billig[2] to model the complex pressure field around the jet as it exits the jet orifice. For the case of a jet entering a quiescent medium, the governing parameter for the penetration is the ratio of the jet pressure, P_i, to the back pressure, P_b. For the case of a flowing medium, an effective back pressure, P_{eb}, must be defined. If the emerging jet is viewed as a roughly cylindrical obstacle to the main flow, then the static pressure distribution around the periphery of the jet would be expected to vary from a maximum at the forward stagnation point (equal to the pressure behind the normal bow shock in front of the jet, P_t) to a low in the region behind the jet. P_{eb} is defined as the value of the jet injection pressure at which the shock structure in the flow is minimized (the pressure matched case). Two different equations for P_{eb} have been used in the past. Using the results of two different studies, Schetz[7,8] found $P_{eb} = 0.80P_t$ to be a satisfactory fit to the data, while Billig *et al.*[6] used $P_{eb} = \frac{2}{3}P_t$. But as Billig points out, the difference between calculated jet trajectories done using the two definitions is trivial (less than 8%) for most cases of interest. For this paper, $P_{eb} = \frac{2}{3}P_t$ has been used.

To calculate the jet boundary, the dynamic pressure ratio, q, behind the Mach disk is needed. Such a determination can be done by using the normal isentropic shock relations to find a new P_i, and then using the following relation,

$$\frac{s_m}{d_i} = M_i^{1/(\gamma-1)}\left[\left(\frac{\gamma - 1}{2}\right)^{\gamma/(\gamma-1)}\left(\frac{\gamma + 1}{4.8\gamma}\right)\right]^{-\frac{1}{2}}, \tag{2.14}$$

(derived from a combination of theory and experiment by Crist *et al.*[9] for the case of a sonic jet issuing into a quiescent medium) to calculate the Mach number, M_i, just behind the shock. In Equation 2.14, γ is the ratio of specific heats for the injected gas, and s_m is the trajectory's arc length to the Mach disk, assumed to be,

$$s_m = \left(x_0^2 + y_0^2\right)^{\frac{1}{2}}, \tag{2.15}$$

where x_0 and y_0 locate the Mach disk relative to the injector orifice.

Equation 2.11 was solved iteratively, decreasing α on each iteration so that a curve of the penetration boundary could be traced out. At each point, s was calculated and used in Equation 2.13 to find D. The

x and y components of D_j (which is a thickness measured normal to the trajectory) were then added to the old x and y to arrive at a new boundary position. The results of that calculation, with $M_a = 1.5$, $P_i = 700$ torr, $P_{eb} = 44$ torr, a typical case for the present investigation, is shown in Figure 2-4.[7]

As is seen in Figure 2-4, the trajectory does not begin at the injector orifice, but at the Mach disk location. The origin of the trajectory is given by the empirical relations[8,10] (for sonic injection),

$$\frac{y_0}{d_i} = \sqrt{\frac{P_i}{P_{eb}}} \tag{2.16a}$$

$$\frac{y_0}{x_0} = 1, \tag{2.16b}$$

where P_i is the jet pressure. As predicted by Schetz *et al.* (References 7 and 8), the under-expanded flowfield is characterized by a rapid penetration to the Mach disk, and then a more gradual penetration (since the value of q is much lower behind the Mach disk) as the jet continues downstream. For an under-expanded jet (as for the experiments in this work), the initial conditions need to be set to the conditions immediately downstream of the Mach disk, and the location of the Mach disk is used as an offset.

2.1.2 Cold Flow Experiments

Most of the previous experiments done on the transverse injection of a gas into a supersonic free stream have used the height of the Mach disk as their measure of penetration depth,[7,8,11,12] primarily because the visualization method used, schlieren photography, is well suited for viewing shock structure. For those works that do plot jet boundary penetrations, two different forms of empirical relations are used to fit the measured penetration trajectories. The first and most common form relates the downstream distance to the penetration height by a power law of the form,

$$\frac{y}{d_i} = aq^b \left(\frac{x}{d_i}\right)^c. \tag{2.17}$$

The form of this equation was determined mainly by a non-dimensionalization of the normal injection problem. Researchers investigated the effect of various ratios (free stream to injection parameters such as Mach number, dynamic and total pressures, and densities for example) on the penetration of jets, and they found that most flow parameters had little or no effect. The dynamic pressure ratio was the most important quatity, an hence they were left with Equation 2.17.

[7] In this figure, and in subsequent gra s, the axis represent distances normalized by the jet orifice diameter. In the figures, the symbol d_i (for the orifice diameter) is replaced by D.

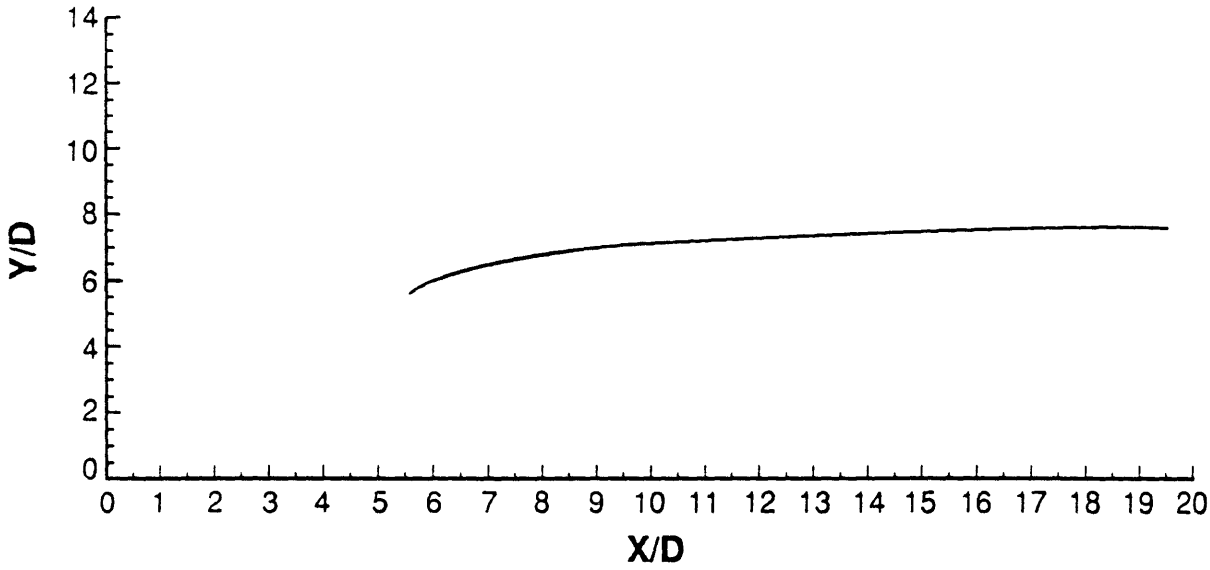

Figure 2-4: Theoretical Jet Penetration Boundary Trajectory Calculated Using Equation 2.11

Vranos and Nolan[13] used this form to fit data for normal injection of a helium-air mixture into a supersonic air stream. The best fit was established with the relation (for $M_a = 1.5$ and $M_i = 1$)

$$\frac{y}{d_i} = 1.68q^{0.5}\left(\frac{x}{d_i}\right)^{0.0866} . \tag{2.18}$$

Rogers[14] used a sampling probe to measure the penetration of hydrogen injected normally into a supersonic, cold airstream. He found his data could be matched quite well using Equation 2.17 with different values of a, b, and c, namely,

$$\frac{y}{d_i} = 3.87q^{0.30}\left(\frac{x}{d_i}\right)^{0.143} . \tag{2.19}$$

Faucher *et al.*[18] performed a series of experiments similar that those done by Vranos and Nolan. They injected a "simulated" fuel (meaning that an inert substance of equal molecular weight to a real fuel) was injected transversely into a cold free stream (with free stream Mach numbers ranging from 1.6 to 3.0). They used a sampling probe to study the penetration of the injected jet. The values of dynamic pressure ratio at which they took data ranged from 0.87 to 5.87, and they only examined the flowfield far downstream from the injector orifice ($14 < \frac{x}{d} < 150$). The empirical relation that fit their data optimally was,

$$\frac{y}{d_i} = 1.446q^{0.392}\left(\frac{M_a}{M_i}\right)^{0.613}\left(\frac{x}{d_i}\right)^{0.0396+0.379M_i/M_a} . \tag{2.20}$$

For the Mach numbers employed for the present study ($M_a = 1.5$ and $M_i = 1$), this equation becomes,

$$\frac{y}{d_i} = 1.854q^{0.392}\left(\frac{x}{d_i}\right)^{0.292} . \tag{2.21}$$

Orth, Schetz, and Billig[5] use Vranos and Nolan's work to both validate their theory and to fit their experimental data. Equation 2.18 (Vranos and Nolan's empirical equation), the theory Schetz and Billig put forth in References 2 and 6, and the data Orth *et al.* took using a sampling probe all fall within 10% of each other.

McDaniel and Graves[15] used PLIF imaging of seeded iodine to measure jet penetration into an M_a=2.07 air stream. They found that their data was predicted using Equation 2.17 far downstream (x/d>10) from the injector orifice, but that there existed a substantial difference between their data and the equation in the near field. They established their own empirical relation to fit their data. This relation is of the form,

$$\frac{y}{d_i} = q^a ln\left[b\left(\frac{x}{d_i} + c\right)\right] , \tag{2.22}$$

where for the McDaniel and Graves data the three constants are: $a = 0.344$, $b = 2.077$, *and* $c = 2.059$.

Recently, Papamoschou *et al.*[16] used schlieren photography to visualize a normal injection flowfield. They concluded that the dynamic pressure ratio, q, is the dominant parameter governing jet penetration, but it is by no means the only one. They point out that four other quantities could influence the penetration of a gas into a supersonic stream. They are: the injection and the free stream Mach numbers, the total pressure ratio at the injector orifice, and the density ratio at the orifice. In their experiment they varied one of these five variables, and held the others fixed. They found that neither the density ratio nor the injection Mach number had any noticeable effect on the jet penetration, but changes in the free stream Mach number or the total pressure ratio (both with the dynamic pressure ratio held constant) did affect the penetration.

Papamoschou *et al.* compared their result to subsonic scaling laws. In a similar, but subsonic flow, the jet boundary profile is given by,[17]

$$\frac{y}{d_i} = aq^{1/3}\left(\frac{x}{d_i}\right)^{1/3}, \tag{2.23}$$

with $a = 2.2$. They solved this equation for a; and for the various values of q that they used (ranging between 1.5 and 7), they found a to range between 1.5 and 2.3, with a mean of approximately 2.

The different equations that were presented in this section are plotted in Figure 2-5, for q=13. One reason that the trajectories in Figure 2-5 are different is that each research team found empirical constants that allow the curves fit their data; *i.e.*, each curve represents fits to different values of q, M_a, *and* M_i. Although q is identical in each of these plots, the conditions of each investigator's experiment are different. In addition, Papamoschou has shown that q is not the only parameter which governs the dependence between y/d and x/d.

Table 2.2 summarizes the results of empirical fits to various transverse injection data. The first entry in the table is for subsonic data, and the last three are for supersonic experiments. The numbers in the table show a large variation, and this could be because of unaccounted for variables (such as boundary layer size and those examined by Papamoschou).

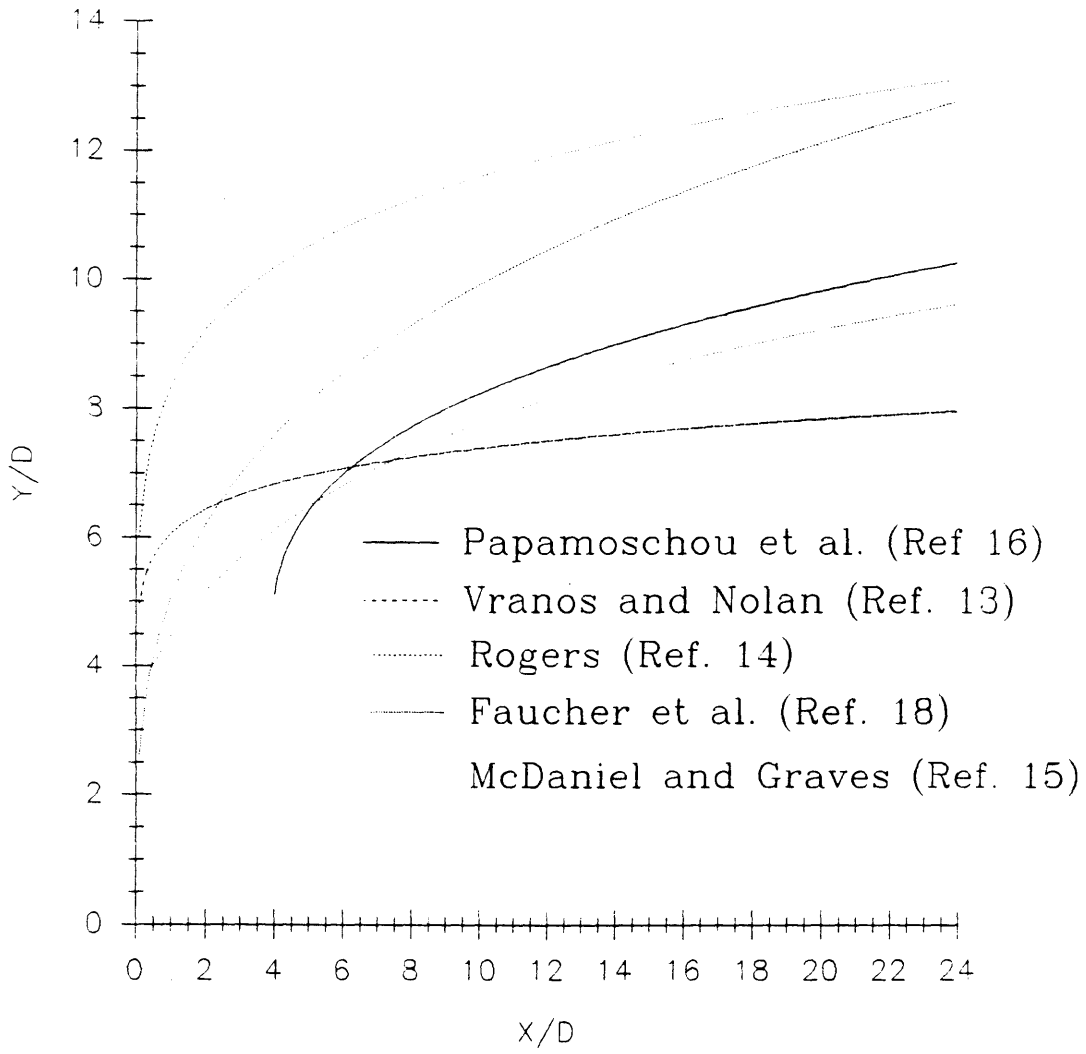

Figure 2-5: Empirical Jet Penetration Boundaries of Various Researchers

Table 2.2: Empirical Power Law Equations for Jet Penetration

Researcher(s)	a	b	c
Broadwell & Breidenthal[17]	2.200	0.333	0.333
Vranos and Nolan[13]	1.608	0.500	0.087
Rogers[14]	3.870	0.300	0.143
Faucher *et al.*[18]	1.854	0.392	0.292

2.1.3 Hot Flow Experiments

Many experiments have been done on various aspects of supersonic combustion, but studies of jet boundary penetrations for reacting flows are scarce. Wilhelmi *et al.*[19] and Bier *et al.*[20] have done work on the normal injection of hydrogen into a supersonic, hot air stream. Using schlieren photographs to study the shock structure and water-cooled sampling probes to measure jet penetrations (at $q \approx 5$), they defined the outer boundary of the jet to be the point where the injectant mole fraction was 1 percent, and their result is plotted in Figure 2-6.

Recently, Lee *et al.*[21] utilized PLIF imaging of OH to image the combustion of an under-expanded hydrogen jet ($q = 2.1$) in a shock tube flow. They found that the penetration of the hydrogen was less than that for nonreacting flows. The smaller depth of penetration is thought to be due to the consumption of H_2 through combustion. Their jet penetration data, and their comparison to the results of McDaniel and Graves[15] is presented in Figure 2-7 (page 22). With $q = 2.1$ in Equation 2.22 (McDaniel and Graves' empirical fit), Lee *et al.*'s data and the empirical predictions are similar.

2.1.4 Hot Flow Numerical Simulations of Transverse Injection into a Supersonic Stream

Typically with the numerical studies done on transverse injection of a fuel into a supersonic oxidizing free stream,[22,23] correlations (*ie.* empirical relations) for calculating jet boundary penetrations are not given. From the concentration contours presented in such studies, however, an estimate of the jet penetration trajectory can be found. One such contour plot produced by Takahshi and Hayashi[22] is shown in Figure 2-8 (on page 23). This plot is for a jet issuing from a slot injector (with $q = 4.2$), which may change the jet penetration close to the injector orifice, but this flowfield and the flow caused by normal injection from a circular injector should be the same in the far field.

Takahshi and Hayashi also computed temperature profiles for their injection from a slot. Their plot is shown in Figure 2-9 (on page 24). The slot injection scheme causes the jet to effectively "stop" the free stream more than injection from a hole does. And so immediately behind the injection slot, the temperature rises very sharply, as the free stream is brought almost to stagnation conditions there. It is also noted that the temperature rises as the jet turns in the flow, but then the combustion rate in the shear layer decreases (as the temperature drops to 1200 K), then heats up again, eventually to 2000 K.

From Reference 23, a computed concentration contour of 0.5% H_2 concentration with laminar flow (and $q = 1$) is shown in Figure 2-10. This plot has been shifted so that its (0,0) point becomes $y/d = x/d = 5.56$ to account for the fact that their calculations were done with "matched" conditions.

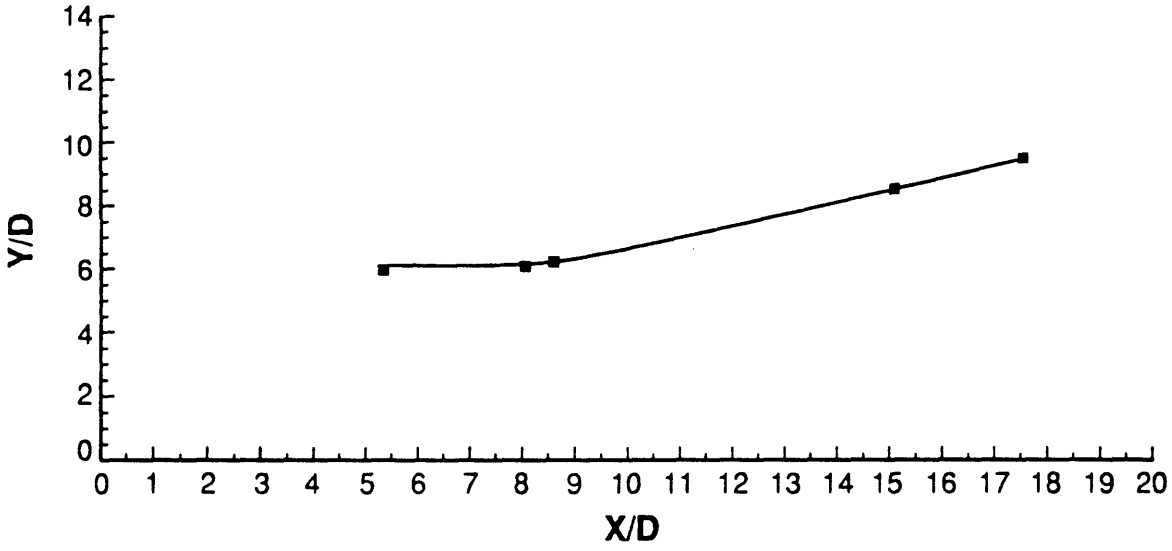

Figure 2-6: Empirical Combusting Jet Boundary (Reference 19)

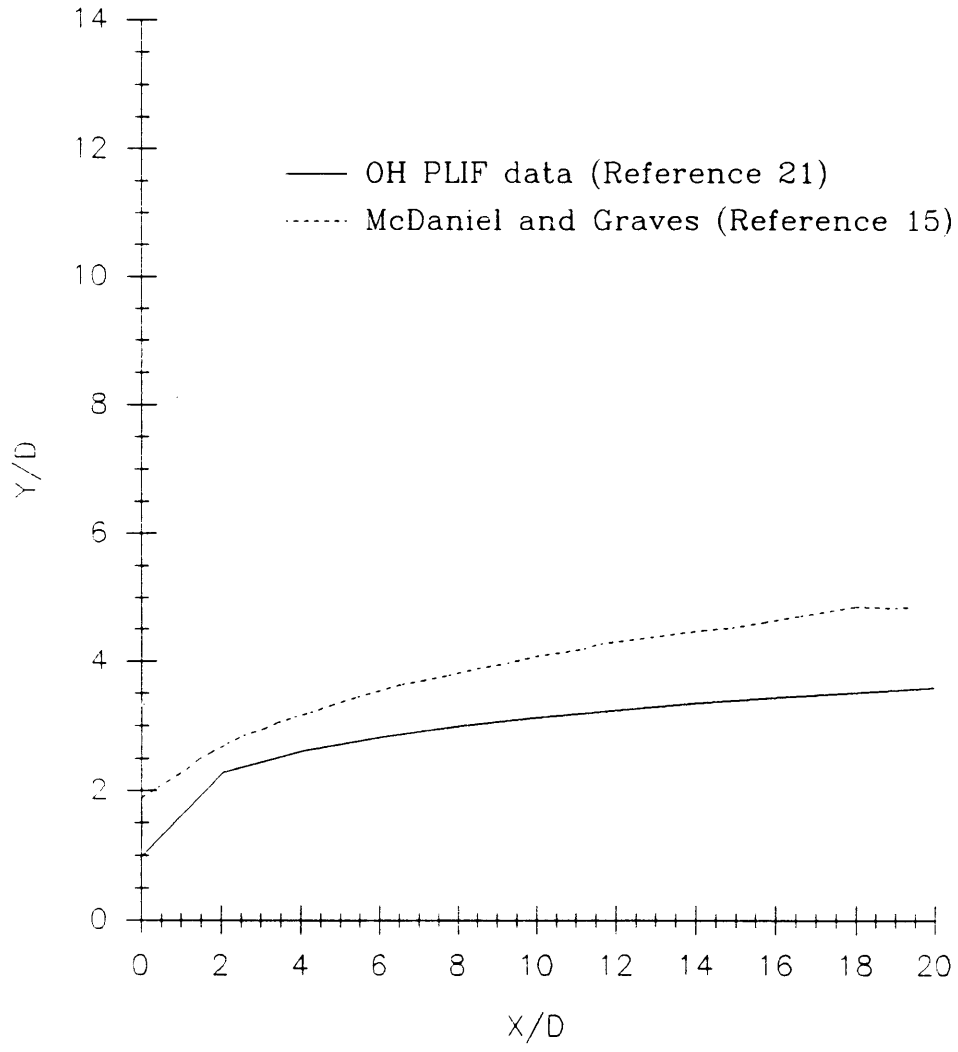

Figure 2-7: Jet Boundary Measured using PLIF on the Hydroxyl Radical (Reference 21)

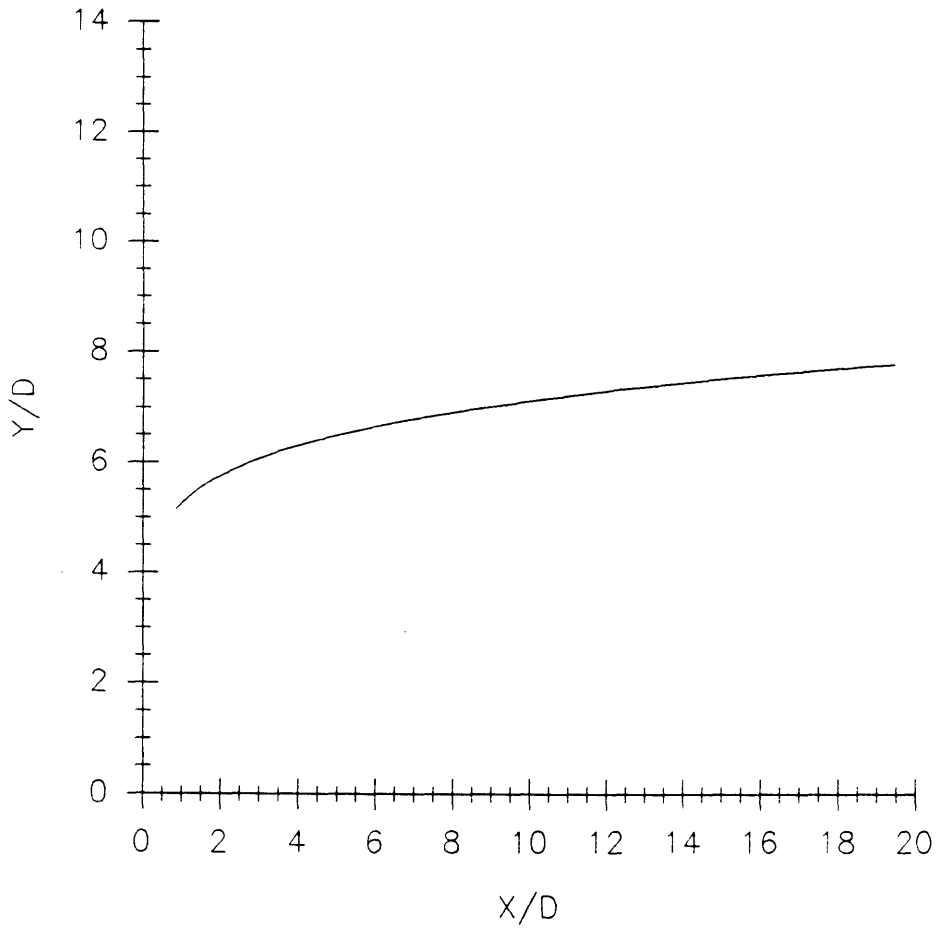

Figure 2-8: Computed 10^{-4} Mole Fraction Contour (Reference 22)

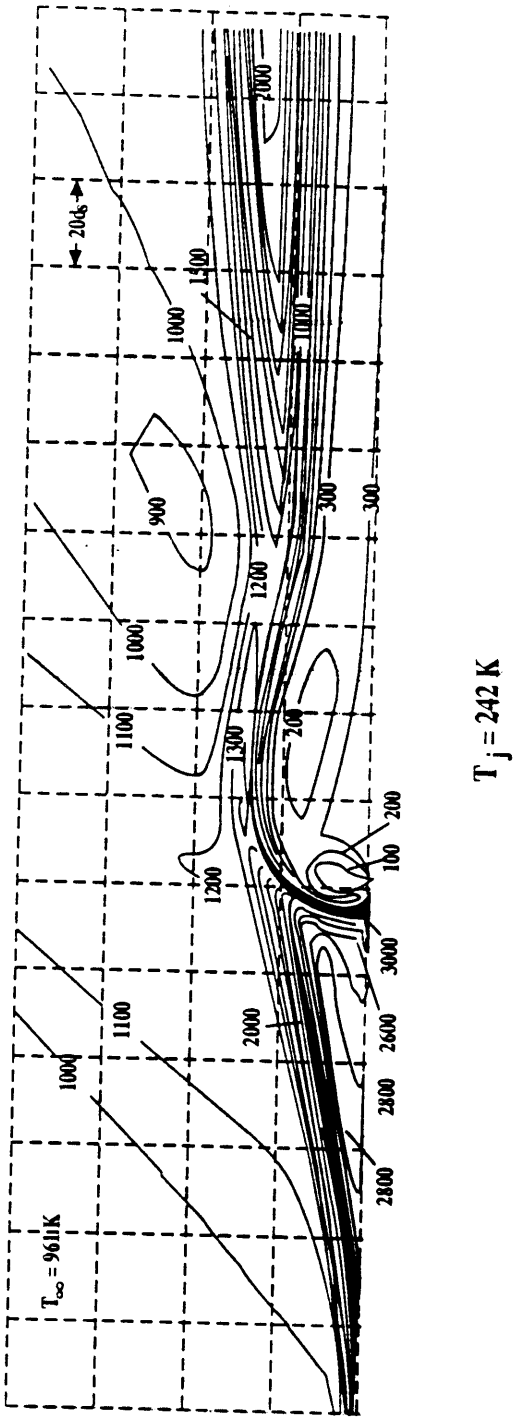

Figure 2-9: Computed Temperature Profiles Around a Slot Injector (Reference 22)

This does limit the usefulness of this plot, since the conditions downstream of the Mach disk are not the same as the initial conditions at the orifice, but it is the best way to compare this calculation with the plots that have been given previously.

In both Figures 2-8 and 2-10, the plotted contours are in qualitative agreement with the fuel penetration plots shown in section 2.1.2 (Figure 2-5 on page 18, for example). Comparing all of the plots presented in this section (cold flow theory, cold flow experiment, hot flow experiment, and hot flow numerical calculations), there can be seen significant variation in the curves near the jet injection point (small x/d values). As was mentioned in the discussion of Figure 2-5, some of the noted differences may be due to the fact that each curve results from a different set of operating conditions (and different values of q). The empirical fits could also suffer from this problem, since they use q as the only parameter, and there are other variables that effect the jet penetration (*e.g.* boundary layer thickness and free stream Mach numbers).

Despite the differences in the conditions at which the data was recorded and the different measurement techniques employed, the curves do show some similarity. For example, out at a downstream distance of x/d = 15, the height (y/d) of the different profiles all lie between about 8 and 10. As will be discussed in detail in the Results chapter (beginning on page 77), the jet boundaries plotted for the images taken during this work also fall within this range (for comparable values of q).

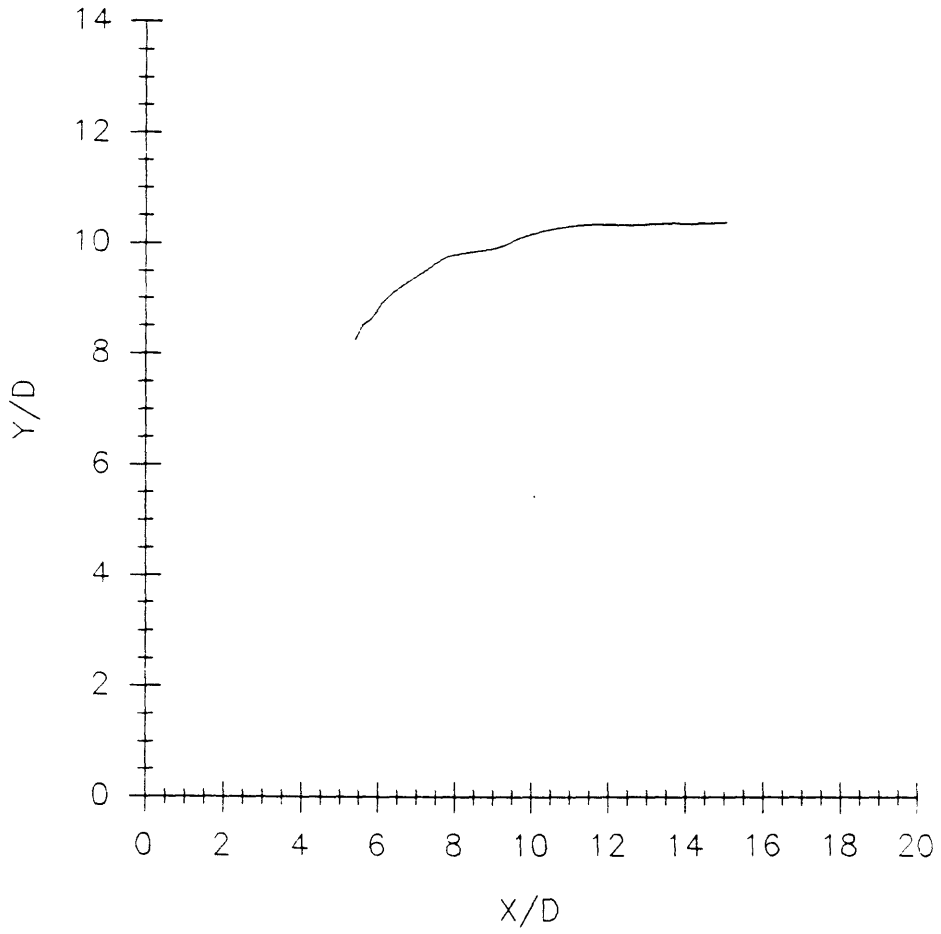

Figure 2-10: H_2 Contour, Laminar Flow (Reference 23)

2.2 Planar Laser-Induced Fluorescence

Laser or spectroscopically based techniques are non-intrusive (excluding laser-initiated chemistry) and species specific. Planar Laser-Induced Fluorescence (PLIF) also has the ability to simultaneously capture spatially resolved measurements of a large number of points in a plane, essentially providing a two-dimensional (2-D) image of the flowfield. These images can then be used to calculate species concentrations or mole fractions, temperatures, densities, velocities, and pressures.[8] Temporal resolution of the measurements is controlled both by the laser source (pulse widths of 5-10 nsec are typical), the detector gate width (as short as 5 nsec), and the fluorescence lifetime of the excited target species (hundreds of nanoseconds for OH). Spatial resolution is ultimately limited by the array detector size, with 1024×1024 (1,048,576 pixels) arrays commonly available. Detectors with up to one million pixels are now becoming available.[24] For a sheet beam and an array detector, the size of the pixels and the magnification of the collection optics controls the size of the measurement volume at each image "point."

An extension of the PLIF concept to the generation of three-dimensional pictures of a flowfield is also possible by rapidly scanning the illumination plane.[25] A few recent papers[26,24,27] have done extensive reviews of the many applications and variations of laser-based diagnostics for fluid flows and combustion; and the reader is referred to them for more details on techniques other than PLIF.

There is a huge potential for the use of imaging diagnostics in the study of reacting and nonreacting flows. The non-invasive nature of the different laser diagnostic approaches (Rayleigh, Mie, and Raman scattering, as well as laser-induced fluorescence) and their good spatial and temporal resolution make them particularly attractive for investigations into turbulent and/or reacting flows.

Laser-induced fluorescence (LIF) initially found application as a tool for spectroscopy and chemical analysis. It is a well-established method for sensing population densities of atoms and molecules in specific quantum states. With the recognition of LIF's potential to be a powerful fluid mechanics diagnostic, the single-point measurement techniques have been expanded into multiple-point planar imaging. The underlying concepts of LIF carry over directly from the single-point studies to the planar case.

The typical apparatus employed for a PLIF experiment are shown in Figure 2-11. A laser beam, generally pulsed and tunable in wavelength, is formed into a thin sheet by a train of simple optics. This sheet of laser light transverses the flowfield being studied. When the laser is tuned to excite a specific electronic absorption transition in the species of interest, a fraction of the incident photons will be

[8] Only the first two of these possible measurements are done in this study, and so the techniques for these two are discussed here.

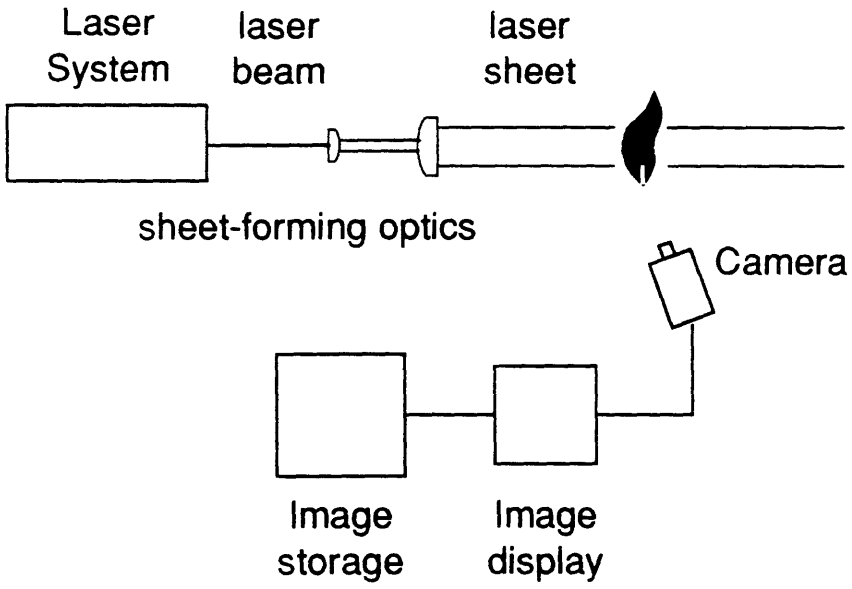

Figure 2-11: Schematic of a Typical PLIF Experiment

absorbed at each point in the illumination plane. Following the absorption process, the molecule may fall back to the lower (typically the ground) electronic state through radiative de-excitation (fluorescence).

Some fraction of the broadband emission (fluorescence from the directly excited state, and from neighboring rotational or vibrational states that are populated through inelastic collisions) is generally collected at a right angle to the direction of the laser beam's propagation. For some applications, the collected light is filtered spectrally at the detector, removing scattered laser light.

The fluorescence intensity that is collected at each pixel in the illumination plane corresponds to the product of the absorber number density in the particular quantum state and the local fluorescence yield, *i.e.*, the fraction of absorbed light that is re-emitted as fluorescence in the bandwidth being imaged. This signal intensity then gives an immediate vehicle for flow visualization, being roughly equivalent to a qualitative or relative measure of species concentration. By various strategies this signal can be related to other, more quantitative, flowfield properties. A knowledge of the quenching rates of the laser-excited species (at its local environment in the flow) allows quantitative concentrations (or mole fractions) to be calculated, and the relevant Boltzmann distribution for the excited quantum states can be used to calculate a temperature from images of the fluorescence signals subsequent to the excitation of two different transitions. These techniques are discussed in more detail in the following sections.

2.2.1 Laser-Induced Fluorescence Theory

Typically, fluorescence denotes the radiation emitted by an atom or molecule when it decays by spontaneous emission of a photon from a higher to a lower energy state. In LIF, the upper state is populated by a laser source which is tuned to a the proper wavelength. Without the laser pulse the upper electronic levels of the target species are assumed to be negligibly populated at combustion temperatures.

After excitation, the upper state can undergo a number of different processes. Figure 2-12 shows five of the most important LIF excited state energy transfer mechanisms. One method of de-excitation occurs when the molecule or atom returns to its original quantum state by laser-induced stimulated emission. This re-emission is at the same wavelength as the laser beam. Since the light entering the detector is generally filtered to remove elastic scattering of the laser light, this stimulated emission signal is not imaged.

A second method of energy transfer is that the molecule could absorb another photon while still in an excited state, and be excited into an even higher energy state, including an ionized state. This second absorption process is labeled in Figure 2-12 as Q_{ion}, the rate of the promotion of the species to an ion

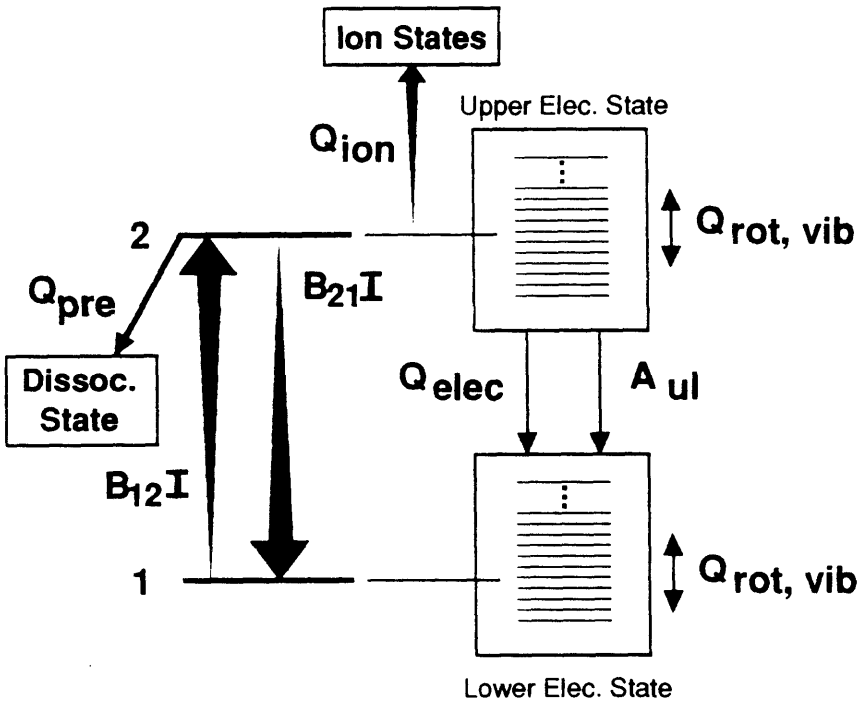

Figure 2-12: Critical Energy Transfer Processes Subsequent to Laser Excitation of a Molecular Species

state.

Inelastic collisions between molecules can cause rotational, vibrational and electronic energy transfer. Electronic state de-excitation through collisions is referred to as quenching. During such a process the excited molecule or atom is knocked back down to the ground state before it can fluoresce. The downward transfer of energy labeled Q_{elec} in Figure 2-12 graphically shows this quenching process.

Interaction between the separate atoms within the molecule can produce internal energy transfers and the dissociation of the molecule. When the dissociation is caused by the switch from a stable to a repulsive electronic arrangement, it is called predissociation. Q_{pre} denotes the rate of this process in the figure.

And finally, the original laser-populated state and nearby upper states indirectly populated though collisions could fluoresce, producing an LIF signal. The rate of the fluorescence is A_{ul}.

The LIF signal can be related to flowfield variables (such as concentration and temperature) by modeling the state-to-state transfer processes mentioned in the previous paragraphs. Because the fluorescence is a function of the upper state population, the state-dependent population dynamics must be considered. While quantum mechanical (density-matrix) descriptions are available,[28–30] most treatments of LIF[31] are based on a semi-classical rate equation analysis first developed for atomic species by Piepmeier.[32] Daily[28] has shown that the density-matrix formulation converges to the rate equations in steady state, and so he concludes that for sufficiently slow laser pulse rise times, the rate equation formulation is sufficient. He estimates the characteristic time scale for laser-excitation to be on the order of 10^{-10} sec, and so laser pulse lengths of a few nanoseconds (like those used for this work and most others) are still long enough for the rate equations to be valid.

The formal rate equation governing the time dependent population, $n_j(t)$ $[cm^{-3}]$, of a specific energy level, j, among a set of levels, i, is given by

$$\frac{dn_j(t)}{dt} = \sum_{i \neq j} n_i(t) R_{ij}^T - n_j(t) \sum_{i \neq j} R_{ji}^T, \tag{2.24}$$

where the first term represents events that populate state j, and the second term those that depopulate j. $R_{ij}^T [sec^{-1}]$ is the total rate coefficient for all events transferring molecules from level i to j. This overall rate constant includes a number of distinct constants: Q_{ij}, the collisional transfer coefficient covering both internal and intermolecular energy transfers; A_{ij}, the Einstein A coefficient for spontaneous emission (*i.e.*, fluorescence); and $B_{ij} I_\nu$, the coefficient for single-photon laser-stimulated processes, where B_{ij} is the Einstein B coefficient and I_ν is the laser spectral intensity $[Wcm^{-2}Hz^{-1}]$. Of these rate constants, it can be noted[26] that spontaneous emission occurs only if i is a higher energy level than j (*i.e.*, $A_{ij} = 0 \; for \; E_j > E_i$), the laser-stimulated rates are related by the principle of detailed balance,

$g_i B_{ij} = g_j B_{ji}$, where g_i is the degeneracy of energy level i, and $A_{ij}/B_{ij} = 8\pi h\nu^3/c^3$.

The essence of LIF is seen more clearly by simplifying Equation 2.24 to the case of a two-level system. One further simplifying assumption is that the laser source bandwidth is broad compared to the bandwidth of the molecular transition; *i.e.*, the laser spectral intensity is approximately constant across the molecular absorption line. This broadband model is appropriate for most of the tunable, pulsed lasers used in PLIF measurements.

With such assumptions, the rate equation for the upper state (the energy level directly pumped by the laser) becomes,

$$\frac{dn_2(t)}{dt} = n_1(t)\left[Q_{12} + B_{12}I_\nu\right] - n_2(t)\left[Q_{21} + B_{21}I_\nu + A_{21}\right]. \tag{2.25}$$

To remove non-linearities due to self-quenching effects (where the Q values are proportional to the number density of the ground state), this equation assumes that number density of the excited species is small compared to other quenching species. If the upper level is assumed to be only negligibly populated before the laser pulse, then an initial condition of $n_2(t = 0) = 0$ can be applied to Equation 2.25. An additional constraint is added by stating that no chemical reactions take place during the measurement, *i.e.*, that the total population is constant. This can be written as,

$$n_1(t) + n_2(t) = \ constant \ = n_1^0 \tag{2.26}$$

where n_1^0 is the initial population of the ground state, n_1. The solution to Equation 2.25 with these conditions is,

$$n_2(t) = n_1^0\left[B_{12}I_\nu + Q_{12}\right]\tau\left[1 - e^{-t/\tau}\right], \tag{2.27a}$$

where

$$\tau = \frac{1}{\left[B_{12}I_\nu + Q_{12} + B_{21}I_\nu + Q_{21} + A_{21}\right]}. \tag{2.27b}$$

As was mentioned above, $n_1 \ll n_{other\ quenching\ species}$, so that Q_{12} is approximately constant (independent of n_1).

For times long compared to the time scale τ, the fluorescence signal is assumed to have reached its steady state rate, R_P $[number\ of\ photons/cm^3/sec]$, which is written

$$R_P = A_{21}n_2^{ss} = A_{21}n_1^0\left[B_{12}I_\nu + Q_{12}\right]\tau. \tag{2.28}$$

In typical applications, the two laser-coupled energy levels are separated by a few electron-volts,

and so collisional excitations, Q_{12}, are so infrequent that they can in general be ignored. And so, Equation 2.28 is rewritten as,

$$R_P = n_1^0 B_{12} I_\nu \frac{A_{21}}{A_{21} + Q_{21}} \frac{1}{1 + I_\nu / I_\nu^{sat}}, \tag{2.29a}$$

where the saturation intensity, I_ν^{sat}, is defined as

$$I_\nu^{sat} = \frac{Q_{21} + A_{21}}{B_{12}(1 + g_1/g_2)}. \tag{2.29b}$$

Equation 2.29a is usually used in one of two limiting cases. For low laser intensities, $I_\nu \ll I_\nu^{sat}$, Equation 2.29a reduces to the linear fluorescence equation,

$$R_P = n_1^0 B_{12} I_\nu \frac{A_{21}}{A_{21} + Q_{21}}, \tag{2.30}$$

so called because the fluorescence varies linearly with laser intensity. The second limit is called the saturation limit, where the fluorescence is independent of laser power. This condition occurs when $I_\nu \gg I_\nu^{sat}$; and then R_P is given by,

$$R_P = n_1^0 \frac{A_{21}}{1 + g1/g2}. \tag{2.31}$$

The two-level model therefore leads to two very simple equations for the fluorescence rate, but it is an incomplete model; and so calculations done with these equations have a large systematic error associated with them. The primary problem with this two-level model is that it ignores rotational energy redistribution.

Lucht *et al.*[33] have developed a four-level model to provide a more accurate model for the events that populate and depopulate the laser-excited state, and the following derivation is based upon their work. The two-level model is appropriate for either of two situations. First, the two laser-coupled rotational states are "frozen" in that there is no transfer to adjacent levels; and second, the rotational levels could be completely "relaxed," meaning that rapid rotational transfer has established a Boltzmann distribution among the rotational levels in the given vibrational states. In this latter case, the two-level model can easily be corrected since the relation between the measured population of the directly excited rotational state (based on photons that were emitted only from this state, which has been depopulated due to rotational relaxation) and the initial population of the excited state is well known. In reality, however, most fluorescence processes lie somewhere between these two extremes, and so the four-level model is needed.

In the four-level model, levels 1 and 2 refer to the specific levels within the rotational manifold that are directly coupled through the laser excitation. And "levels" 3 and 4 refer to the collection of rotational

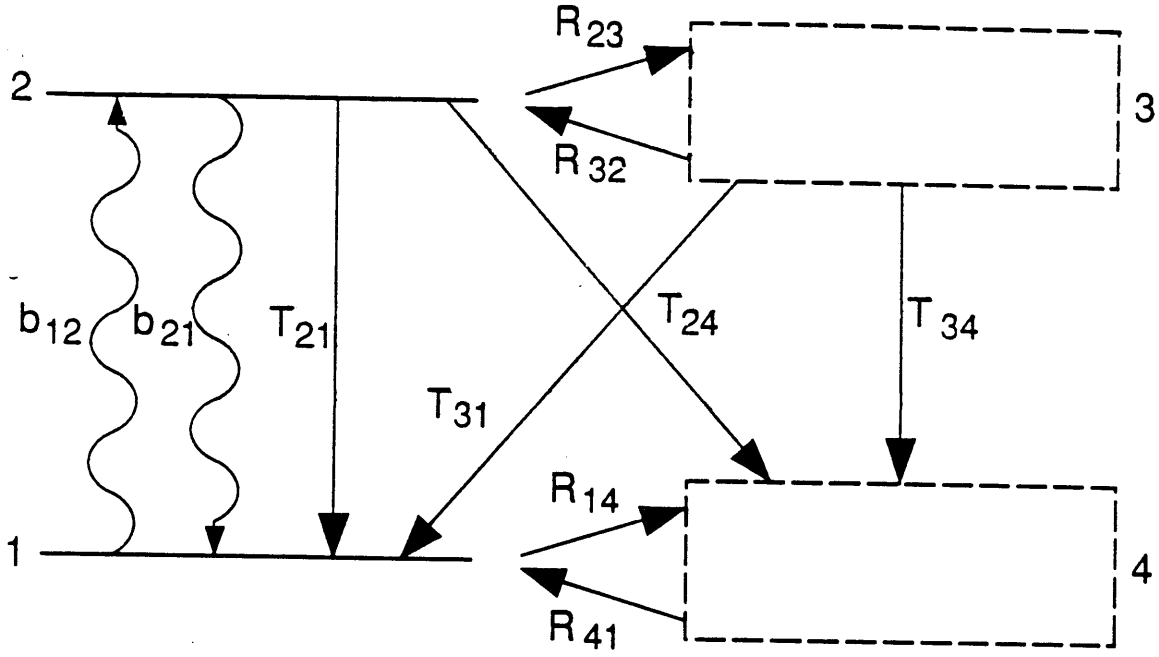

Figure 2-13: Four Energy Level Model

states in the upper and lower electro-vibrational states, respectively, that are not directly coupled with the laser. These four states are represented schematically in Figure 2-13 (page 34) with the downward transfer rates, T, representing a combination of collisional quenching, Q, and spontaneous emission, A. R represents the rotational transfer rates. The rate and conservation equations for these levels are given by:

$$\dot{N}_1 = -N_1(B_{12}I_\nu + R_{14}) + N_2(B_{21}I_\nu + T_{21}) + N_3T_{31} + N_4R_{41} \tag{2.32a}$$

$$\dot{N}_2 = N_1B_{12}I_\nu - N_2(B_{21}I_\nu + T_{21} + T_{24} + R_{23}) + N_3R_{32} \tag{2.32b}$$

$$\dot{N}_3 = N_2R_{23} - N_3(T_{31} + T_{34} + R_{32}) \tag{2.32c}$$

$$\dot{N}_4 = N_1R_{14} - N_4R_{41} + N_2T_{24} + N_3T_{34} \tag{2.32d}$$

$$N_T = N_1^0 + N_4^0 = N_1 + N_2 + N_3 + N_4, \tag{2.32e}$$

where a superscript zero denotes level populations prior to the laser pulse.

If one now adds Equations 2.32a and 2.32b, the result is

$$\dot{N}_1 + \dot{N}_2 = -N_1R_{14} - N_2(T_{24} + R_{23}) + N_3(R_{32} + T_{31}) + N_4R_{41}. \tag{2.33}$$

The first two terms here represent transfers from the directly coupled levels 1 and 2 to the rotational manifolds 3 and 4, and the last two terms represent transfers in the other direction. By assuming that the cross rates balance, *i.e.* that $N_1 + N_2 =$ *constant*, (in the limit of strong laser pumping, levels 1 and 2 reach steady-state rapidly, tens of picoseconds, and so $\dot{N}_1 = \dot{N}_2 = 0$.[31] Level 3 is also assumed to have reached a steady state value (so that $\dot{N}_3 = 0$); then N_3 can be eliminated using Equation 2.32c with the result,

$$N_2 = N_1^0 \frac{B_{12}I_\nu}{B_{12}I_\nu + B_{21}I_\nu}\left[1 + \frac{T(1 + \frac{R_{23}}{T+R_{32}})}{B_{12}I_\nu + B_{21}I_\nu}\right]^{-1}, \tag{2.34}$$

where it is assumed that $T_{31} = T_{21}, T_{34} = T_{24}$, *and* $T \equiv T_{21} + T_{24}$. This equation can be put into exactly the same form as Equation 2.29a,

$$R_P = N_1^0B_{12}I_\nu \frac{A_{24}}{A+Q}\frac{1}{1+I_\nu/I_\nu^{sat}}, \tag{2.29a}$$

but with the definition of I_ν^{sat} changed to

$$I_\nu^{sat} = \frac{(Q + A)(1 + R_{23}/R_{32})}{B_{12}(1 + g_1/g_2)}, \tag{2.35}$$

where $Q = Q_{21} + Q_{24}$, $A = A_{21} + A_{24}$, so $T = Q + A$, and since R is generally much faster than T, $R_{23}/(T + R_{32}) \approx R_{23}/R_{32}$.

The fluorescence that is viewed typically is the shifted fluorescence from level 2 to level 4, because the wavelength corresponding to the transition between levels 1 and 2 is filtered out with the scattered laser light. The ratio R_{23}/R_{32} is proportional to the number of energy levels that are populated in the rotational manifold 3 by rotational energy transfer from the directly pumped level 2. With the loss of population into other rotational levels, it is intuitively clear that rotational relaxation such as this will increase the laser intensity needed to saturate the specific pumped state. This is important because one method of determining quenching rates is to measure the saturation laser intensity. When fluorescence signal is plotted versus laser intensity, the resulting curve is typically linear for small laser powers and then begins to "roll over" as saturation is reached. Eventually the increasing laser power will no longer increase the fluorescence signal. This characteristic shape is predicted by Equation 2.29a, and is experimentally producible as well. When such a plot is generated for a particular experimental setup, then from the definition of I_ν^{sat} (either Equation 2.29b or 2.35), the quenching rate, Q, can be determined. If the two-level model is used, the quenching rate could be grossly overestimated.

Since Lucht *et al.*[33] developed their balanced cross rate four-level model, others[34] have pursued the same concepts with slightly different assumptions, but the results (specifically Equations 2.29a and 2.35) of the two theories are identical.

If the transition being targeted can be saturated (*ie.* when the fluorescence signal is independent of laser intensity), the steady-state signal becomes independent of the quenching rate as well. Equation 2.31 clearly shows how the quenching rate does not effect the fluorescence rate when $I_\nu \gg I_\nu^{sat}$. This removal of the need to know the quenching rates greatly simplifies the analysis of the images. If the laser intensities needed for saturation (see page 41) cannot be achieved, it is common to use a procedure introduced by Baronavski and McDonald[35] for treating partially saturated fluorescence data. By performing a simple expansion on Equation 2.29a, assuming $I_\nu > I_\nu^{sat}$, one obtains,

$$R_P = n_1^0 \frac{A_{21}}{1 + g_1/g_2} \left[1 - \frac{I_\nu^{sat}}{I_\nu}\right]. \tag{2.36}$$

PLIF measurements in combustion environments have been made using both linear fluorescence and saturated fluorescence techniques. They will be discussed separately in the following two sections. A third method for quantitative measurements that avoids the problems of an unknown quenching rate (as saturated fluorescence also does) is called pre-dissociative laser-induced fluorescence.[36] In this case, the upper state decay rate is no longer dominated by molecular collisions. The molecules dissociate at rates faster than the collision rate, and so quenching corrections are unnecessary. A calibration experiment

is still needed, but by eliminating quenching corrections the LIF signal becomes linearly proportional to the OH concentration (the fluorescence yield become a constant throughout the flow). Because the predissociation rate is faster than the fluorescence lifetime, the overall signal strength is reduced. The difficulties of this method are that a predissociating transition must be found for the species of interest in a frequency range accessible by an available laser. Typically, predissociating transitions occur at high vibrational levels, and so wavelengths between 100 and 200 nm are often necessary.[79]

2.2.2 Theory of Species Measurements

Linear Fluorescence Species Measurements

The derivation of fluorescence signal (for the linear fluorescence model) is completed by converting the fluorescence rate, R_P, into a total detected signal by integrating over the length of the laser pulse and by accounting for the collection efficiency of the optics. The total number of photons, N_p, that strike the photodetector from the collection volume, V_c, is expressed as,

$$N_p = \eta \frac{\Omega}{4\pi} f_1(T) \chi_m n V_c B_{12} E_\nu \frac{A_{21}}{A_{21} + Q_{21}}, \tag{2.37}$$

where η is the transmission efficiency of the collection optics, $f_1(T)$ is the fractional population of the lower state, χ_m is the mole fraction of the absorbing species, Ω is the collection solid angle, n is the total gas number density, and $E_\nu \left[Jcm^{-2}Hz^{-1}\right]$ is the spectral fluence of the laser.

Equation 2.37 shows that the fluorescence signal is proportional to the initial lower state population and to a factor $A_{21}/(Q_{21} + A_{21})$, which is called the Stern-Vollmer factor or the fluorescence yield.[26] The fluorescence signal can be viewed as a direct measurement of the lower state population, modified by this fluorescence yield. Thus an unprocessed PLIF image can provide a qualitative map of species concentration. When the Stern-Vollmer factor is constant throughout the imaged plane, the resulting fluorescence signal corresponds directly to the number density of the target species. Generally though, this factor varies with temperature (for some transitions more than others), and so ro-vibrational lines must be chosen that exhibit fluorescence yields that are fairly constant over the range of temperatures in the flow being considered. For quantitative concentration measurements, or for determining other desired flowfield variables, it is important to know the upper-state collisional decay rates, Q_{21}, particularly when $Q_{21} \gg A_{21}$ (see Equation 2.29a, page 33), which is usually the case for flames at or near atmospheric pressure.

When using linear fluorescence, there are typically three ways with which the problem of not knowing the fluorescence yield is overcome. The first is to set up a combustion environment where $Q_{21} \ll A_{21}$

(*i.e.*, at very low pressures), and so collisional quenching is no longer the dominant decay mode for molecules in the excited state. The second method used is to model the collisional processes and thus directly compute the quenching correction. And the third possible technique is to run some type of calibration experiment, one where the other quantities in Equation 2.30 are known, and the quenching rates are then found experimentally.

A graph of the number of excited molecules vs. time is shown in Figure 2-14 for varying values of Q_{21}. In this graph, the laser is turned on (assumed to come on instantaneously) at $t = 0$, and is on for all future times. For a given value of laser intensity, I_ν, varying Q_{21} alters only the steady-state value of the number of molecule in the excited state. As Q_{21} decreases, the steady-state value approaches the saturation limit, which is independent of Q_{21} (as is seen in Equation 2.31). The nearly linear region of the graph, at the very beginning of the laser pulse. is also independent of Q_{21}. This can be shown by expanding Equation 2.27a for $t/\tau \ll 1$. The result is: $n_2 = n_1^0 t$, which is clearly independent of Q_{21}.

Since the excited-state number density of interest in these two regions is independent of Q_{21}, LIF measurements made under these conditions will not require quenching corrections. At the time that the laser is turned off, the number of excited species immediately begins to decay exponentially. The rate of this decay is governed by the sum of the quenching and the spontaneous emission rates (and the rates of any other processes that depopulate the upper-state - like predissociation).

Figure 2-14 also helps to explain why a short laser pulse can eliminate the need for quenching corrections. In low pressure flames ($\approx$ 20 torr) for example, the quenching is low enough (Q_{21} for OH $= 5 \times 10^7\ sec^{-1}$[37]) that the linear build-up region is extended such that a nanosecond laser pulse ends while the upper-state population is still in the linear build-up phase. In atmospheric flames, however, picosecond laser pulses would be required. Nanosecond laser pulse lengths are typical of most standard pump lasers used for the current PLIF studies.

When another process depopulates the upper state much faster than quenching does (such as predissociation), then even the steady-state upper-state population level is independent of quenching. When predissociation is occurring, the predissociation rate, P, must be added to the denominator of the fluorescence yield. And if $P \gg Q_{21}$, the steady-state upper level population (and the fluorescence yield) becomes virtually independent of the quenching rate. Even though the fluorescence signal does still depend on the predissociation rate, it is constant throughout the flowfield (whereas the quenching rate varies), greatly simplifying calibration procedures.

Another way to account for collisional quenching is to directly compute the quenching rate from

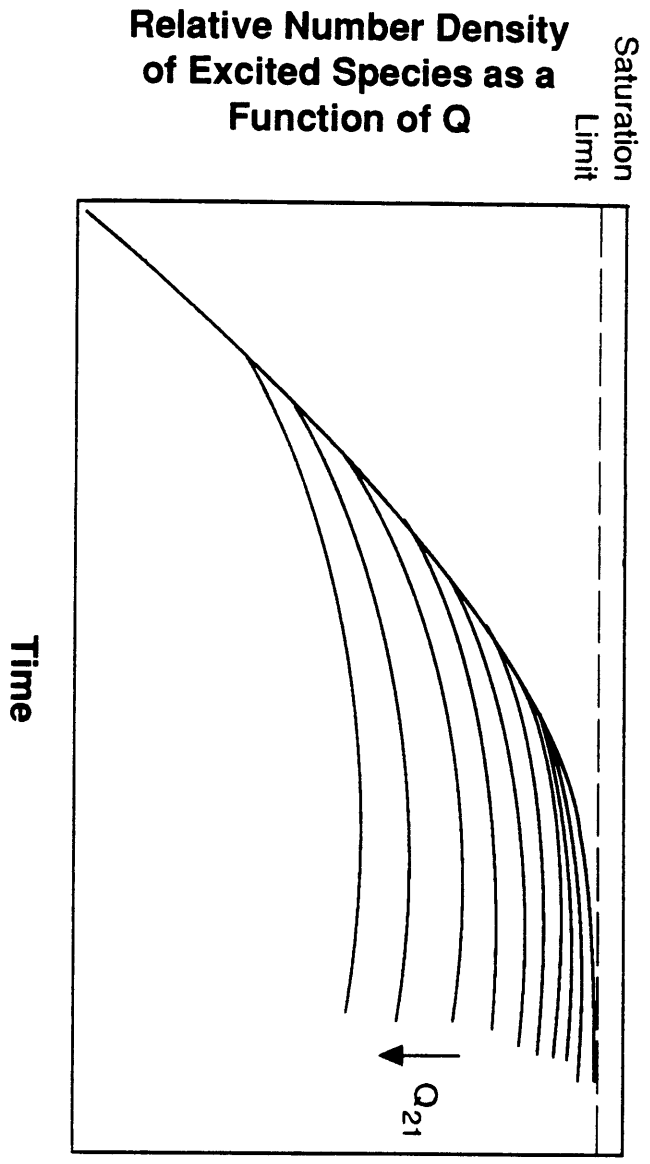

Figure 2-14: Relative Number Density of Excited Species vs. Time

theoretical models. This is typically done[31] by using the relation

$$Q_{21} = \sum_i n_i \sigma_i v_i, \tag{2.38}$$

where n_i is the number density of the deactivating species, σ_i is the cross section for quenching (or deactivation), and v_i is the relative velocity between the molecule being quenched and the atom or molecule that is doing the quenching.

This method has some difficulties however. Often for the species of interest (particularly in flames), the collisional cross sections are not well known or not known at all. Furthermore, the values that are available are generally for room temperature conditions, and Bergano *et al.*[38] have shown that such cross sections can vary significantly with temperature. In addition, the temperature of the flame, especially the local temperature in a turbulent flame, is not well known. Thus accurate values of Q_{21} cannot be determined because both v and σ are dependent on temperature.

Yet another difficulty in assessing Q_{21} is that the quenching cross sections also vary with the collision partners. At every measurement location, the dominant collision partners and the temperature are needed to successfully compute a quenching cross section. This is challenging enough for simple, laminar flames, but it certainly limits the application of this computational technique for turbulent combustion.

Another recent theoretical study by Garland and Crosley[39] has surveyed many independently determined quenching cross sections for OH, and has calculated total quenching rates (taking into consideration collision partners, rotational levels, and temperature) in hydrocarbon and ammonia flames. Even in these well-characterized (non-turbulent) flames, they only claim to be within 30-50% of the actual quenching rates.

As was previously mentioned, a third method for computing absolute (as opposed to relative) species concentrations is to run a calibration experiment.[40] The basis for one variation of this technique is as follows. By using ideal gas assumptions, the effects of pressure and temperature on gas density and relative collisional velocities (but not collisional quenching cross sections), which are important in Equation 2.38, can be used to correlate a quenching rate at a known set of conditions to a quenching rate at a different pressure and temperature. In equation form such a correlation is expressed as,

$$Q_{21}(T, P, \chi_i) = \left(\frac{P}{P_{ref}}\right)\left(\frac{T_{ref}}{T}\right)^{1/2} Q_{21}(T_{ref}, P_{ref}, \chi_i). \tag{2.39}$$

This equation is only expected to be valid over a small range of temperatures, and so T_{ref} and P_{ref} need to be close to the expected values of T and P.

Referring back to Equation 2.37 (page 37), when $Q_{21} \gg A_{21}$, the number density of the absorbing

species, $\chi_m n = n_m$, can be written as,

$$n_m = C_1 Q_{21}^{-1}(T, P, \chi_i)\frac{N_p}{E_\nu}, \tag{2.40}$$

where the constant C_1 has absorbed the various spectroscopic constants and constants of the detector and collection optics. By substituting Equation 2.39 into this equation, and absorbing $Q_{21}(T_{ref}, P_{ref}, \chi_i)$ into the constant, the following is obtained:

$$n_m = C_2 \left(\frac{P}{P_{ref}}\right)\left(\frac{T_{ref}}{T}\right)^{1/2}\frac{N_p}{E_\nu}. \tag{2.41}$$

To determine C_2, a calibration experiment with a known concentration of the target species needs to be done. Another point that needs to be considered for this calibration is that C_2 will vary from pixel to pixel in an array detector. Such consideration is necessary because C_2 measures both quantum efficiencies (which vary from pixel to pixel), and fluorescence volume, which can have small variations due to imperfect optics. This variation in sensitivity must be measured independently, and C_2 corrected for each detector element.

This calibration technique obviously only works when a reference condition can be suitably defined and measured (using exactly the same experimental setup as for the actual experiment) for the combustion process being studied, and when local values of P and T are known. These two conditions are not always possible.

Saturated Fluorescence Species Measurements

As seen in Equation 2.31 (page 33), when the laser intensity is made sufficiently large, the absorption and stimulated emission rates become much larger than the quenching rate, and so a quantitative knowledge of the quenching rates is not needed. This condition is called saturated fluorescence. Another advantage of using saturated fluorescence is that the signal is maximized (adding more laser power won't increase the signal at all), providing the greatest species detection sensitivity. One serious disadvantage of saturated LIF studies is that the laser intensities needed to saturate some species of interest are so high that laser sheets cannot be used. And so the saturated fluorescence technique is generally restricted to point measurements. For example, Piepmeier[32] has calculated that laser power densities needed for saturation are on the order of 100-200 kW/cm^2 for some common metals. For turbulent flowfields, where multiple point measurements in the flow need to be taken simultaneously, the use of saturated LIF may not be feasible.

Saturated fluorescence represents an attractive method in that the fluorescence signal is completely independent of both laser power and electronic quenching rates (as is shown in Equation 2.31). This

eliminates the need for the complex calibration schemes or the inaccurate computations that are needed for quantitative species measurements using linear LIF. Calibration cannot be entirely foregone, however. The optical collection efficiency must still be characterized. But procedures to do this are typically simpler than calibrating both the optics and the quenching, as is needed for quantitative linear fluorescence measurements.

2.2.3 Theory of Temperature Measurements

To make temperature measurements using laser techniques such as LIF, one assumes that a Boltzmann population distribution exists among various rotational and vibrational states. The Boltzmann relation gives the relative populations of two separate states as a function of temperature, and then LIF can be used to determine the actual ratio of populations in the two states so that a temperature can be calculated. The Boltzmann distribution for the relative density n_i in a quantum state i of a molecule can be written,

$$n_i \propto (2j+1)exp(-E_i/kT), \tag{2.42}$$

where k is the Boltzmann constant, j is the total angular momentum, and E_i is the energy of the quantum state i above the ground state.

The number density n_i is equal to $f_1(T)\chi_m n$, and so Equation 2.37 can be rewritten as,

$$N_p = Cn_i q_i \frac{A_{ji}}{A_{ji}+Q_{ji}}, \tag{2.43}$$

where the laser and optics parameters are absorbed into C and q_i is the relative line strength of the transition labeled i. When fluorescence signals are taken from the exact same experimental setup, C is constant. Suppose that two signals are measured, with S_1 representing the LIF signal collected subsequent to exciting state i_1, and S_2 representing the signal obtained by exciting a different state, i_2. With the Stern-Vollmer factor $A/(A+Q)$ assumed to be independent of quantum state,[47] the ratio $R = (N_p)_1/(N_p)_2$ reduces to

$$R = \frac{(N_p)_1}{(N_p)_2} = \frac{(nq_i)_1}{(nq_i)_2} = \frac{q_1(2j_1+1)}{q_2(2j_2+1)} exp\left(\frac{E_2-E_1}{kT}\right), \tag{2.44a}$$

Solving for T yields,

$$T = \frac{E_2-E_1}{k\ ln\left[\frac{q_2(2j_2+1)}{q_1(2j_1+1)}R\right]}. \tag{2.44b}$$

In this equation, the ratio, R, is directly measured, and all of the other quantities are known. As can be seen, only the relative fluorescence signals from the two lines are required, and so complicated calibration procedures are not needed and laser power fluctuations no longer affect the results.

In principle, a temperature could be determined using any two quantum states; but the precision of the measurement relies on the variation of R with temperature. For a good signal-to-noise ratio, the energy separation between the excited states should be greater than kT.[36, 48, 49]

The assumption that the quenching rates are independent of state is not always a very good one. It has been shown[50] that the quenching rate is quite sensitive to both collision partner and rotational level. Thus, this approach is valid only when quenching rates for each state are equal and hence cancel, or when quenching occurs too slowly to be an issue.[9] An example of the latter is in low pressure flames, where collisional quenching need not be considered (see page 37). But even if the quenching rate is not constant throughout the flow, it would appear in the logarithm of Equation 2.44b; and hence its influence would be small.

The fluorescence yields will also cancel if the excited transitions originate from the same upper state. If an upper state can be found that decays back to the ground state and also to another intermediate state, then the quenching rates of the two lines will be identical. This method has some drawbacks, however.[36] The only way to measure the fluorescence signals when the same upper state is accessed is by time resolution (because the resultant fluorescence signals are too close spectrally for filtering to be used), and the same upper state can only be reached from neighboring lower states (so $\Delta j = 2$), meaning a small energetic difference between the probed states, creating inherently low precision. When time resolution of the signals is used, the two signals must be separated in time, reducing the "instantaneousness" of the observation.

To evaluate a temperature, the two signals S_1 and S_2 need to be measured separately. The two signals need to be separated somehow, either in frequency (so spectral filtering can separate them), or in time (so that an acquisition system can isolate them). Each of these two approaches has disadvantages. Because two different transitions need to be excited, spectral filtering uses two detectors and two laser systems (a very expensive option); and time resolution eliminates the ability to capture instantaneous maps. If averaged temperatures are acceptable, the second choice is certainly satisfactory. The choice between these two approaches would depend upon the equipment available and the wavelength separation between the two excited states (if they are too close together, spectral filtering would be impossible). Temporal separation was used for the work described in this thesis, with many-image averages being used for each state.

[9] This same problem was discussed in the section on linear fluorescence.

In turbulent systems, averaged as well as instantaneous pictures of the temperature field are desirable. For all of the two-line excitation techniques discussed here, instantaneous measurements (two pulsed, tunable laser systems and two solid-state cameras) are hampered by high equipment costs. Two different single excitation techniques have been suggested.[51] The first of these relies on rapid collisions to redistribute the population from the directly excited state into adjacent states. Then, one laser excites one state, and two cameras, each collecting fluorescence from only one transition (using appropriate filters), simultaneously record the two signals S_1 and S_2 needed. The difficulties with this is that the signals may depend on unknown collisional relaxation rates, requiring careful calibration; and, secondly, collisional relaxation may not separate the two states by enough energy to make the calculation accurate.

The second technique only applies to cases where the mole fraction of the absorbing species is fixed. In this case, the signal becomes a known function of temperature only (see Equation 2.37 on page 37). Q_{21} depends on temperature because of the collisional velocity (see Equation 2.38), and f_1 is the Boltzmann fraction. Both of these quantities (Q_{21} and f) can be calculated as functions of temperature, and then a plot of relative fluorescence signal vs. temperature can be made. The measured signal strength can then be interpreted in terms of a temperature. While both of these approaches could work in limited applications, for the majority of cases (including the work being reported here) they are not suitable.

2.2.4 Qualitative Species Imaging Experiments Using LIF

The extension of single-point laser-based diagnostics (reviewed in detail by Eckbreth[52]) to planar array detection schemes was first done by Long *et al.*[53] and Escoda and Long[54] (at Yale University) using Mie and Rayleigh scattering. In these experiments a 100×100 pixel array (a gated low-light-level TV camera) was used to record instantaneous concentration (qualitative only) profiles of turbulent, nonreacting jets.

In 1982, three groups used laser-induced fluorescence to capture planar images. Alden and coworkers[55] used a gated, intensified diode array to capture images of OH in CH_4/air and propane flames at atmospheric pressures. Dyer and Crosley[56] they used a vidicon camera (500×500 pixels) to image OH. Hydroxyl radical concentrations as low as 700 parts in 10^6 in a stable, laminar diffusion flame were measured. And lastly a group from Stanford, Kychakoff *et al.*,[57] measured OH concentrations in both a premixed laminar flat flame and a premixed turbulent flame with a photodiode array (100×100 pixel). They claim that mole fractions of 10 ppm should be detectable.

A different application of PLIF is the study of vapor/liquid distributions in spray flames.[58] To make the two phases distinct from one another, some property that differs between the two must be exploited.

The work reported in Reference 58 uses exciplexes (*excited state complexes*) to red-shift the fluorescence of a target molecule in the vapor phase relative to the liquid phase. This is done by forming a second emitting species when the excited target species reacts with a secondary molecule. The complex that is formed between the two then fluoresces at a different wavelength than the un-reacted molecules. The two different wavelengths are then used to distinctly visualize the liquid and the vapor phases simultaneously. Because a large number of combustors use liquid fuels, the study of liquid spray flames is an important one.

Allen *et al.*[59] studied liquid-fueled spray flames using PLIF of OH and seeded NO and photodissociation measurements of C_2H_2 to measure species and temperature distributions in a heptane/air flame. They found that the PLIF temperature measurements were within experimental error when compared to radiation-corrected thermocouple measurements. They did not attempt to quantify their species concentration images.

Another qualitative OH study in various flames was done at Stanford by Kychakoff and coworkers[60] in 1984. The focus of this study is, as in the previous experiments that were mentioned, more on the demonstration of the technique rather than on the results. They concentrate mainly on the sensitivity and resolution of the diagnostics; developing and expanding the technique of PLIF.

In 1986 the group from SRI, Dyer and Crosley, used LIF (at a point, not a plane) to study simultaneous excitation of several radical species in atmospheric flames.[61] They use overlapping resonant transitions of OH, NH, CH, and CN at 312.22 nm to measure the radicals simultaneously in both space and time. Their work primarily represents an investigation of the feasibility of multiple species excitation, and of the spectroscopic aspects and collisional processes that are important for the application of LIF to simultaneous, multiple species detection.

Although the emphasis of many of the works described here is on the OH radical, the techniques of PLIF are applicable to any species that has a transition at a wavelength that is accessible by current lasers and that is strong enough to provide a detectable fluorescence signal. Lee *et al.*[62] (from Stanford University) have demonstrated the acquisition of PLIF images of O_2 in flames using an ArF excimer laser at 193 nm. One extension of the technique that they were able to make with this laser source is the observation of the real-time evolution of flame structures. The ArF excimer laser is capable of repetition rates up to 250 Hz, and so high-speed sequences can be filmed. This research group has also done work (discussed in later paragraphs of this section) on the PLIF imaging of NO.

A comparison of three different visualization techniques was reported in 1990 by Diskin *et al.*[63] In this study three techniques were employed: (1) simultaneous ArF laser imaging of H_2, O_2, and Rayleigh cross-section weighted densities in a H_2/air flame, (2) ultraviolet flashlamp imaging of O_2,

OH, and Rayleigh cross-section weighted densities in a H_2/air flame, and (3) Raman Excitation plus Laser Induced Electronic Fluorescence (RELIEF) velocimetry in heated air flows. They conclude that a combination of techniques will offer unique diagnostic capabilities. For example, they suggest that a simultaneous stimulated Raman pumping of both H_2 and O_2, together with a broadband ArF laser may provide simultaneous H_2 and O_2 velocimetry and species imaging.

Paul, alone[64] and with coworkers,[65] has worked on developing and characterizing detectors for use in PLIF experiments. He has identified that the limiting factor for signal performance in CCD cameras is due to intensifier saturation, which limits the dynamic range available. The limiting factor in spatial performance results from the use of fast, cascade imaging systems. These systems tend to blur sharp edges, as one excited pixel may bleed over into neighboring pixels in the cascade process. In 1990 Paul *et al.*[65] studied an improved camera system to remove some of the limitations found previously. By greatly increasing the number of pixels in the camera (to 221,184 from 16,384, with plans to use 480,000), which increases the spatial resolution available, and using a cryogenically cooled CCD array which produced improved contrast, a larger dynamic range, and a better signal to noise ratio. With these improvements, they predict flowfield imaging technology entering a mature phase, with future work bringing increased emphasis on image interpretation and application.

One such application of LIF (in a line, not in a plane) was the study of the perturbation of a flame by a probe. Because of its precise spatial resolution, Stepowski *et al.*[66] found that LIF can be used to solve a specific experimental problem. They found that the presence of the sampling probe reduced the OH concentration in the preheating zone of the flame (perhaps due to the perturbation of the diffusion field by the probe). And so, OH levels measured with a sampling probe in this area were lower than they actually are (in an undisturbed flow). The discovery of this systematic error in sampling probes is of obvious importance.

2.2.5 Injections Studies Using PLIF

The transverse injection of a gas into a supersonic free stream was studied using PLIF by Lee *et al.*[21] They used seeded NO to study the nonreacting case, and they used OH to probe a reacting flowfield. In the reacting case, they found that the majority of the combustion occurs in two places; (1) in the shear layer between the jet and the free stream, and (2) in the boundary layer next to the wall behind the jet. Because this work is similar to the present study, it is discussed in more detail and in direct comparison to current result in the Results Chapter (Chapter 4). Lee *et al.* also found the presence of large scale turbulence structures in the flowfield, suggesting the need to study the instantaneous (rather than time-averaged) mixing and combustion processes. Single-shot laser diagnostics are of course well

suited for such studies.

Normal injection was also studied by McDaniel and Graves[15] and Abbitt and coworkers[67] (both from the University of Virginia). In the first study, a database was created for validating calculations of 3-D mixing in a supersonic combustor without reactions. The "fuel" stream was seeded with iodine and PLIF was used to study three different injection configurations: (1) injection from a single orifice into a constant area duct, (2) injection from a single orifice behind a rearward facing step, and (3) injection from staged orifices behind a rearward facing step. Results of their work on the single injector without the step is relevant to the present study (see section 2.1.2 on page 14).

A later study by the group from Virginia[67] examined the mixing subsequent to injection from two ports located behind a rearward facing step in a supersonic flow. PLIF images of seeded iodine was utilized to compute injectant mole fractions, and to create a 3-D database of the injection process by combining many 2-D slices at various locations.

A third study of normal injection was done using both laser-based techniques and conventional schlieren photography.[68] Large-scale turbulent structures in the flow were evident with the laser-generated images but did not show up on the schlieren photographs. The flowfield studied was nonreacting, and the imaged the fluorescence was obtained by exciting seeded biacetyl vapor. No jet profiles were determined however.

2.2.6 Quantitative Species Concentration Experiments Using Linear LIF

Cattolica and Vosen[40] have used the calibration technique described on page 40 to measure OH concentrations. They used Rayleigh scattering from SF_6 to determine the sensitivity of each pixel element, and then used a capillary-tube burner (in place of their full experiment's constant volume combustion chamber) with a known temperature, pressure, and OH concentration to calculate the constant C_2 in Equation 2.41 (page 41). The results they obtained for OH concentrations agree to within experimental accuracy with the predictions of a laminar flow model for their system.

The calibration technique has been utilized in several different forms. Each research group uses a different mix of calibration and calculation to make quantitative species measurements depending upon the experimental configuration.[10] For an overview of many of these ideas, the reader can see Reference 27.

Another approach to linear LIF measurements is to ignore quenching corrections altogether! This is what is done for very low pressure flames, but as Barlow and Collignon[69] have shown, it can also

[10] Is the flame laminar or turbulent? Are the major collisional partners known? Is the laser beam well characterized?

be applicable to atmospheric flames under some conditions. They have shown, both experimentally and theoretically that quenching effects are virtually cancelled out by changes in the Boltzmann fraction. Looking back at Equation 2.39 (page 40), the quenching rate is only corrected for changes in the collision velocity at different points in the flame. But there are two other variations between the calibration or reference point and other points in the flow. The collisional cross section changes with temperature, as does the population fraction in the ground state (since the Boltzmann fraction varies with temperature). Thus the total difference in quenching rates between a reference point in the flame and all other points is approximately zero when the decrease in quenching cross section is canceled by the increase in ground-state population fraction.

This simplifying cancelation only occurs at some flame conditions (non-sooting methane flames at atmospheric pressure), but Barlow and Colligon found that their uncorrected OH concentration measurements agreed to within 10% of code-calculated and previously observed results. Only a simple calibration of the fixed optical, spectroscopic, and electronic properties of the flow and imaging systems is then needed, much easier than correcting for quenching at every point in the imaged field.

2.2.7 Quantitative Species Concentration Experiments Using Saturated LIF

Most of the early uses of saturated fluorescence to measure quantitative concentrations[35, 70–72] was done using the two level model discussed in section 2.2.1. To neglect the rotational relaxation effects, implicit in the two level model, is valid only for studies at very low pressures.[71] These studies also temporally integrated over the fluorescence signal and collected fluorescence over the entire beam diameter (one dimensional studies, not planar), and so non-saturated fluorescence contributed both spatially and temporally to the signals. Concentration values measured by such an approach varied by factors between 2 and 5 from the concentrations measured independently by absorption measurements.

When Lucht *et al.*[33] developed the balanced cross-rate four-level model, they applied it to saturated LIF signals.[44, 73] They found that measurements of OH could be performed to within 20% of number densities derived independently. They also demonstrated the insensitivity of saturated fluorescence to flame pressure by varying the pressure over an order of magnitude. Their estimated OH detection limit was $10^{12} - 10^{13}$ molecules/cm^3.

Kohse-Hoinghaus *et al.*[72] compared saturated fluorescence with linear fluorescence measurements in low (10 torr) pressure flames, and found good agreement between the two methods. In the low pressure flame, they assumed that the laser pulse was short enough so that quenching was not a factor in the linear regime, and for the saturated measurements they used Milander's approach[71] which corrects the

actual probe volume to account for the portions that were not at saturation.

Kohse-Hoinghaus *et al.*[42] later went on to improve the accuracy of saturated fluorescence measurements by strictly monitoring and correcting for: (1) nonuniform saturation depending on the spatial intensity distribution across the laser beam, and (2) pulse-to-pulse variations of the spatial, temporal, and spectral laser intensity distributions. In addition, they used a low-pressure flame to remove the effects of collisional processes, and measured local temperatures using rotational spectra of excited molecules. They found their number densities to be in good agreement to other experiments and exhibit a $\pm 15\%$ uncertainty.

Kohse-Hoinghaus *et al.*[41] also compared saturated LIF measurements of OH to both previous experimental results and to a one-dimensional chemical-kinetic model of the low-pressure flame. They found them to be in good agreement. They also note that the local temperature is a key parameter in the modeling, illustrating why simple (such as the 1-D model they used) models are insufficient for turbulent, non-equilibrium flames.

Drake *et al.*[45] have used saturated fluorescence to map OH concentrations in non-premixed flames. Their probability density functions for OH concentrations in turbulent flames (the first ever measured directly) confirm computations that predict superequilibrium conditions (up to 4 or 5 times the equilibrium values) near the fuel's entrance into the air.

One final application of saturated fluorescence was another study done by Lucht *et al.*[46] where they examined the role OH plays in sooting. The hydroxyl radical is thought to play an important role in the oxidation of soot and soot precursors, but there had been very little work done on OH concentrations in fuel-rich flames to characterize potential contributions of OH in the soot-forming process. The calibration for their measurements was done on a lean (non-sooting) flame, and was considered applicable to the rich flame because of the demonstrated insensitivity of saturated fluorescence to collisional transfer rates. They estimate an accuracy of $\pm 20\%$ in the rich flame, with a detection limit of 5 ppm. They demonstrated that saturated fluorescence can be useful even in environments with large particulate densities. It was observed that visible soot begins to form only after the OH concentration has dropped significantly from its peak value in the flame.

2.2.8 Temperature Mapping Experiments Using PLIF

Paul and Hanson[49] demonstrated the first single-shot, two-camera/two-laser OH PLIF imaging of temperature in a compressible high-speed flow of combustion products. One excimer laser was used to pump two dye lasers, with the output of one time-of-flight delayed by 34 nsec. The accuracy of

their measurements was tested by careful comparison to thermocouple measurements. They calculated temperatures using the frozen model (which assumes that rotational relaxation does not occur), and found a systematic error of +134 K at 1845 K because of this. By shifting the temperature scale downward by this amount, there was still some variation between the thermocouple readings and the PLIF calculations. There was a drift towards higher temperatures with decreasing gas temperature. This drift was small however, well within the 10% random variation in shot-to-shot images.

Allen and coworkers[74] used two lasers and two cameras to capture "instantaneous" temperature and relative species concentrations. They tune the lasers to two different wavelengths, and pass them through the flame overlapping in space, but separated in time by about 1 μsec. The ratio between the two images is used to compute a temperature, while one image is used to extract a map of the OH number density. The found their temperatures established via the laser technique agreed to within 100 K of the thermocouple readings recorded in their flame.

Fast predissociation of an excited molecule was used to measure temperatures in atmospheric pressure flames, eliminating the need for quenching corrections, by Anderson *et al.*[36] The species O_2, OH, and H_2O were excited with a tunable, broadband excimer laser, and both emission and excitation spectra were recorded. They found that spectral filtering was sufficient to separate fluorescence from simultaneously excited transitions, and so concluded that measurement of the rotational temperatures with a single laser shot would be feasible. This work was only done with cylidrical laser beams, but they are working on sheet illumination and detection, and they claim it should be feasible.

A different PLIF technique for single-shot temperature measurements was developed at Stanford.[75] In atmospheric flames, the quenching rate is greater than the Einstein A coefficient by three orders of magnitude, and so the resulting fluorescence signal can be expressed as:

$$I_{LIF}(T) \sim \chi_s \frac{f(T)}{\sqrt{T}}, \tag{2.45}$$

where χ_s is the mole fraction of the absorbing species and $f(T)$ is the Boltzmann distribution. The $1/\sqrt{T}$ dependence comes from the collisional velocity component of the quenching equation (Equation 2.38). Because the Boltzmann fraction is a known function of temperature, once χ is known, the fluorescence signal can be expressed as a function of temperature alone. To avoid a simultaneous concentration measurement, this group simply seeded NO into the fuel stream at a known mole fraction. The maximum signal intensity was calibrated to the peak temperature of the function $f(T)/\sqrt{T}$.

Their generated contour plots of temperature in the flame are within $\pm$100-200 K of temperatures established using other LIF techniques in a similar flame. The main source of error in the experiment was the unaccounted-for dependence of the quenching cross section on both collisional partner and

temperature (the quenching cross section was considered constant for their study). These two effects tend to cancel each other, with the collisional cross sections decreasing with temperature, but being higher for minor species (CO_2, H_2O, O_2) than for N_2, the predominant (and hence accounted-for) molecule. Extending this technique to more complex reacting flows would require more data on the quenching cross sections of NO and on the chemical reactivity of NO at combustion temperatures.

The same technique just described was extended to low-temperature flows using iodine fluorescence subsequent to broadband argon-ion laser excitation[76] (the seeded NO method used by Seitzman *et al.* is limited to temperatures above 300 K). The iodine fluorescence was used to study the well known flowfield of a Laval nozzle, and the results were compared to a Navier-Stokes code calculation. Their temperature measurements agree to within 2% of the code predictions, and they claim that their technique is useful for pressures between 150 and 1000 torr and for temperatures between 100 and 300 K, a range common in super- and hypersonic aerodynamics (but not in combustion environments).

Cold compressible flows were also studied using iodine fluorescence by Ni-Imi *et al.*[47] They used a two-line excitation scheme similar to what is described in the theory section (page 42). Their temperature measurements, obtained in a supersonic free jet, agree to within a few degrees of theoretical predictions.

A test facility for supersonic combustion research using PLIF methods was built and tested by Allen *et al.*[74] They used two lasers to excite two lines of OH ($P_1(4)$ and $Q_1(12)$in the (1,0) band of the $A^2\Sigma^+$ electronic state), and then they compared these results to both thermocouple measurements and to temperatures determined from rotational spectra. They found their best agreement between the PLIF data and the thermocouple to be 100 K.

In a study similar to the one mentioned above (from Reference 77), McMillin *et al.* used PLIF images of NO in a shock tube to construct temperature maps of flows with strong shocks.[48] They used only a single laser and camera, relying on the reproducibility of the flow to make shot-to-shot flow structure changes irrelevant. A total shot-to-shot random error (including laser frequency tuning, laser spectral width, and flow reproducibility) of 16% was noticed.

Palmer *et al.*[78] have used PLIF for flow visualization and temperature measurements needed to characterize a new shock tube facility (reflection type with a free jet expansion). They used a combination of shadow imaging, PLIF, and method of characteristics calculations, each complimenting one another, in their investigating.

One final PLIF temperature technique that was used[79] involves exciting O_2 at 193 nm in a heated air flow (no combustion). A number of predissociative states were excited with one laser pulse, thus eliminating the need for quenching corrections. They measured fluorescence levels in gases at a known temperature to validate theoretical predictions, and then used their model to create a 2-D plot of the

temperature in an experimental flow with a stated accuracy of ± 50 K.

Chapter 3

Experimental Equipment and Procedure

The apparatus used for the experiments described here has two main components, the flow system and the diagnostics/imaging system. Because they are entirely independent of each other, they will be addressed separately in the following two sections.

3.1 Flow System

The ability of current test facilities to investigate the interdependence of gas dynamics and combustion chemistry is limited primarily by flow contamination. Vitiated-air flows suffer from water contamination, and arc-heated flows have electrode contaminants. Shock tube flows are relatively contaminant free, but run times are limited to a few milliseconds. Resistive heater-driven flows are limited in the maximum temperatures they can achieved, and so are limited in their ultimate attainable flow speed. The radio frequency (RF) discharge system used here, by the nature of its operation, eliminates contaminants, maintains a very high temperature (up to 10,000 K), and runs in a continuous flow mode.

The use of radio-frequency heating for the production of a clean, high-enthalpy source for ground aerodynamic test facilities was suggested by Rhodes and Keefer.[80] A disadvantage of the RF driven system with respect to the current study is that the stagnation pressures attainable are small ($\approx$250 torr) with a 20% oxygen in argon stream.[1] At its current size, the flow system is only a laboratory

[1] Characterization of the tube is not complete - higher pressures may be possible. In an stream of pure argon, pressures

device, with a test section $\approx 1.5x2x2$ cm. Extrapolation to a large-scale test facility is certainly feasible, but is not in place currently.

A schematic of the gas flow system is shown in Figure 3-1. An Ar/O_2 mixture (20% O_2) from a K bottle is regulated to sub-atmospheric pressures and is fed into the plasma tube. A 50 kW RF generator supplies the power to the plasma tube, where the gas is heated to high temperatures (5,000 - 10,000 K) and then fed to the entrance of a water-cooled half-nozzle by a short connecting section. At the inlet to the nozzle (the stagnation conditions) the temperature has dropped to roughly 2500 K because of radiative losses and heat conducted to the cooled walls. Oxygen begins to dissociate at about 2000 K, and in the plasma it is virtually fully dissociated. At the nozzle entrance the oxygen is still mostly dissociated because the very low density prevents equilibrium conditions being reached (this is demonstrated through calculations described in the section on the stagnation conditions, page 60). The nozzle stagnation pressures (P_0) are set by simply regulating the Ar/O_2 line pressure. Typically P_0 ranges between 50 and 200 torr. The gas exits the approximately 3 cm half-nozzle traveling at Mach 1.5.[2]

The injection block shown in Figure 3-1 contains a 0.48 mm hole though which the hydrogen is injected. This hole is aligned with the centerline of the nozzle, and is located 0.70 cm downstream from the exit plane. According to calculations, the flow over the injector block is laminar; and the region of interest for the experiments lies between the injector orifice and the end of the block, 1.15 cm (23.5 orifice diameters) downstream.

The chamber pressure, which the flow exiting the nozzle encounters, is adjusted using a gate valve located between the expansion chamber and the vacuum pumps. The pressure in the expansion chamber is set so that the nozzle exit pressure equals the expansion chamber pressure (*ie.*, matched conditions). The back pressure needed to achieve matched conditions was determined by a calibration procedure. The flow stream static pressure was measured by a pressure transducer connected to the injection orifice. The static pressure was recorded for various expansion chamber pressures, with the stagnation pressure held constant. A sample graph from this calibration procedure is shown in Figure 3-2 (page 56). As the expansion chamber is raised, the static pressure also rises, except for some range of expansion chamber pressures, where the static pressure was invariant. The center of this range was considered to be the expansion chamber pressure necessary to establish matched nozzle exit conditions, and the measured static pressure in this range was considered to equal the static pressure in the free stream for all subsequent runs at the indicated values of nozzle stagnation and expansion chamber pressure. In the

of up to two atmospheres have been obtained.

[2] See page 61 for more information on the nozzle.

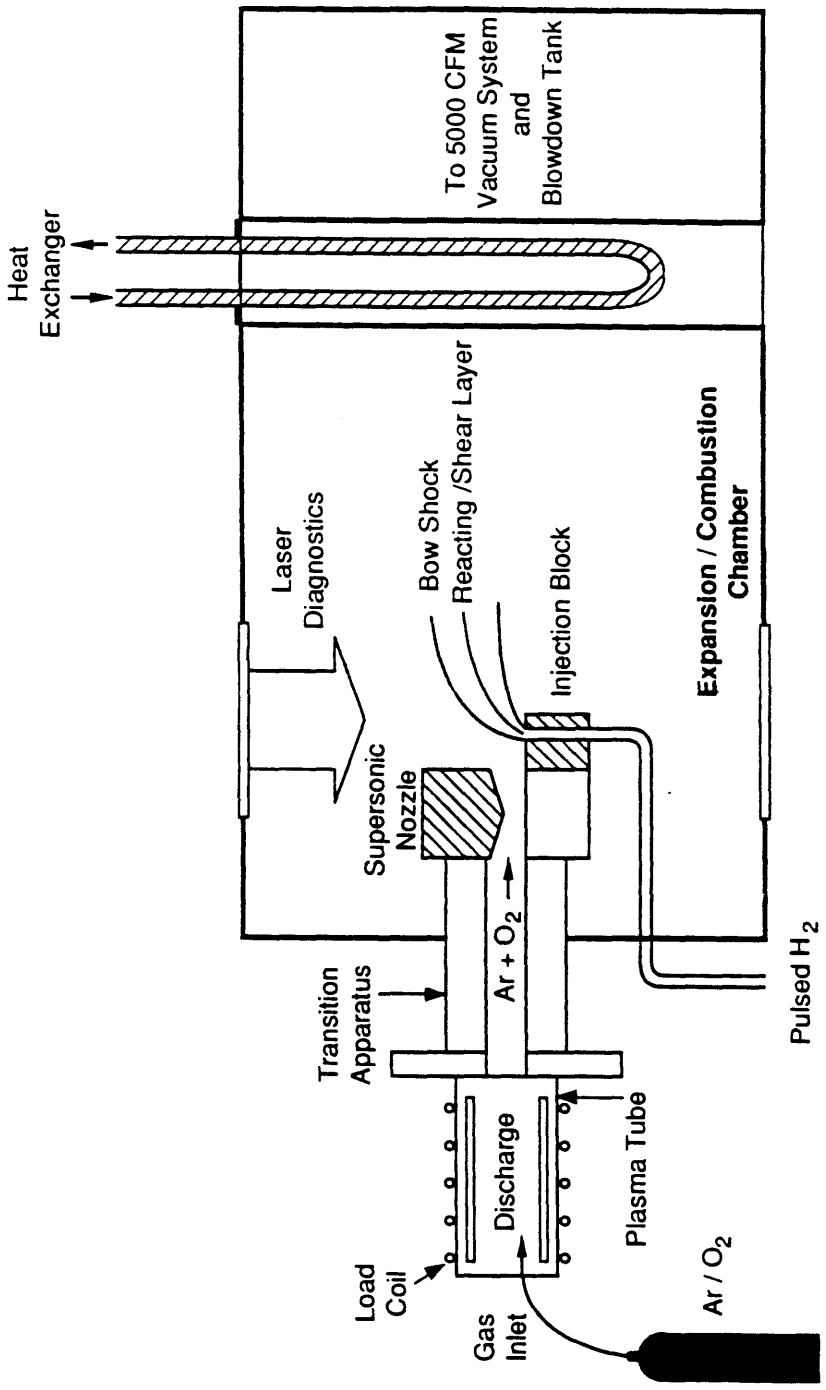

Figure 3-1: RF Discharge Driven Flow System Showing Transverse Injection Scheme

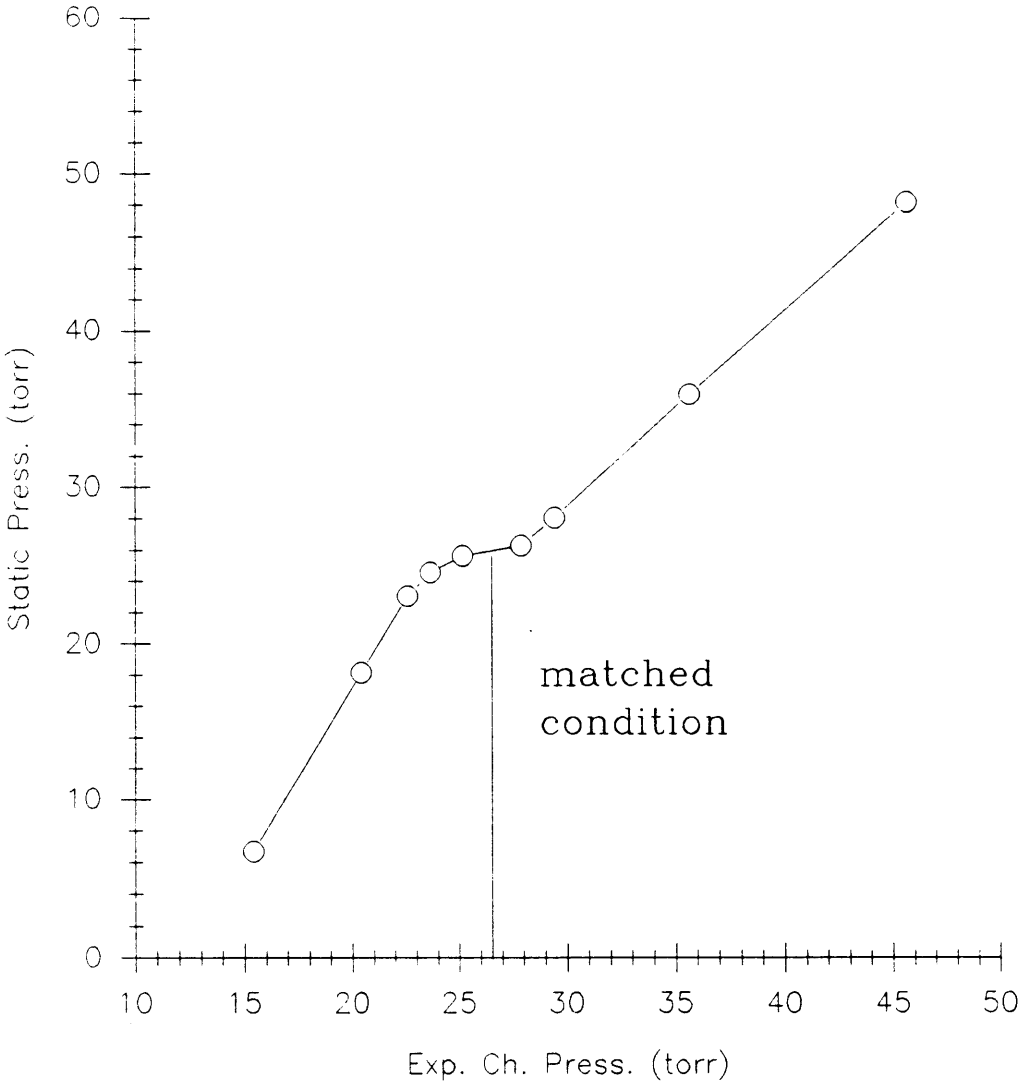

Figure 3-2: Static Pressure vs. Background Pressure, P_0=100 torr, T≈2500K

example given in Figure 3-2, the expansion chamber pressure needed for matched conditions (and hence the pressure at which data was taken) with a nozzle stagnation pressure of 100 torr is approximately 26 torr.

Once the free stream passes the end of the injector block it is influenced by gas recirculation in the expansion chamber. The H_2-O_2 combustion products and unburned gases then pass through a water-cooled heat exchanger. A liquid nitrogen trap, located downstream of the chamber, prevents pump oil from backstreaming into the chamber. The gases are finally exhausted by a 5,000 cfm (for pressures between 0.1 and 30 torr) pumping system consisting of two Kinney KMBD 2700 systems acting in parallel. Each system consists of two positive displacement pumps, a high-vacuum mechanical booster pump, and an oil-sealed, rotary-piston backing pump. The details of each of the components composing the flow system are given in the following subsections.

3.1.1 Plasma Tube

In general, radio-frequency (RF) plasma tubes rely upon a rapidly alternating magnetic field to induce eddy currents in the gas within the tube, thereby driving the gas to high temperatures with ohmic (I^2R_R) heating. A load coil, wrapped around the plasma tube and tied directly to the RF generator, supplies the power to the tube. When the coil is active, an alternating magnetic field is set up along the axis of the tube. This oscillating field in turn sets up circumferential eddy currents in the gas. The conductivity of the gas determines the strength and the location of these eddy currents, and hence the degree of ohmic heating. This heat addition is balanced by the normal mechanisms of heat transfer losses: radiation, conduction, and convection; but when the total heat input is high enough, the gas becomes ionized and a plasma is formed.

The plasma tube used for these studies represents a novel design.[81] The tube combines properties of both shielded and unshielded designs, yielding an easily ignitable tube with good plasma discharge stability demonstrated over a wide range of operating conditions. Before discussing this mixed design's characteristics, it is helpful to review the general properties of both the conventional shielded and unshielded plasma tube designs.

An unshielded tube is the most simple design for a plasma tube. In this type of plasma tube, a load coil is wrapped around a cylinder containing the slightly ionized gas. The unshielded tube's primary characteristic is an increase in plasma diameter with both increasing gas pressure and increasing input power. This expansion of the plasma is detrimental to prolonged operation because the plasma will eventually contact the enclosure, causing it to fail. Many schemes have been attempted to confine the

expanding plasma while cooling the enclosure, but none have been entirely successful over the desired range of operating conditions.

In contrast to the unshielded design is the shielded plasma tube. For this tube, there is no line-of sight path between the load coil and the plasma. The shield lowers the coupling efficiency of the coil to the plasma, which is in itself a disadvantage; but a secondary problem also arises. The size of the plasma is determined by a balance of forces between temperature (expanding) and electromagnetic (contracting). In the unshielded design, the expansion force increases faster than the electromagnetic pinching effect with increasing coil power, but in a shielded tube, the coupling is less efficient, and so the plasma actually shrinks as the power input is increased. Eventually, the plasma will disappear due to the electromagnetic pinch.

The tube used for this experiment uses a shield of overlapping segments (instead of a solid, one piece shield) to try to combine the two designs and strike a balance between the expanding and contracting forces on the plasma. Enclosing the segmented shield is an O-ring sealed (since the tube operates below atmospheric pressure) quartz tube, and around that is the load coil. The tube design is currently under patent review, and so its exact construction cannot be described, but one suggestion for the tube's performance (a stable plasma diameter as load coil power is increased) is that the segments in the shield locally ionize the gas, creating a constant source of conducting species to add to what would be a shrinking plasma.

Physically the tube is approximately 40 cm long, with the shield segments comprising 20 cm of its total length. The 12 copper segments of the shield are cooled with high pressure (150 psi) water entering and exiting from six fittings around the tube. The inside diameter of the shield is approximately 5 cm. A water-cooled copper plate fastens the tube to the transition assembly, which carries the hot gases to the nozzle inlet.

A 50 kW (Lepel Corporation, model T50) RF generator supplies power to the tube. The generator was typically operated at a frequency of 0.68 MHz, but it is capable of operating anywhere between 0.2 MHz and 1.0 MHz.

The plasma tube can sustain a discharge in Ar/O_2 at pressures up to 250 torr; but because of plasma instabilities (causing pressure fluctuations of up to 10%), 200 torr was the highest pressure at which data were collected. A picture of the plasma tube in operation is shown in Figure 3-3. The copper load coil is seen wrapped around the quartz tube and the shielding, and the many water cooling hoses running to various parts of the tube can be seen. During normal operation, the entire tube is encased in a rectangular box made of 1 inch thick polycarbonate shielding (to stop the ultraviolet radiation) and a metal screen (to protect from RF radiation). One side of the enclosure was removed for the picture.

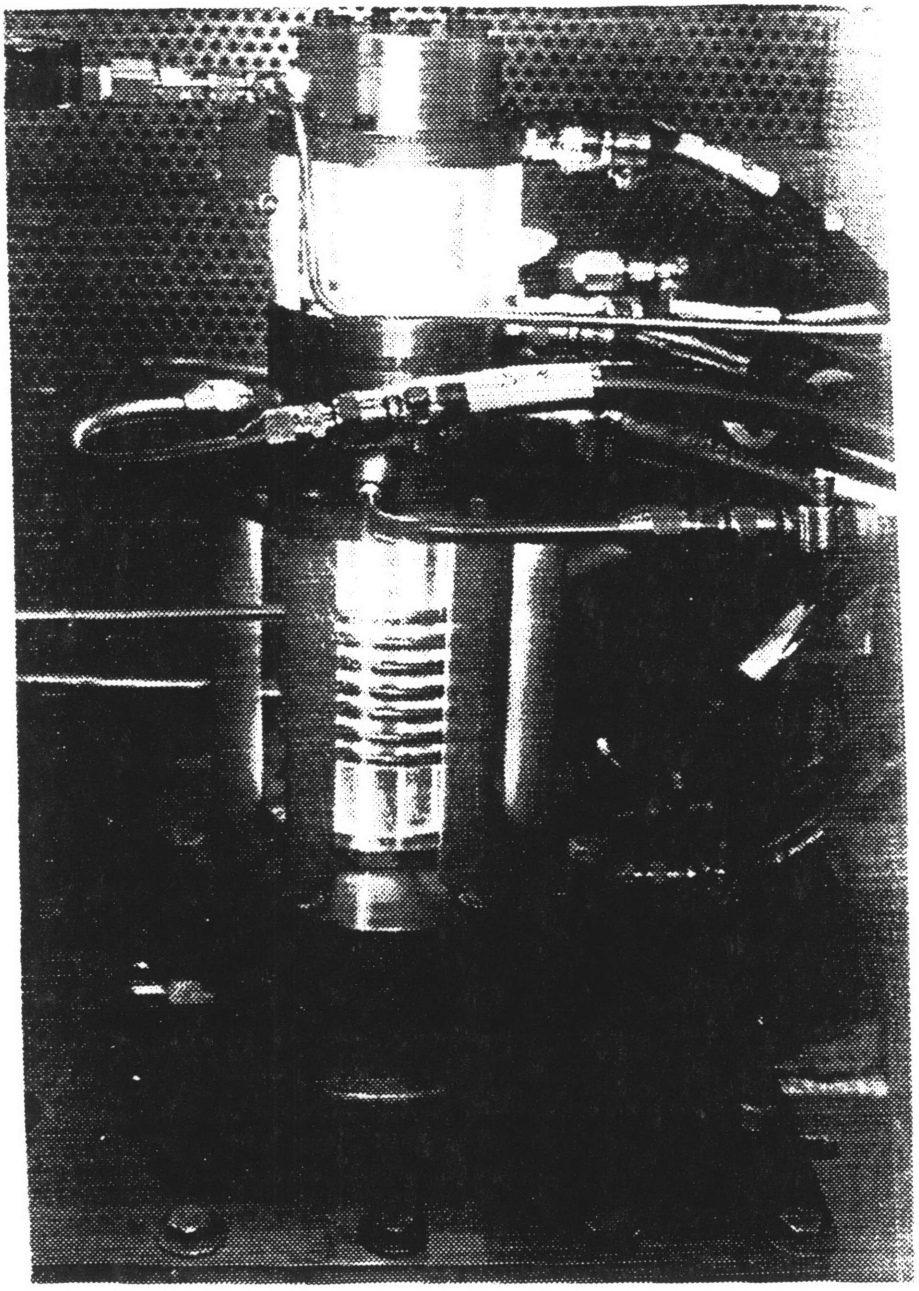

Figure 3-3: Plasma Tube in Operation

The observed efficiency of this tube is at least twice that of other shielded tubes. The efficiency was measured by recording the power supplied to the plasma tube with and without a plasma present. Typical efficiencies were on the order of 55%.

3.1.2 Stagnation Conditions

The gas-dynamic temperature (which is approximately the excitation temperature, the actual quantity measured) in the plasma itself is very high (5,000-10,000 K),[82] and the molecular oxygen is essentially totally dissociated. Equilibrium calculations show that even at 5000 K, only 0.27% of the oxygen remains in molecular form. As the gas traverses the 33 cm long transition apparatus to the nozzle, radiative and conductive losses cause the gas temperature to drop to the 2,000-2,500 K range. This temperature range is what is assumed to be the stagnation temperature for the flow.

In equilibrium the oxygen in the flow at these stagnation conditions would be almost entirely recombined into oxygen molecules, but the low densities (on the order of 10^{-5} gm/cm^3) prevent thermodynamic equilibrium from being reached before the gas is expanded through the nozzle. Using the SENKIN computer code[83] on a Cray YM-P computer, the mole fractions of argon, oxygen molecules, and oxygen atoms were computed for four different plasma tube pressures. The gas entering the plasma tube is composed of 80% argon and 20% oxygen molecules. With the assumption that the oxygen is fully dissociated, the gas leaves the plasma to head towards the nozzle entrance at a 66.7% mole fraction of argon and a 33.3% mole fraction of oxygen atoms. The results of these calculations are presented in Table 3.1.

Table 3.1: Stagnation Mole Fractions for Various Pressures; $\bar{u}_{TA} = 33$m/s

Tube Pressure	Ar	O_2	O	% recombination
75	0.669	0.00295	0.328	0.9%
100	0.670	0.00510	0.325	1.5%
150	0.674	0.0109	0.310	3.3%
200	0.679	0.0182	0.303	5.7%

This table assumes that the gas is flowing at 33 m/s between the plasma and the nozzle entrance. Not knowing this velocity exactly, another set of calculations was done for various flow velocities with the pressure at 200 torr. These numbers are presented in Table 3.2. It can be seen from this table that the amount of recombination is strongly dependent on the gas velocity, or, effectively, the amount of time the gas takes to traverse the transition apparatus. A speed of about 10 m/s is assumed to be a reasonable estimate, and so a stagnation (molar) composition of 70.3% argon, 5.4% oxygen molecules, and 24.3% oxygen atoms is assumed to be the maximum recombination of any of the experimental conditions used

(since lower tube pressures reduce the amount of recombination).

3.1.3 Supersonic Nozzle

A schematic of the supersonic nozzle used is shown in Figure 3-4. The nozzle is rectangular in cross section. The entire nozzle block is cooled with a separate high pressure (150 psi) water system. The cooling system was designed to remove up to 30,000 BTU/hr, keeping the copper nozzle well below the softening point of copper for nozzle stagnation temperatures as high as 5000 K. The supersonic section of the nozzle is fashioned as a half-nozzle for simplicity of construction as well as to provide a laminar flow over the surface of the injector block.

The composition of the gas (the amount of oxygen that is in molecular versus atomic form) going through the nozzle will affect its performance. To estimate the recombination fraction of oxygen as it passes through the nozzle, the flow through the nozzle was modeled using the SENKIN chemical kinetics code. The nozzle was approximated as a volume changing with time (see Appendix B). This is not entirely accurate, since the pressure changes in a nozzle will be substantially different than in this model, and the velocity was assumed to be linear in both the subsonic and supersonic section, which it is not. But such a calculation should give an upper bound on the amount of oxygen recombination in the nozzle, since in reality the extremely low pressures on the supersonic section will tend to create a frozen flow environment. With input conditions of 70.3% argon, 5.4% oxygen molecules, and 24.3% oxygen atoms, there was virtually no further recombination by the exit plane of the nozzle.

Thus a composition of 70.3% argon, 5.4% oxygen molecules, and 24.3% oxygen atoms is considered to be the composition throughout the nozzle and the experimental section. The value of gamma, γ, for such a mixture is 1.652, and it is this value that is used for all calculations.

A simple isentropic nozzle calculation for the ratio of the nozzle exit area, A_e, to the nozzle throat area, A^*:

$$\left(\frac{A_e}{A^*}\right)^2 = \frac{1}{M_a^2}\left[\frac{2}{\gamma+1}\left(1+\frac{\gamma-1}{2}M_a^2\right)\right]^{(\gamma+1)/(\gamma-1)}, \tag{3.1}$$

can be used to calculate an exit Mach number for this nozzle of 1.71. Pitot tube scans were done, and a static pressure was measured at the injection orifice. Using the isentropic relation

$$\frac{p_0}{p} = \left(1+\frac{\gamma-1}{2}M^2\right)^{\gamma/(\gamma-1)}, \tag{3.2}$$

in conjunction with pitot tube (impact pressure), p_0, and static pressure, p, measurements yields a Mach number of 1.5. Boundary layer growth within the nozzle is thought to reduce the effective flow area ratio

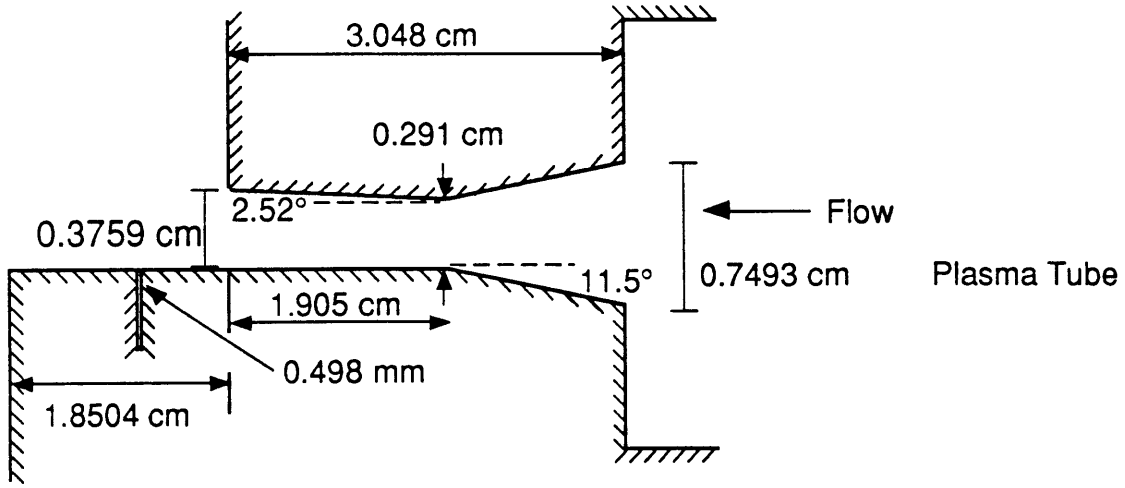

Figure 3-4: Schematic of Supersonic Nozzle

such that the final exit Mach number is less than predicted. CFD calculations for this nozzle supports this explaination.

3.1.4 Free Jet Expansion Chamber

The gas exiting the nozzle enters the rectangular expansion/combustion chamber whose pressure can be regulated. The chamber is constructed from aluminum with interconnecting copper tubing attached to the outside surface for cooling. The chamber has 16 window ports, four on each side. Some of the windows are of a racetrack design, offering good optical access to the combustion area. High-quality fused silica windows are used to ensure wide-range optical transmission.

A water-cooled heat exchanger is coupled directly onto the downstream flange of the expansion chamber. It can safely remove up to 150 kW of power in continuous operation. The throttle valve that controls the expansion chamber pressure is located immediately behind the heat exchanger.

3.1.5 Hydrogen Injection

A schematic of the injection block was detailed in Figure 3-4 (page 62). The orifice acts like a throat, choking the hydrogen flow, and so the hydrogen enters the expansion chamber highly under-expanded and at sonic velocities ($\approx$1,300 m/s). The hydrogen is brought to the block from a K bottle with several scram valves in the line to cut off the hydrogen flow in the case of an emergency. A fast-acting valve allows precise control over the amount of hydrogen injected in each pulse. This valve is controlled by an electronic pulse sent by a central control station, and was typically set to be open for 0.5 sec. Due to the long feed lines leading from the hydrogen bottle to the injector (the hydrogen bottle was located outside of the building because of safety considerations), there was a pressure drop of approximately 10% during the 0.5 sec pulse. Shorter pulse widths would certainly have helped this situation, but frame grabber board timing difficulties (see following section) prevented their use.

In the hydrogen line there is a Baratron pressure gauge and a fast-acting piezoelectric pressure transducer. The feed line between the Baratron gauge and the injector orifice is small, with a 1.24 mm ID, and so a calculation was done to determine the pressure drop between the measurement point and the orifice (a distance of about one foot). The equation for Poiseuille flow,

$$\Delta P = \frac{8\mu L Q}{\pi R_g^4}, \tag{3.3}$$

was used, where ΔP is the pressure drop along the line, μ is the viscosity of the hydrogen gas, L is the length of piping, R_g is the radius of the feed line, and Q is the volumetric flow. The estimated pressure

drop along the lines of the feed system used in the experiment is only 0.015 atm. For the smallest injection pressure used here, 450 torr, this amounts to a pressure loss of 2.5%.

3.2 Imaging System

Referring back to Figure 2-11 (on page 28), the main components of the imaging system can be seen. A laser system produces pulses of light that can be tuned in frequency to a molecular transition of interest, and a train of optics both directs as well as forms the beam into a sheet. A camera collects light perpendicularly to the direction of the beam's propagation. The specifics of the imaging equipment used for these experiments are discussed below.

3.2.1 Lasers and Optics

The dye laser pump laser is a Quanta Ray Nd:YAG Q-switched laser. The laser produces 10 nsec wide pulses of up to 1 J of energy at a wavelength of 1.06 μm. This beam is sent through a HG-2 harmonic generator to double the frequency, creating a green beam at 532 nm with $\approx$250 mJ of energy. This beam then pumps Rhodamine 590 (a laser dye) in a Quanta Ray PDL-3 dye laser. The output of the dye laser is tunable, and it is set to $\approx$568 nm (in the yellow). At this wavelength, the energy contained in the beam is 30-80 mJ. The last stage in the laser system is a WEX wavelength extender with a crystal suitable for doubling the dye laser output into the ultraviolet at 284 nm with 3-15 mJ of energy.

The uv light from the WEX is sent through several beam telescopes (each composed of two 1" right angle quartz prisms) until it was directly above the top window of the expansion chamber. As the cylindrical beam is sent downward, it passes through 2 cylindrical lenses (one +10 cm and the other -10 cm in focal length) and a spherical lens (15 cm focal length), producing a sheet of light approximately 0.5 mm $\times$ 35 mm in cross section at the injector block. This final stage of optics is displayed schematically in Figure 3-5. The maximum focus of the beam was set at the injector block, and the beam was aligned to illuminate the region directly above the injection orifice. The plane of illumination extended lengthwise from just upstream of the orifice to well past the end of the injector block.

3.2.2 Detector

A Xybion (model ISG-250-U-3) uv intensified CCD camera is used to image the fluorescence. A Nikkon 105 mm, f/4.5 quartz lens with a Nikkon (PK-13) extension tube focuses the fluorescence emission from the combusting flow onto the detector. The camera was set with a 30 nsec gate width, centered over

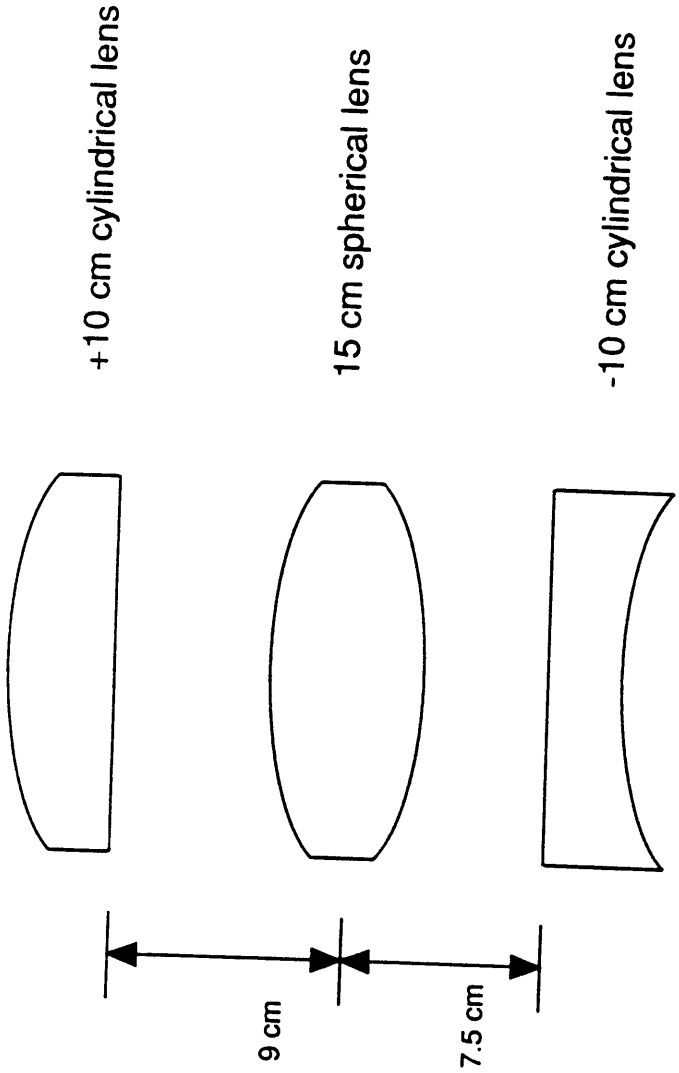

Figure 3-5: Schematic of the Sheet Forming Optics

the laser pulse. Such a short gate width effectively eliminates background light (such as the room lights or emission from the plasma discharge). The scattered laser light was filtered out by a WG-295 filter. The camera produces an image comprised of 696 x 240 pixels. The area imaged by the camera was approximately 1.51 cm x 1.21 cm, giving an area per pixel (and hence a limit on the spatial resolution) of 22 μm x 51 μm. This compares well with the resolutions achieved by previous studies (pixel sizes of 60 x 60 μm[21,77] and 25 x 25 μm[68]).

3.2.3 Computer Storage, Processing, and Timing

The entire imaging system was precisely timed using a SRS delay generator (model DG535) and three pulse generators (a Systron-Donner 100A, a Systron-Donner 100C, and a Nanofast dual delay generator, model 568). The 100C pulse generator provided a 10 Hz trigger for the SRS. The SRS then triggers the Nanofast, which fired the Nd:YAG laser flash lamps and $\approx$ 245 μsec later the laser's Q-switch. Another output of the SRS triggered the CCD camera, just slightly before the Q-switch fired. When the hydrogen valve was opened with a (manually initiated) pulse from the Systron-Donner 100A, the frame grabber board (EPIX Silicon Video MUX), interfaced with an IBM XT microcomputer, would capture and save two images taken approximately 1/ 60^{th} of a second apart. A schematic of the cascaded timing sequence is shown in Figure 3-6.

The post image processing was different for the penetration depth study and the temperature mapping. For the jet penetration work, multiple images of the reacting flow recorded for the same conditions were captured, averaged, and contrast enhanced. They were then transferred to a SUN Spark station for false color addition and color printing. Hardcopy printouts (8 1/2" x 11") of each average were then used to digitize the penetration depth profile using a Jandel Scientific digitizing tablet. Curve fits and hardcopy printouts were then produced using commercial software (SigmaPlot by Jandel Scientific).

For the temperature mapping, a color version of the EPIX Silicon Video MUX board was used. Again multiple images were captured; 20-30 images at identical pressures for each of the two transitions (which are described in section 3.3.2) used. These were averaged and then smoothed using EPIX SVIP software. A BASIC program calculated a temperature at each pixel by taking the ratio of the two averaged images. The computed temperatures were re-loaded into the SVIP software where false color and legends were added.

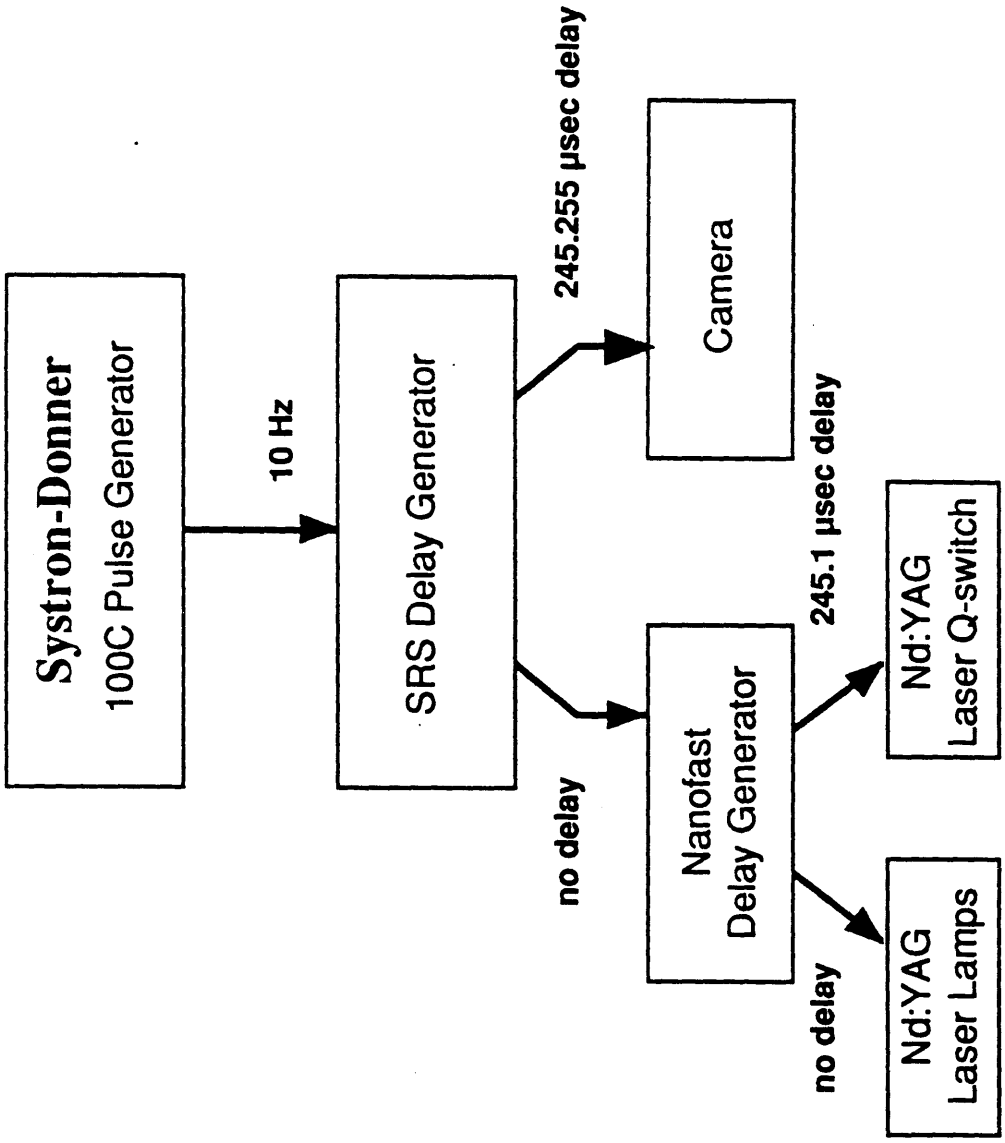

Figure 3-6: Schematic of the Timing Sequence

3.3 Procedures

3.3.1 Chemiluminescence Experiments

Initial experiments centered upon imaging chemiluminescence from OH in the supersonic reaction zone. Chemiluminescence refers to the photons given off by the molecules as they drop from a thermally and/or chemically excited state to a lower state. Chemiluminescence from excited OH is emitted in the uv (<320 nm) and is not visible to the naked eye. The uv intensified camera, however, was sensitive enough to image it.

The experimental setup and procedure were almost the same for the imaging the chemiluminescence as were employed for the PLIF imaging. There were only two differences between the procedures used for two studies. To collect enough chemiluminescent light, the camera gate was opened for long periods (20 msec), and so the pictures taken represent a signal integrated in time and in space (over the line of sight). No laser beam was utilized for the luminescence studies.

The main disadvantage of the chemiluminescence for imaging diagnostics is the lack of temporal resolution and the spatial integration of the produced emission. The PLIF technique relies on short pulse-width lasers and fast decay fluorescence signals so the camera gate can be kept short, resulting in temporally resolved images. In addition, the laser sheet produces a 2-D spatial image of the flow. The chemiluminescence experiments, however, provide a good test of the equipment, and of the timing sequence; and it verified that OH is being produced in the combustion region. Images of the chemiluminescence are shown and discussed in the Results chapter.

3.3.2 OH Spectroscopy

To move from imaging OH chemiluminescence to PLIF, the laser beam must be introduced and be tuned to a precise transition wavelength of OH. To identify that the correct transition was being excited, an acetylene/air diffusion flame was used. Initially, the laser beam was passed through the flame, and an image of the flame was focused onto the entrance slit of a 1/3 meter monochromator. The exit slit of the monochromator was set to about 3 mm, so that most of the broadband emission would be collected by a photomultiplier tube (PMT) positioned at the exit. The signal out of PMT was sent to a boxcar averager and then to a strip chart recorder. The grating in the monochromator was adjusted such that emission at all wavelengths within about 10 nm of 310 nm was collected.

Once the optics and the timing were set properly, the dye laser frequency was scanned at a constant rate. The absorption (or excitation) spectra from the flame was captured and recorded on the strip

chart. The measured spectra was matched to a calculated OH spectra, calibrating the dye laser tuning so that the desired transition could be excited.

For the jet penetration study part of this experiment, the $Q_1(7)$ line in the (1,0) band of the $A^2\Sigma^+$ electronic state was the target transition. This line was chosen because of its large signal strength, its accessible wavelength (283.2195 nm) with the doubled dye, and its relative insensitivity to temperature. This last characteristic is important in interpreting the images as relative concentration maps. If the signal strength depended strongly on temperature, hot regions with a smaller OH concentration could conceivably show up with a stronger signal (and hence be thought to have a higher OH concentration) than a cooler region that actually does have higher OH levels.

The scanned spectrum and the calculated spectrum of OH around the $Q_1(7)$ line in the $A^+\Sigma^2$ (1,0) state can be compared in the graphs of Figure 3-7.

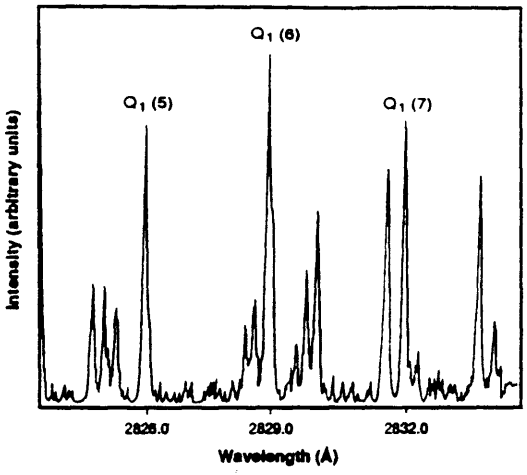

(a) Partial Experimental OH Fluorescence Excitation Spectrum Around $Q_1(7)$

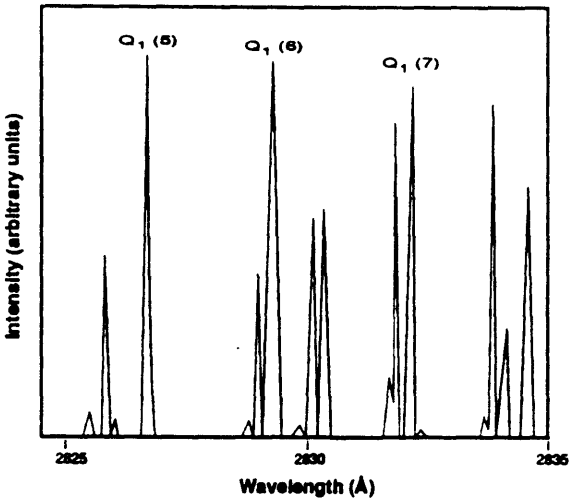

(b) Partial Calculated OH Fluorescence Excitation Spectrum Around $Q_1(7)$

Figure 3-7: Partial Calculated OH Fluorescence Excitation Spectrum for Jet Penetration Study

Table 3.2: Stagnation Mole Fractions for Various Gas Velocities; P_0=200 torr

Gas Velocity (m/s)	Ar	O_2	O	% recombination
33	0.679	0.018	0.303	6.0%
10	0.703	0.054	0.243	18.3%
3	0.727	0.090	0.183	32.0%
0.3	0.779	0.169	0.052	76.6%

3.3.3 Jet Penetration Data Collection

Once the laser is tuned to the desired transition in a stationary flame, the beam is sent into the combustion chamber. The tuning is then manually adjusted (over fractions of an angstrom) to maximize the PLIF image's intensity.

For collecting jet penetration data, the standard operating procedure is to maximize the laser output, check the laser alignment, and then start up the flow system. Two parameters were varied during the course of this investigation, namely the hydrogen injection pressure and the free stream pressure. P_{H2} was varied from 450 to 1000 torr, and P_{FS} from 12 to 55 torr (corresponding to nozzle stagnation pressures of 75 to 200 torr). For each value of P_{H2} and P_{FS}, two to six PLIF images were taken and stored. Then a new data point was set, and more images taken. Dynamic pressure ratios[3] investigated cover the range 5.9 - 38.6. The dynamic pressure ratios established for each set of injection and free stream pressure is given in Table 3.3. An "X" in the table means that no experiment was performed for those conditions.

Table 3.3: Dynamic Pressure Ratios Established for Various Injection, P_{H2}, and Free stream, P_{FS}, Pressures

P_{FS} (torr)	12	26	39	55
P_{H2} (torr)				
450	17.4	8.0	X	X
500	19.3	8.9	X	X
550	21.2	9.8	X	X
600	23.2	X	X	X
650	25.1	X	7.7	X
700	27.0	12.5	8.3	5.9
750	29.0	X	8.9	6.3
800	30.9	14.3	9.5	6.7
850	32.8	15.1	10.1	7.2
900	34.7	16.0	10.7	7.6
950	X	16.9	11.3	8.0
1000	38.6	17.8	11.9	8.4

[3]The dynamic pressure ratio is the most important parameter in determining jet penetration. It is defined and discussed in the Background chapter, specifically on page 10.

3.3.4 Temperature Mapping

OH Spectroscopy

Before the temperature studies were begun, several OH fluorescence excitation scans were recorded to definitively locate the two ro-vibrational lines that were used to establish the required intensity ratios; namely the $R_1(3)$ (at 281.2144 nm) and $Q_1(10)$ (at 284.3261 nm), lines, both in the $A^2\Sigma^+$ (1,0) band. The dye laser was again passed through a flame and the generated emission was imaged onto a PMT through a monochromator. These two lines were also used by previous researchers[49] to determine temperatures because of their good energy separation (the lines are separated by 0.22 eV, whereas 2500 K is 0.21 eV), their sensitivity to temperature over the range of interest, and their strong signal strengths subsequent to excitation. Comparisons of the calculated and recorded fluorescence excitations are presented in Figure 3-8.

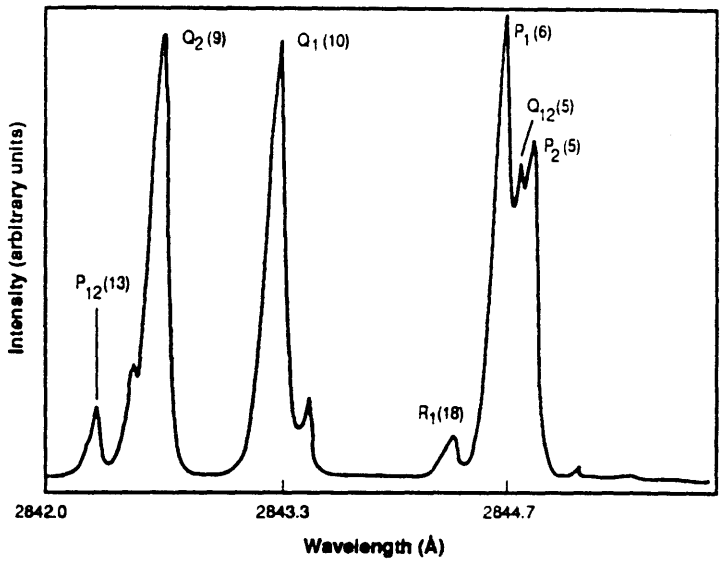

Partial Experimental OH Fluorescence Excitation Spectrum Around $Q_1(10)$

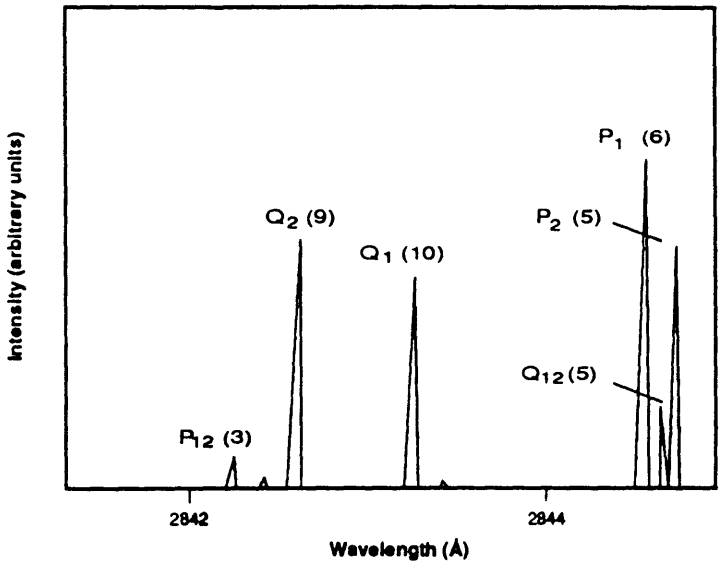

Partial Calculated OH Fluorescence Excitation Spectrum Around $Q_1(10)$

Figure 3-8: Partial Experimental and Calculated OH Fluorescence Excitation Spectrum for Temperature Study, $Q_1(10)$ Line Assignment

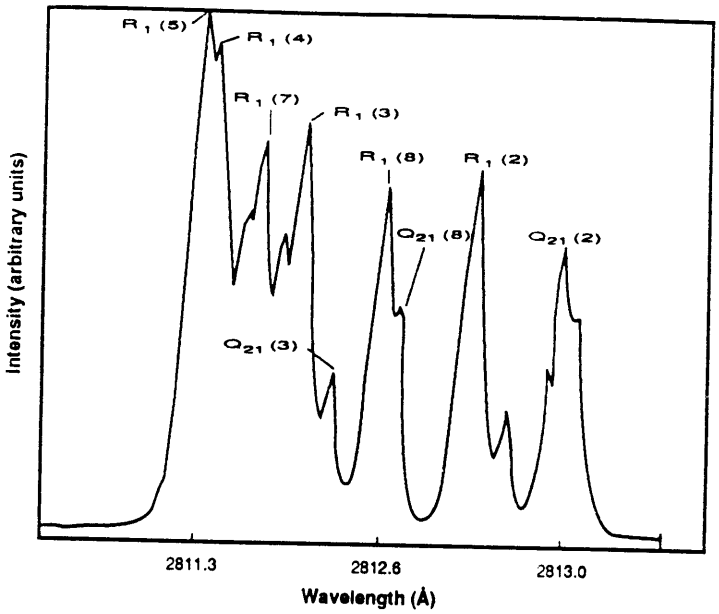

Partial Experimental OH Fluorescence Excitation Spectrum Around $R_1(3)$

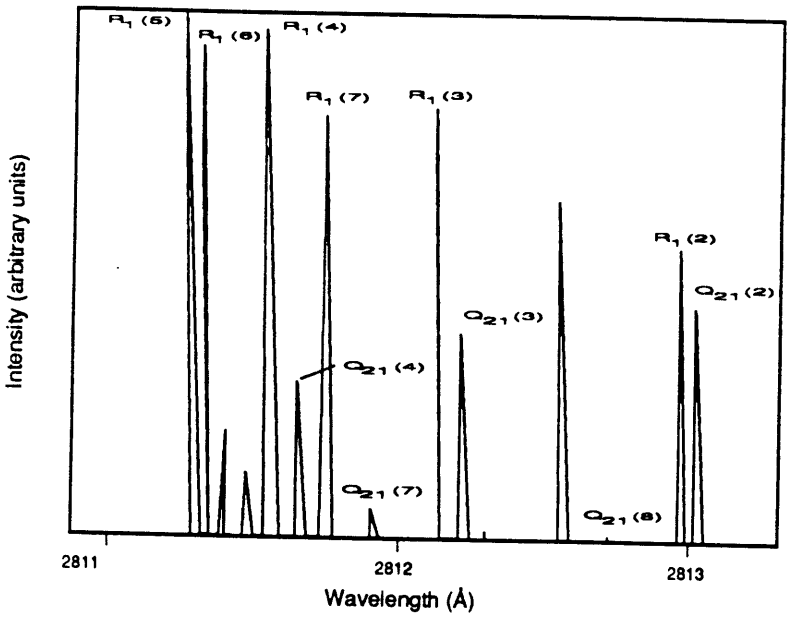

Partial Calculated OH Fluorescence Excitation Spectrum Around $R_1(3)$

Figure 3-8 (continued), $R_1(3)$ Line Assignment

Data Collection

The same procedure was used to capture the images for the temperature studies as for the flow visualization/jet penetration experiments. Thirty images were recorded of the emission generated after excitation of each of the two lines, and then were averaged to remove any turbulence effects or shot-to-shot differences (*ie.* the pressures or the laser beam intensity profile). The intensity of every pixel in the resulting average images was saved to a file. A computer program was written to read in the averaged image files; and from the ratio of pixel intensities a temperature was computed at every point. The program used for this calculation is given in Appendix C on page 132.

The temperature was computed using captured flurescence intensity ratios and Equation 2.44b.

$$T = \frac{E_2 - E_1}{k \ ln\left[\frac{g_2(2j_2+1)}{q_1(2j_1+1)}R\right]}, \tag{2.44b}$$

where $Q_1(10)$ is line # 2 and $R_1(3)$ is line # 1, R is the ratio of fluorescence signal strengths measured from excitation of $R_1(3)$ over that from $Q_1(10)$, q_i is the relative line strength, and j_i is the angular momentum. Table 3.4 displays the values of these spectroscopic properties for the two lines.

Table 3.4: Spectroscopic Constants for $Q_1(10)$ and $R_1(3)$

	$Q_1(10)$	$R_1(3)$
E (cm^{-1})	2019.633	201.922
q	2.5253	20.9745
j	10	3

With these values the resulting expression relating the ratio of pixel intensities to a temperature is

$$T = \frac{2615.4}{ln(R) - 1.02}. \tag{3.4}$$

Chapter 4

Results and Discussion

4.1 Chemiluminescence

A photograph of the OH chemiluminescence is shown in Figure 4-1. A small region of combustion (indicated by a small amount of excited OH emission) is noted near the jet orifice. The initial portion of the combusting H_2 jet shows up dimly on the right side of the picture. This lack of hydroxyl radicals could be due to two reasons. First, the hydrogen is injected at room temperatures, and so it will take some time for it to heat up to ignition temperatures. The flow is very fuel rich (about 157 times more hydrogen molecules than the stochiometric ratio for this case), and so there are large amounts of cold hydrogen that may be reducing the temperature. And secondly, there may be insufficient mixing at that point of the flow for combustion to occur.

As the jet continues downstream (towards the left in the figure), there is a region of little or no combustion; presumably where an expansion wave lowers the density of the gas below a level that can support combustion. Farther downstream significant chemiluminescence is noted, presumably where the flow is slightly re-compressed, causing the combustion to begin again in earnest.[1] Because of the spatial integration along the line of sight, the image shows OH present solidly between the upper boundary of the H_2 jet on top and the injector block on the bottom. The combustion is actually a 3-D phenomenon, with the hydrogen mixing and burning in a shell, with an un-reacting center region. Because of the projection of this 3-D phenomenon onto two dimensions, viewed at a right angle the combustion seem to be occurring uniformly between the injection block and the top of the jet.

[1] The expansion/compression wave structure has been noted by researchers running CFD codes.[22]

4.2 PLIF Images

A representative, averaged, contrast enhanced[2] image is shown in Figure 4-2 (page 87). For this picture, the stagnation pressure was 100 torr, giving a free stream pressure of 26 torr, and the injection pressure was 700 torr. These values, along with a value of gamma of 1.652, give a q (the dynamic pressure ratio) of 13.0. This image is of the fluorescence generated subsequent to excitation of the $Q_1(10)$ line (one of the ro-vibrational lines used for the temperature study).

This figure shows the characteristic jet trajectory of a rapid penetration[3] as the under-expanded jet leaves the orifice, and then a more gradual penetration as the jet continues downstream. There seems to be a region where the combustion extinguishes (where no OH is detected), and then the combustion seems to re-ignite. This is as was seen in the chemiluminescence images; where it is thought that a weak compression/expansion wave reduces the density of the gas, causing the combustion reacting to stop; and then re-compresses it, causing it to re-ignite (as was also seen by Takahashi and Hayashi[22]).

The edges of Figure 4-2 are somewhat ragged. Because this image represents an average of 30 individual images, any turbulent structure originally present should have smoothed out. Figure 4-3 (P_{H2}=700 torr, P_{FS}=26 torr; different camera position than used in Figure 4-2) represents a single-shot image. It can be seen that the signal is not uniform at all across the shear layer mixing region. This may be because of the very low densities in the combustion region,[4] causing only a small amount of OH production, and hence limited fluorescence emission production. Thus, it appears that more than 30 images are required to fully remove the "graininess" that is observed in Figure 4-3, and it is thought that this graininess is the major cause of the ragged edges in the averaged image.

4.2.1 Injection Depth Penetration

General Comments on the Jet Penetration Results

As was mentioned in the section describing the plasma tube, the highest stagnation pressure used was 200 torr. At this pressure in the plasma tube, the pressure in the expansion chamber was 55 torr. This low pressure means a concomitantly low density of oxygen. In general the jet penetration studies were performed under very fuel rich (between 74 and 480 times more hydrogen molecules then oxygen atoms) conditions. The high fuel/oxygen ratio suggests that, at least in the initial stage of the injection

[2] Contrast enhancement in this case simply means multiplying the pixels intensities by a constant to make them brighter.
[3] Presumably to the Mach disk - see Theory section.
[4] A simple analysis shows that in the combustion region an approximate value for the OH production rate is on the order of 6×10^{21} moles/cm^3/sec.

process, the jet penetration may not be significatly influenced by the combustion process, *ie.*, the flow field studied here may be considered a non-reacting flow. Lee *et al.*[21] observed a lower penetration of their reacting jet than equivalent non-reacting jets, and they point to fuel consumption by combustion as a possible reason. But with injection under very fuel-rich conditions, the total fuel consumption should be small enough to not greatly affect the jet's penetration.

By looking closely at Figures 4-2 and 4-3, it is noted that at large x/d, where the combustion has re-ignited, the reacting shear layer is actually expanding; essentially resulting in deeper jet penetration. If a smooth trajectory is visually extended from the penetration as the jet turns, it seems to be slightly lower than the actual edge delineated in the downstream region. Local heating and expansion of the gas due to chemical reactions in that region seems to explain why this penetration enhancement should occur.

Measured Trajectories Without Empirical Curve Fitting

During the course of this study, 35 different jet penetration trajectories were measured. The trajectories are presented in four different groupings, one for each of the four free stream pressures used, and are found in Figures 4-4 through 4-7 (on pages 89 to 92). It is evident that some of the trajectories do not extend as far in x/d as others. The reason is that for images taken at the high free-stream pressure (55 torr), the fluorescence intensity was very low, and a reliable trajectory could not be digitized any further downstream than is presented. Quenching by water molecules (the final product of H_2+ O_2 combustion) or reactions with O atoms[5] can occur are the most likely reasons for the reduced fluorescence intensities.

In general, the trend represented by the trajectories is that higher values of dynamic pressure ratio results in deeper jet penetration into the free stream , as would be expected. This trend is not adhered to universally, however. Some of the closely grouped trajectories have curves with lower values of q penetrating deeper than curves for higher q values. These differences do not exceed experimental error, however.

Empirical Relations for the Data of the Present Study

As was mentioned in the Cold Flow Experiments section (Section 2.1.2), a power law of the form

$$\frac{y}{d_i} = aq^b \left(\frac{x}{d_i}\right)^c \tag{2.17}$$

[5] Just as a molecule can be collisionally quenched, the excited species can react chemically before emitting a fluorescence signal. Oxygen atoms in the free stream can react with hydroxyl radicals to cause this chemical quenching.

has been used extensively to fit supersonic jet penetrations. Table 2.2, which listed the parameters a,b,c determined though other experiments, is reproduced here with the values established from the results of the present study. The equation that best fit the data taken here is,

$$\frac{y}{d_i} = 2.173q^{0.276}\left(\frac{x}{d_i}\right)^{0.281} \tag{4.1}$$

Table 4.1: Empirical Power Law Equations for Jet Penetration

Researcher(s)	a	b	c
Broadwell & Breidenthal[17]	2.200	0.333	0.333
Vranos and Nolan[13]	1.680	0.500	0.087
Rogers[14]	3.870	0.300	0.143
Faucher *et al.*[18]	1.854	0.392	0.292
This work	2.173	0.276	0.281

As can be seen in Table 4.1, there is a wide variation in the power law constants, with those for the present study falling within bounds set by the others. The values quoted as a part of this work were found using the Marquardt-Levenberg algorithm to fit Equation 2.17 to over 750 sets of data (each data set was comprised of a y/d, and x/d, and a q).

A second empirical curve, proposed by McDaniel and Graves[15] (again for a non-reacting flow), of the form,

$$\frac{y}{d_i} = q^a ln\left[b\left(\frac{x}{d_i}+c\right)\right], \tag{2.22}$$

was also used to fit the same 750 data sets from this present study. McDaniel and Graves found the best fit was established for their experiments with a, b, and c equal to 0.344, 2.077, and 2.059 respectively. The jet profiles from the present study are fit best with the equation,

$$\frac{y}{d_i} = q^{0.3015} ln\left[4.704\left(\frac{x}{d_i}+0.6373\right)\right]. \tag{4.2}$$

Figure 4-8 (beginning on page 93) displays actual measured trajectories (from this study) together with trajectories predicted using the two empirical relations found for the current data (Equations 4.1 and 4.2). Many of the jet boundary profiles match the empirical fits very well, whereas some differ up to 30%. Some trajectories (q = 5.9, 6.7, 7.2, 9.8, 17.4, 19.3, 21.2, 25.1, 32.8, 38.6) are over-predicted by the empirical relations, while others (q = 9.5, 10.1, 12.5, 14.3, 15.1, 16.9) are under-predicted. It seems that the trajectories measured for middle values of q are higher than the predictions, and trajectories resulting from low and high values of q are lower; but except for a few cases, the fits are quite good.

Because the equation forms that predict non-reacting, normal injection flows provide adequate fits to the data from this study, the idea that this flow (which is very fuel rich) is behaving like a cold flow is supported.

In the first three graphs in Figure 4-8, a small depression can be noted in the measured jet trajectory. This depression is thought to be due to the shear layer density reduction in that area, as is seen in Figure 4-2. As the trajectory was digitized, the lack of fluorescence signal in the area immediately after the jet is turned creates an apparent dip in the jet boundary.

An additional method of judging how well these two "universal" empirical formulas fit the penetration trajectories is to plot the actual measured y/d values vs. the y/d values predicted by the empirical fits. If the empirical fits were perfect, the graph would be a straight line. Six plots, two for each of the high, medium, and low values of q (one each for Equations 4.1 and 4.2), of this type are given in Figure 4-9.

All six plots show reasonable collapse of the data points onto the straight line. The lower values of y/d (those closer to the injector orifice) seem to be better predicted than higher values, over all values of q.[6] Trajectories measured for middle and low values of q ($10 < q < 17$ and $q \leq 10$) are better predicted by Equations 4.1 and 4.2 than those from higher or lower values of dynamic pressure ratio, throughout the range of x/d_i. By using Equations 4.1 and 4.2, the jet trajectories in the middle range of q are predicted to within 8% of the measured values. Penetration heights measured for high and low ranges of q are in general predicted to within 16% and 8% respectively. The power law equation, Equation 4.1, is noted to be slightly more accurate in predicting the measured trajectories, in general being with 8% for low values of q, whereas Equation 4.2's predictions are only within 13%.

Comparison to Empirical Relations found by Previous Researchers

The various graphs in Figure 4-8 compare individual trajectories to the curves that optimally fit the data of this study. To compare the data of this study to previous research, the empirical curves, Equations 2.17 and 2.22, (with the a, b, and c parameters that the others investigators used) are plotted along with the penetration data measured in this study in Figure 4-10. The different coefficients used in the power law relation are tabulated in Table 4.1 on page 80.

The data from this current study fairly ubiquitously falls in the space between some of these other equations. The subsonic curve, and the power law equations found by Rogers[14] and Faucher *et al.*[18] predict penetrations higher (up to 67% higher) than what was measured for this present work. The power law found by Vranos and Nolan[13] gives the lowest predicted penetration trajectories, 10-50%

[6] Perhaps because the jet is truly cold there.

lower the measured curves. The logarithmic equation used by McDaniel and Graves[15] (Equation 2.22 with values of a, b, and c that they used) is consistently the closest to the present data. The data curves are typically higher than curves generated by the McDaniel and Graves equation (some plots show this trend reversed), differing by 5-25%. The large variation in trajectories shown in these plots is most likely caused by variations in experimental conditions between the various research groups. As was discussed in the Background chapter, variables other than q (such as boundary layer thickness and free stream Mach number) may be influencing the trajectories that each research group has measured, and hence the determinations of the parameters a, b, and c.

Comparison to Theoretical Prediction

Back in the Normal Injection section of the Background chapter, a theoretical jet penetration was predicted using the equations of Schetz and Billig. This prediction used a value of $q = 13.0$. The predicted trajectory is compared to the actual trajectory (for comparable q) in Figure 4-11 (on page 126).

The theory predicts a much flatter trajectory for larger values of x/d (> 12) than the measured data shows. This could be caused by the boundary layer in the experiments, which effectively lowers the pressure the injectant encounters as it enters the free stream, and hence the jet penetrates farther.[7] When Schetz and Billig[2] compared their theory to subsonic data, they also found that it under-predicted penetrations for high values of q. A plot they made comparing their theory to subsonic data was given in the Background Chapter (Figure 2-3 on page 12).

Conclusions

Empirical equations found for the jet penetration data collected in this study generally predict to within 16% (over the entire range of experimental conditions) the experimentally measured penetrations of sonic jets entering a supersonic free stream with very high values of dynamic pressure ratio. Because of the good fit to this data by equations whose form was first derived for cold flows, and because of the high hydrogen to oxygen ratio, the reacting flowfield investigated here seems to be adequately approximated as a non-reacting flow. The data falls within bounds delineated by previous researchers.

Based on previous theoretical and experimental work and on the data collected here, the dynamic pressure ratio is the dominate factor in determining jet penetration profiles. However other variables may influence the jet trajectories. For example boundary layer thickness and/or the separation of the boundary layer could influence the effective pressure encountered by the emerging jet. Papamoschou

[7] The theory ignores boundary layers.

et al.[16] has stated that the definition of the dynamic pressure ratio, $(\gamma PM^2)_{FS}/(\gamma PM^2)_{jet}$, may not sufficiently predict the influence of variables such as the free stream Mach number on the penetration of the jet.

For the work performed in this study, the recommended empirical relation which best described the penetration trajectory has the form:

$$\frac{y}{d_i} = 2.173q^{0.276}\left(\frac{x}{d_i}\right)^{0.281} . \tag{4.3}$$

4.2.2 Temperature Mapping

Temperatures were calculated for an injection pressure of 700 torr and a free stream pressure of 26 torr. A computed local temperature map of the flowfield is shown in Figure 4-12. The temperature range depicted is from 880-2600 K. Both because the emerging jet is blocking the flow (slowing and hence heating the flow as it approaches stagnation conditions) and the heat added by the combustion reactions, a hot zone is created close to the injection orifice. As the jet is turned, the density in the shear layer drops, causing the combustion to extinguish. This is similar to the reduced reaction rates and temperature drop found in the same region by the Takahashi and Hayashi[22] in a computer simulation of a slot injection scheme (the temperature contours they calculated is show in Figure 2-9). Farther downstream, the density rises and the reaction re-ignites (causing the temperature to rise also). The flow in this downstream region has a hot core, with the temperature dropping off towards the top and bottom edges of the jet. The temperature gradient along the upper edge of the jet is smaller than along the bottom edge, and this again can be seen in the computations shown in Figure 2-9.

The region close to the injection orifice has been expanded and is displayed in Figure 4-13. One interesting feature of this figure is that the very hot regions are scattered somewhat. This scatter may mean that the mixing and heating of the cold hydrogen is still occurring.

The temperatures calculated from the PLIF measurements have not been benchmarked or calibrated against other temperature measurements (such as thermocouple measurements or rotational spectra calculations). Previous researchers who have used PLIF to measure temperatures[49, 74] (see section 2.2.8) have found that the PLIF-derived temperatures are systematically 100-200 K too high (as judged by radiation corrected thermocouple measurements). Typical peak temperatures measured in hydrogen-oxygen flames range from 1800-2000 K.

There are two main sources of error in the temperature calculations presented here. One reason that the temperatures calculated here seem high could be that the technique used is based on the assumption

that the gas is in equilibrium.[8] Because of the low densities in the combustion region (on the order of 10^{17} molecules/cm^3), however, the rotational temperature may differ from the actual gasdynamic or kinetic temperature. Nevertheless, the 2-D temperature map illustrates the potential utility of a laser diagnostic (namely PLIF) for determining temperatures in high-speed, reacting flows.

4.3 Summary

Hydrogen, at pressures ranging from 450 to 1000 torr, was injected transversely into a Mach 1.5, ≈1400 K, oxygen-containing free stream. The correlation between the injection and free stream pressures and the jet penetration trajectory was studied. A 2-D temperature map of the flowfield was also determined. Planar laser-induced fluorescence was the primary diagnostic technique used for these studies. A sheet of laser light illuminated a cross section of the flowfield, exciting specific ro-vibrational state of the hydroxyl radical. The fluorescence emitted as these excited OH molecules relaxed into lower energy levels was imaged at right angles to the plane of illumination by a uv-intensified CCD camera.

The images recorded were used to measure the jet penetration height as a function of downstream distance for many values of jet and free stream pressures. As previous works have shown, the primary factor influencing the jet penetration is the dynamic pressure ratio, q. This factor and the various trajectories of jet penetration height versus downstream distance were analyzed to generate empirical relations that predict the actual measured trajectories to within 23%. The two empirical equations were found to be,

$$\frac{y}{d_i} = 2.173 q^{0.276} \left(\frac{x}{d_i} \right)^{0.281} , \tag{4.4a}$$

and

$$\frac{y}{d_i} = q^{0.344} ln \left[4.704 \left(\frac{x}{d_i} + 0.6373 \right) \right] . \tag{4.4b}$$

Previous studies of the normal injection of a gas into a supersonic free stream have typically used values of q around unity. This study investigates injections with $5.9 < q < 38.6$. Despite the large extrapolation from previous works, some of the empirical equations generated by past researchers predict the trajectories measured to with 25%. Predictions from other empirical relations are shown to differ by up to 67%.

[8] As was discussed in the Background chapter, the PLIF technique for computing a temperature assumes a Boltzmann distribution among the ro-vibrational target ro-vibrational levels.

Temperatures were computed using the ratio of the fluorescence intensity measured from the excitation of two different ro-vibrational lines by assuming a Boltzmann distribution among the levels. The temperatures in the combustion region were found to range from 880 to 2600 K.

4.4 Suggestions

This study was limited by both the physical size of the test section and the low pressure limitations. The plasma tube can sustain a discharge in 2 atmospheres of argon, but the inclusion of oxygen into the plasma tube reduces the coupling efficiency of the RF power to the gas. The highest plasma tube pressure at which data was recorded was 200 torr, which results in an expansion/combustion chamber pressure of 55 torr at matched conditions. Future work should aim at correcting these difficulties, making the results more relevant to actual applications (for example, studies for a scramjet engine should be at higher pressures). A higher free stream pressure would also permit lower values of q to be established, and that would make comparisons to previous research more realistic, since most of those experiments deal with values of q below 7 (a typical scramjet engine would have values of q on the order of 1 or below). In the current experimental appuratus, hydrogen injection pressures low enough to study q values on the order of unity are overly influenced by the boundary layer thickness[9]. Higher free stream pressures would allow lower values of q to be achieved while maintaining a sufficiently high hydrogen injection pressure.

The main source of error in the jet penetration measurements was the drop in injection pressure over the length of the 0.5 sec hydrogen pulse. This problem could be overcome in one of two ways. The hydrogen bottle could be moved into closer proximity to the experimental apparatus, larger diameter feed lines could be used, and a higher pressure gas regulator could be incorporated. Or better image capturing equipment that could provide a more precise timing scheme would allow the pulse width to be greatly reduced (and hence reduce the amount of pressure drop during the duration of the pulse). By precisely controlling the time lapse between the initiation of the hydrogen pulse and the capture of an image, improved image capturing equipment would allow the study of the time-evolution of the injection process.

The problem of defining the jet penetration edge was also mentioned. A higher pressure free stream would increase the gas density in the combustion region, perhaps making the edge of the jet more clear in the images. Quantitative measurements of OH concentrations would also be very useful for future combustion studies and CFD code benchmarking.

[9] Jet observed at these conditions are noted to never penetrate past the boundary layer.

Figure 4-1: Typical Chemiluminescence Image

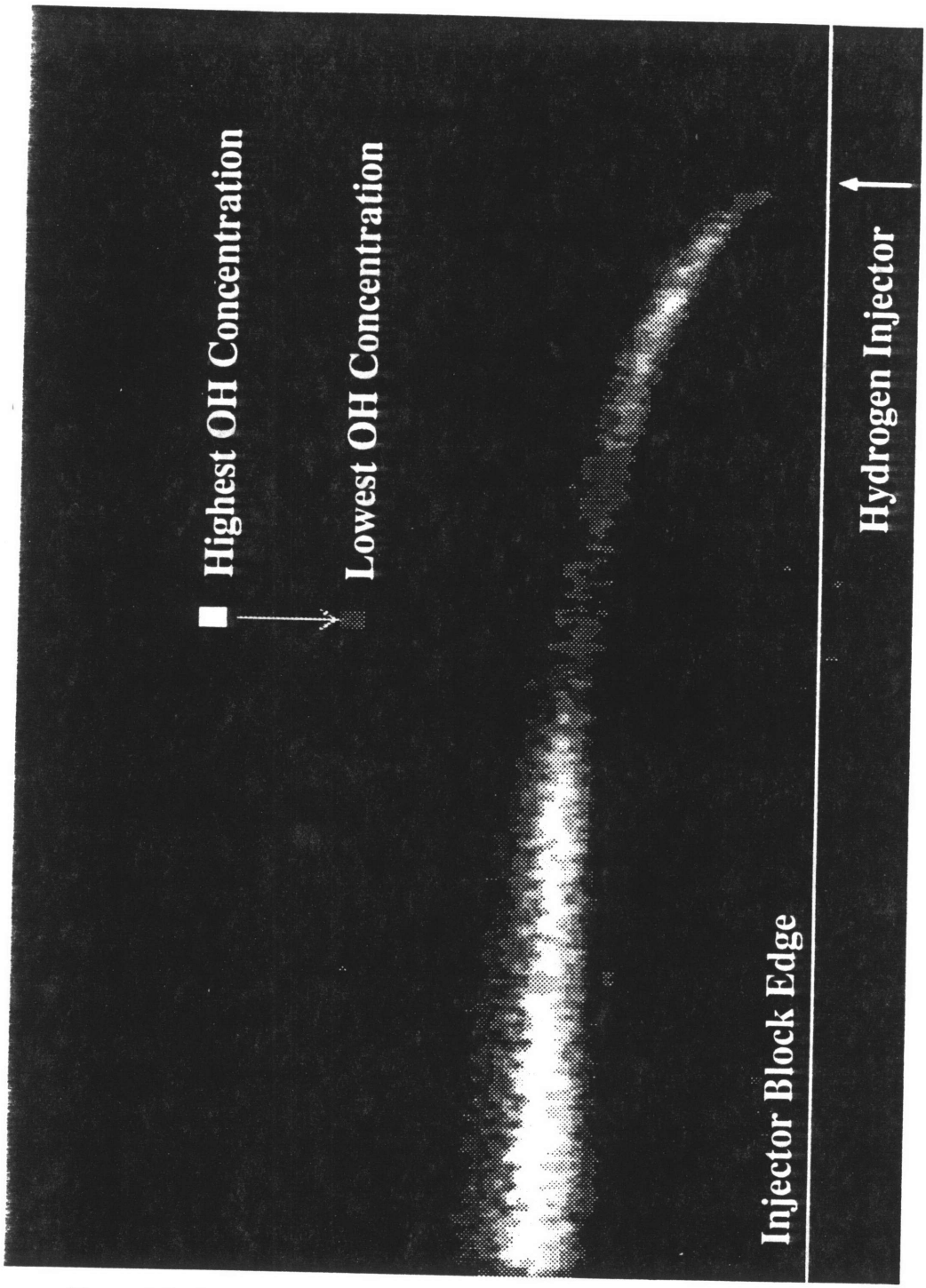

Figure 4-2: Averaged, Smoothed, Contrast-Enhanced PLIF Image, $q = 13$

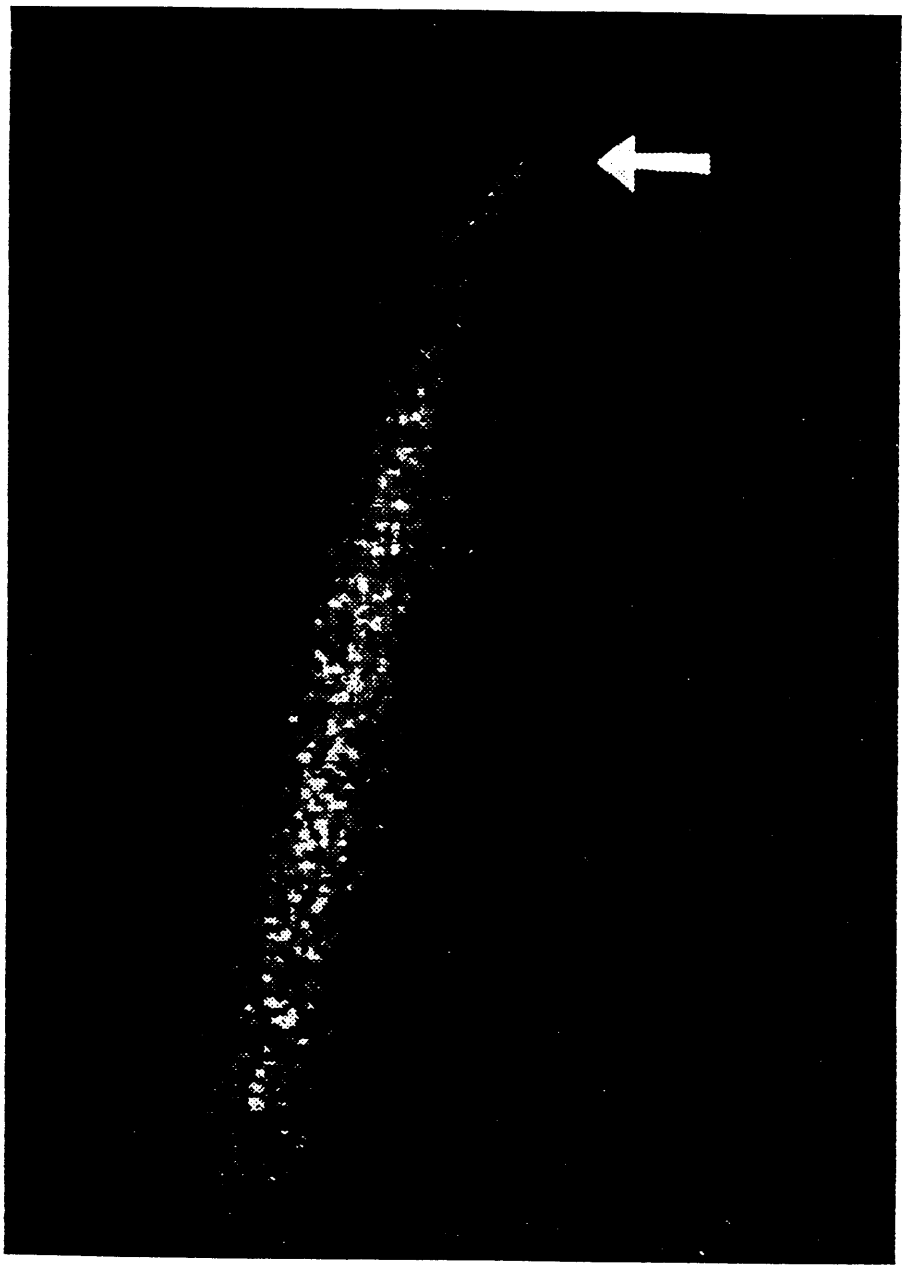

Figure 4-3: Single-Shot, Unprocessed PLIF Image, $q = 13$

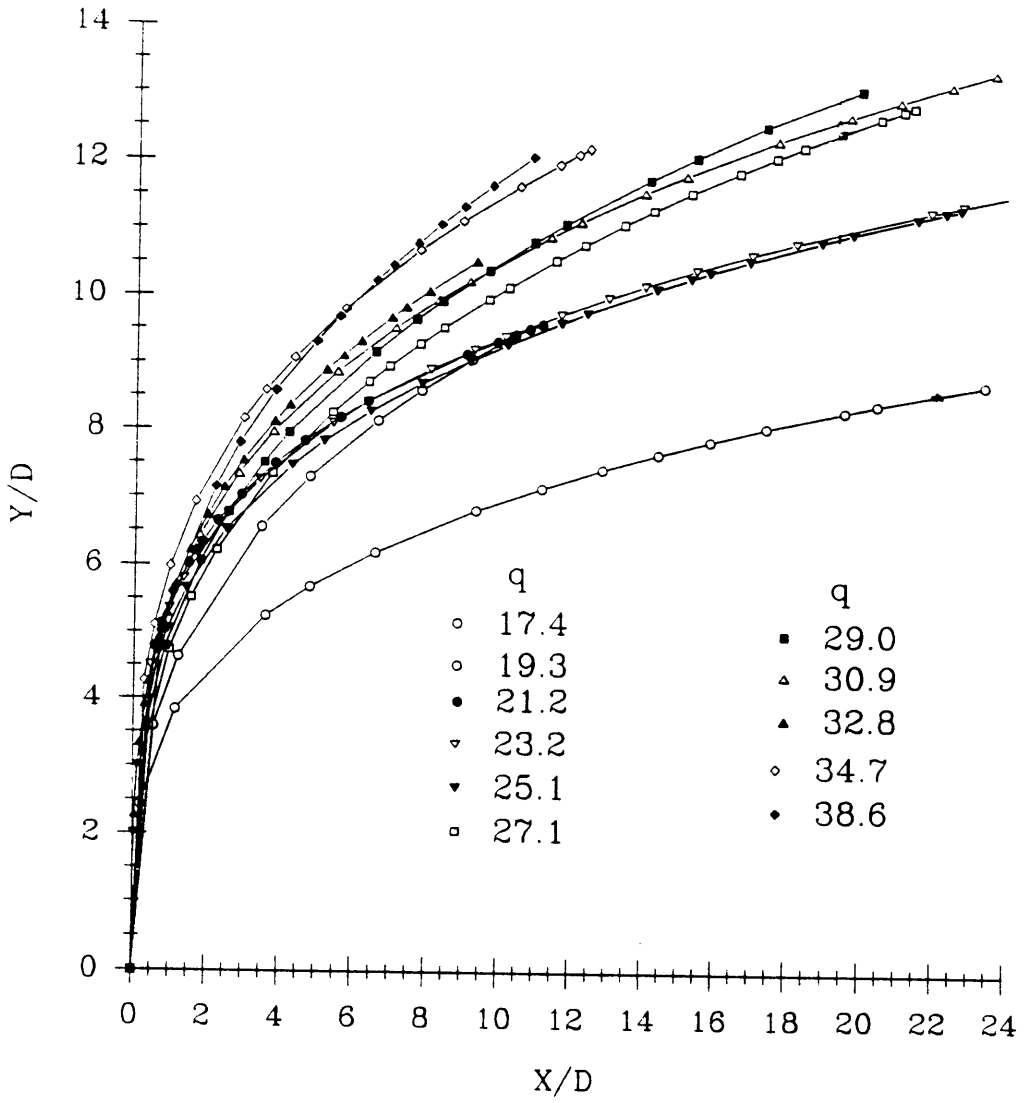

Figure 4-4: Jet Trajectories for a Free Stream Pressure of 12 torr, ±3%

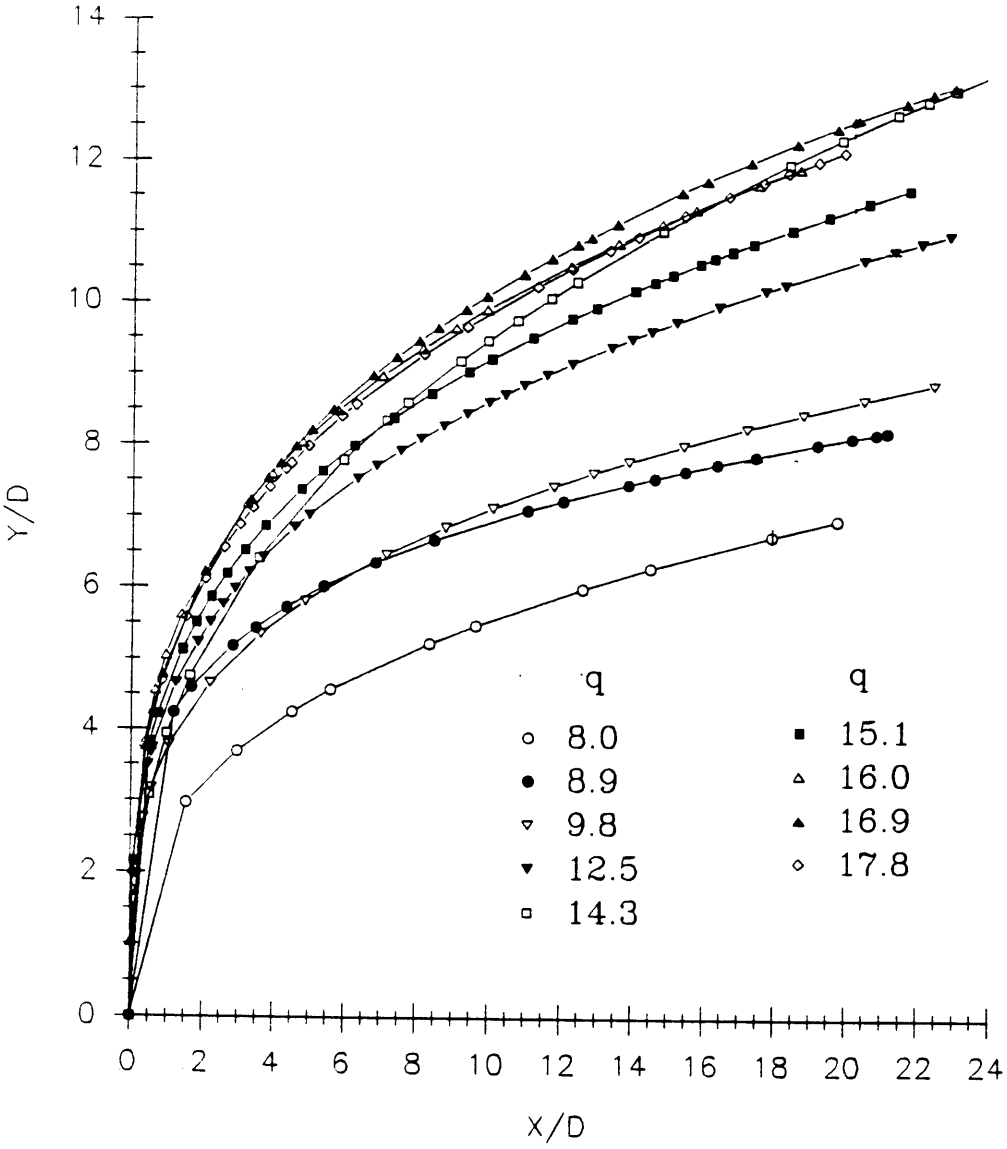

Figure 4-5: Jet Trajectories for a Free Stream Pressure of 26 torr, ±3%

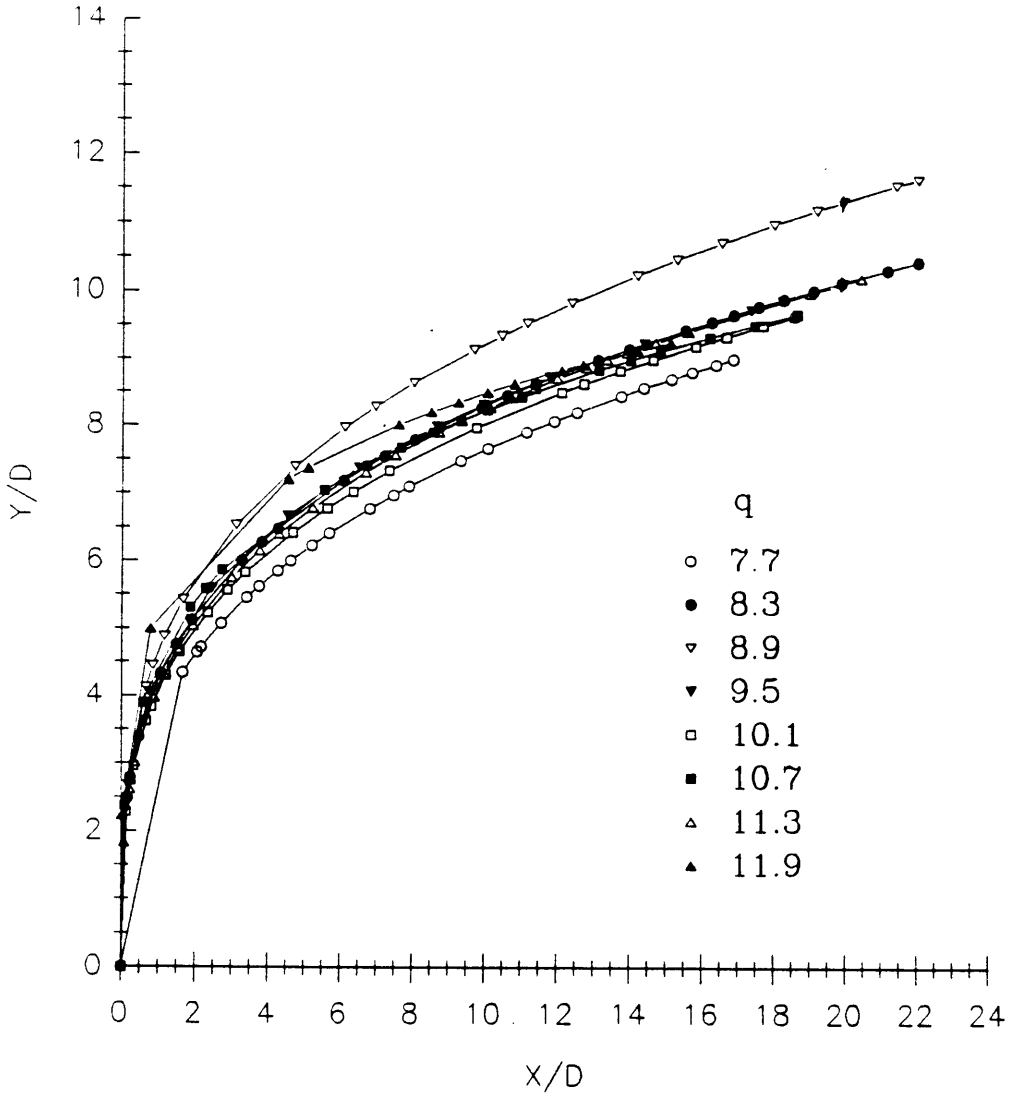

Figure 4-6: Jet Trajectories for a Free Stream Pressure of 39 torr, ±3%

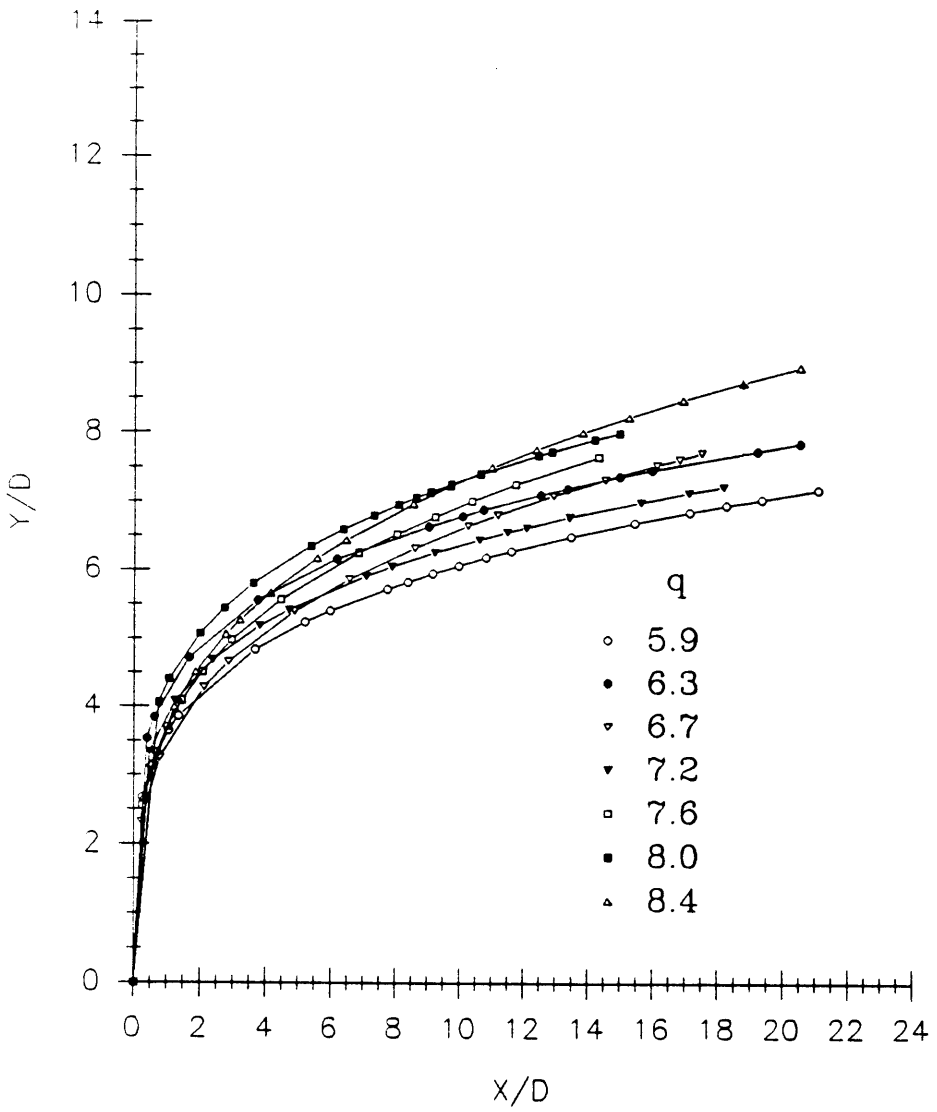

Figure 4-7: Jet Trajectories for a Free Stream Pressure of 55 torr, ±3%

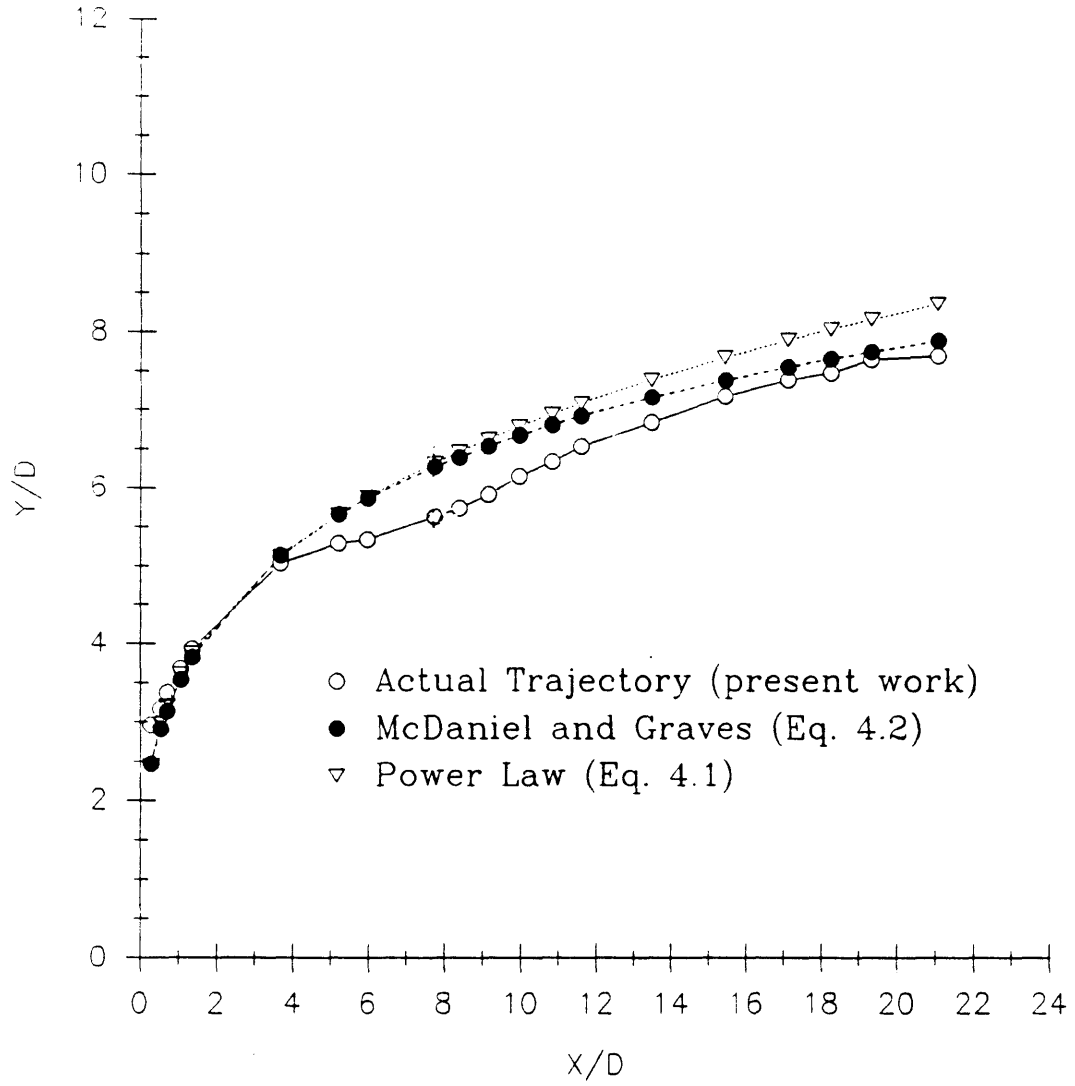

Figure 4-8: Actual Jet Penetration Trajectory Compared With Predicted Trajectories Calculated Using Equation 4.2 and Equation 4.1, for $q = 5.9$. Measured Trajectories ±3%, Predicted Trajectories ±2%

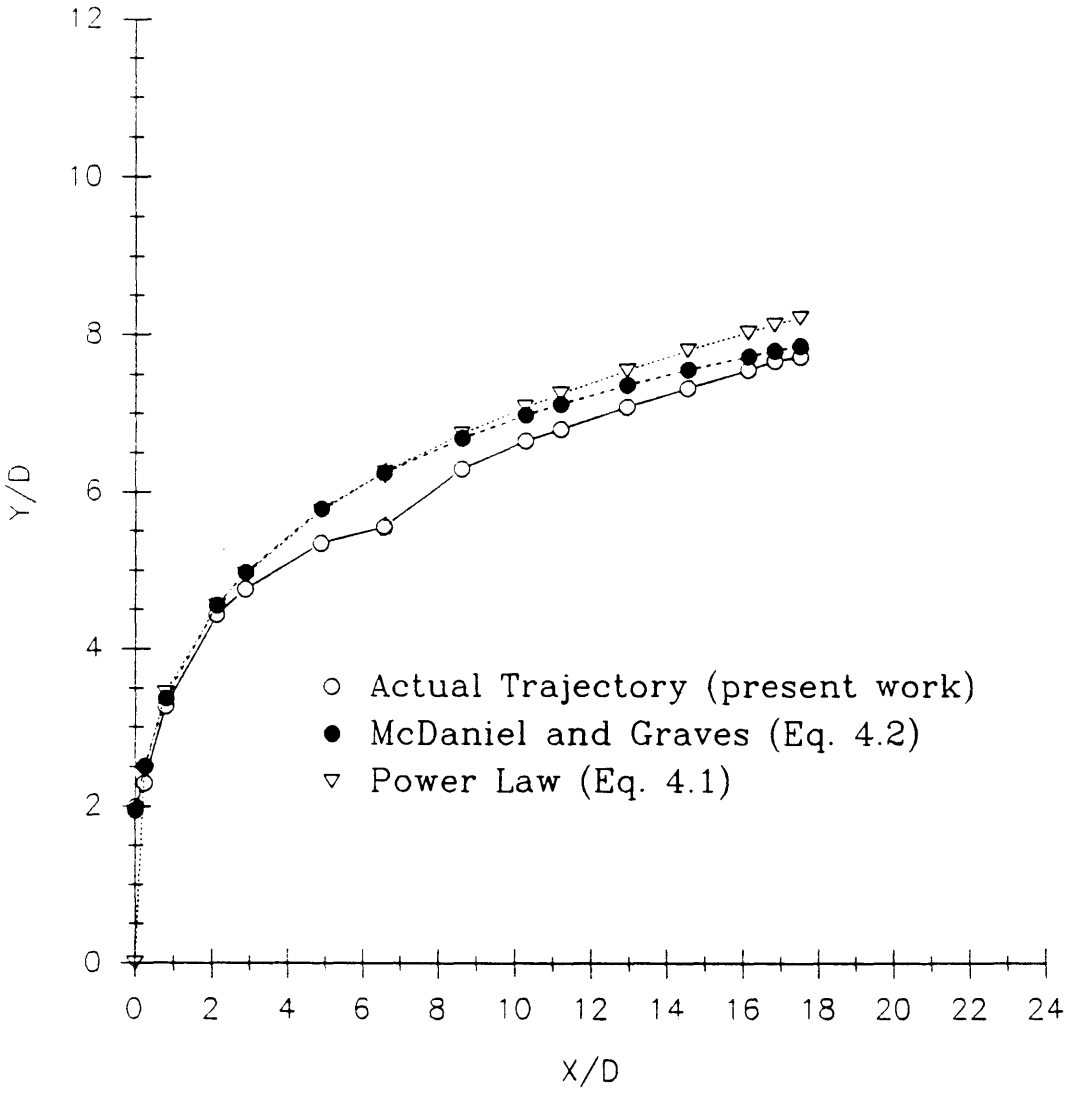

Figure 4-8 (continued), $q = 6.7$

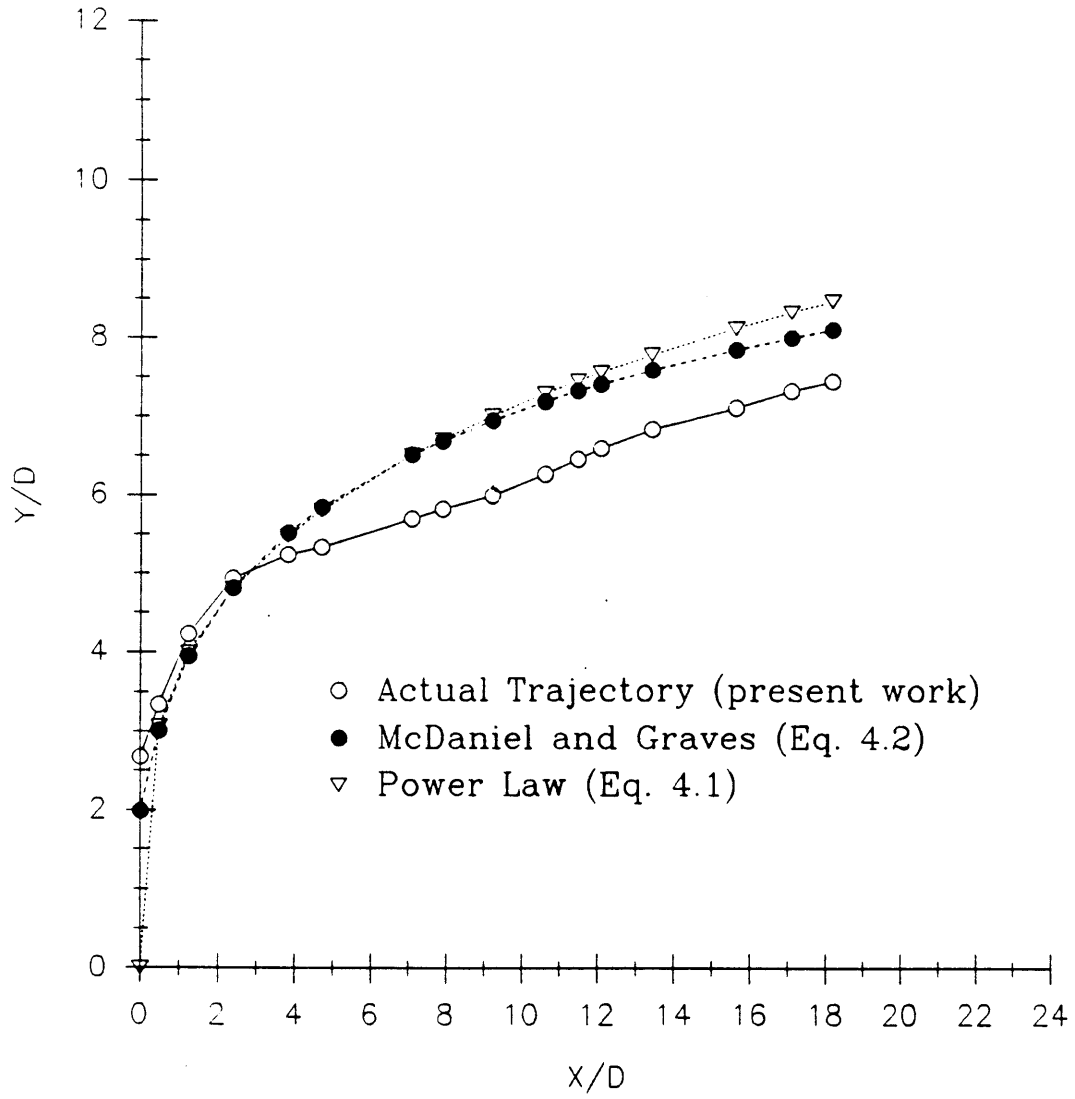

Figure 4-8 (continued), $q = 7.2$

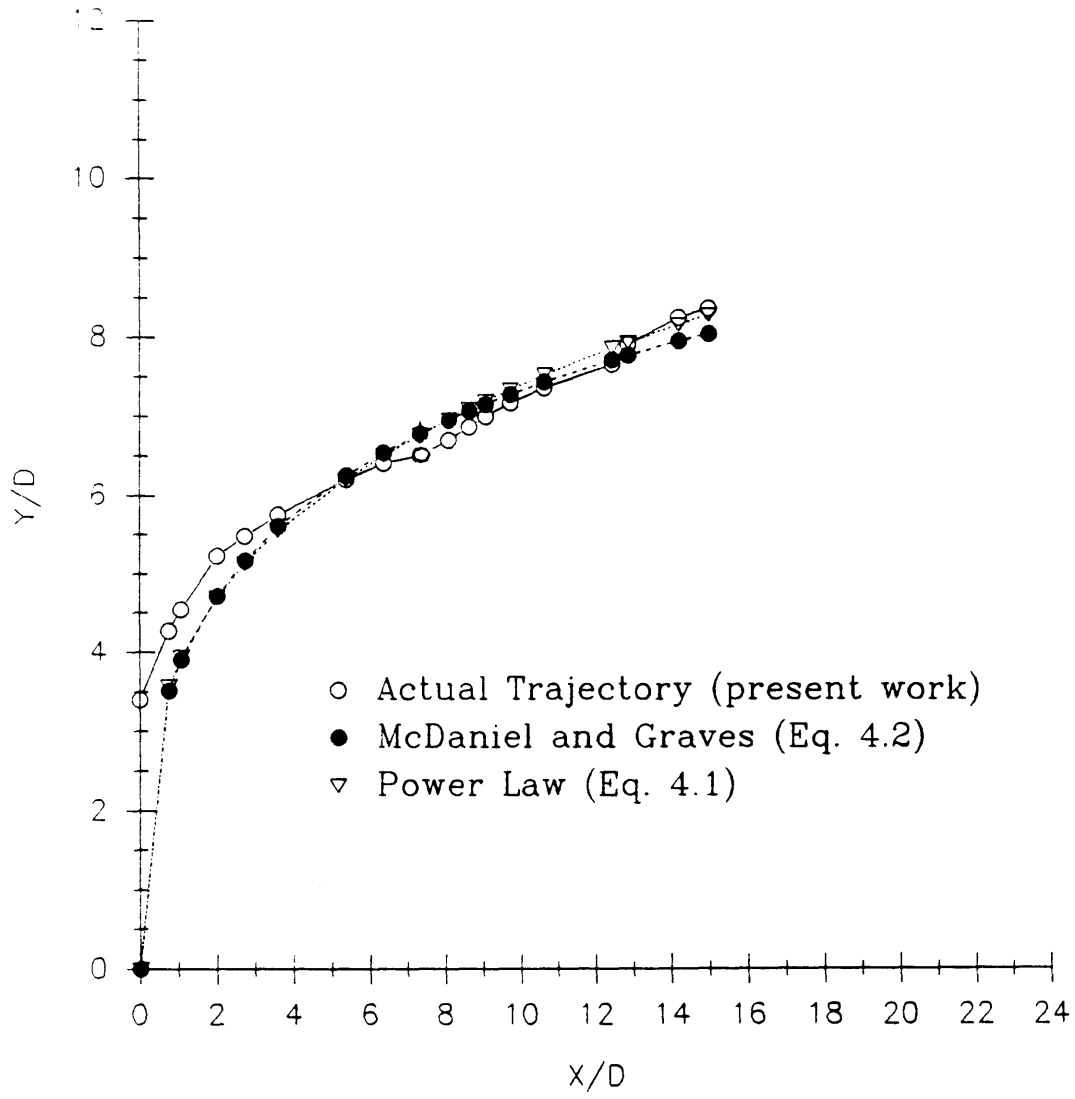

Figure 4-8 (continued), $q = 8.0$

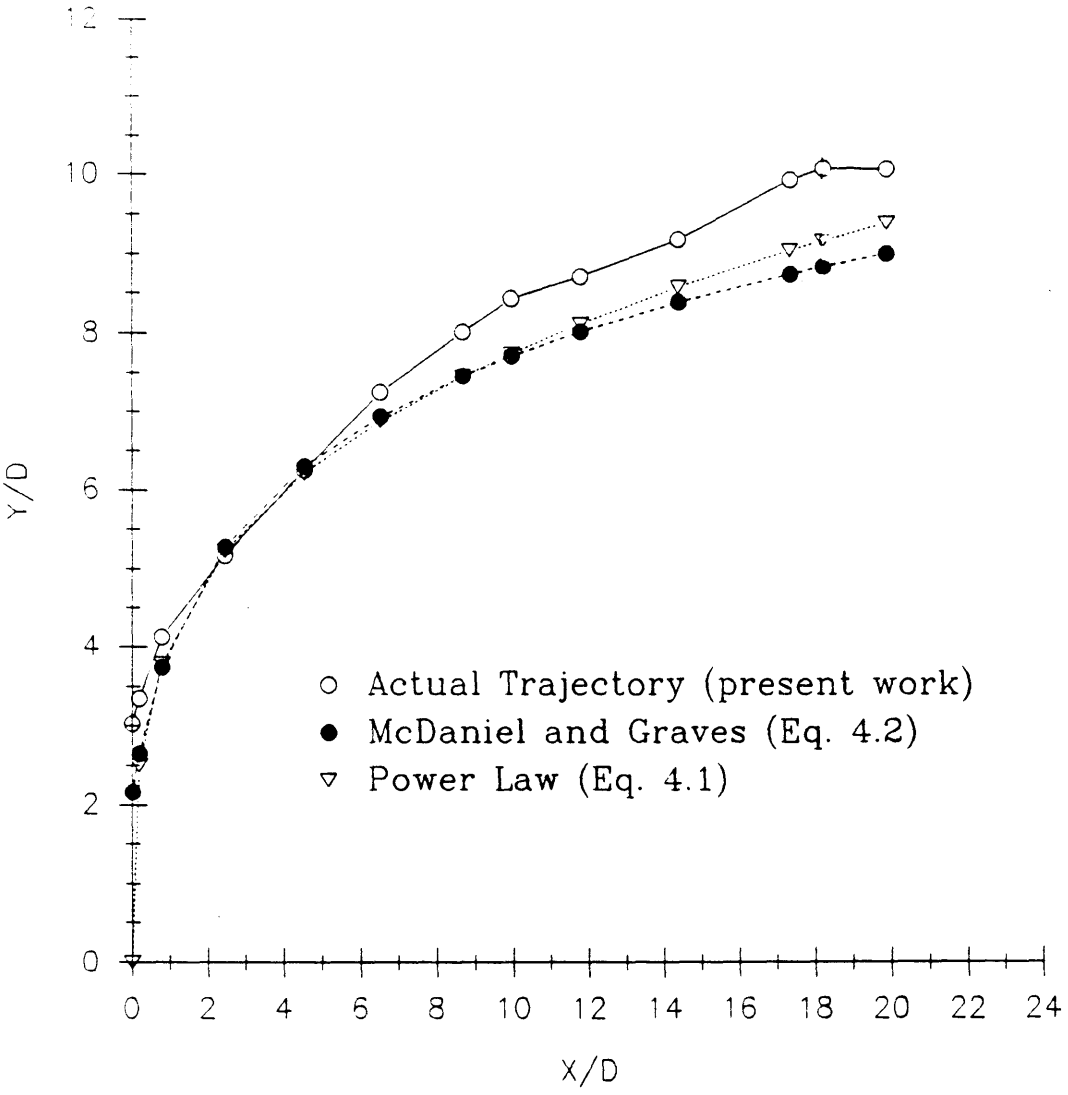

Figure 4-8 (continued), $q = 9.5$

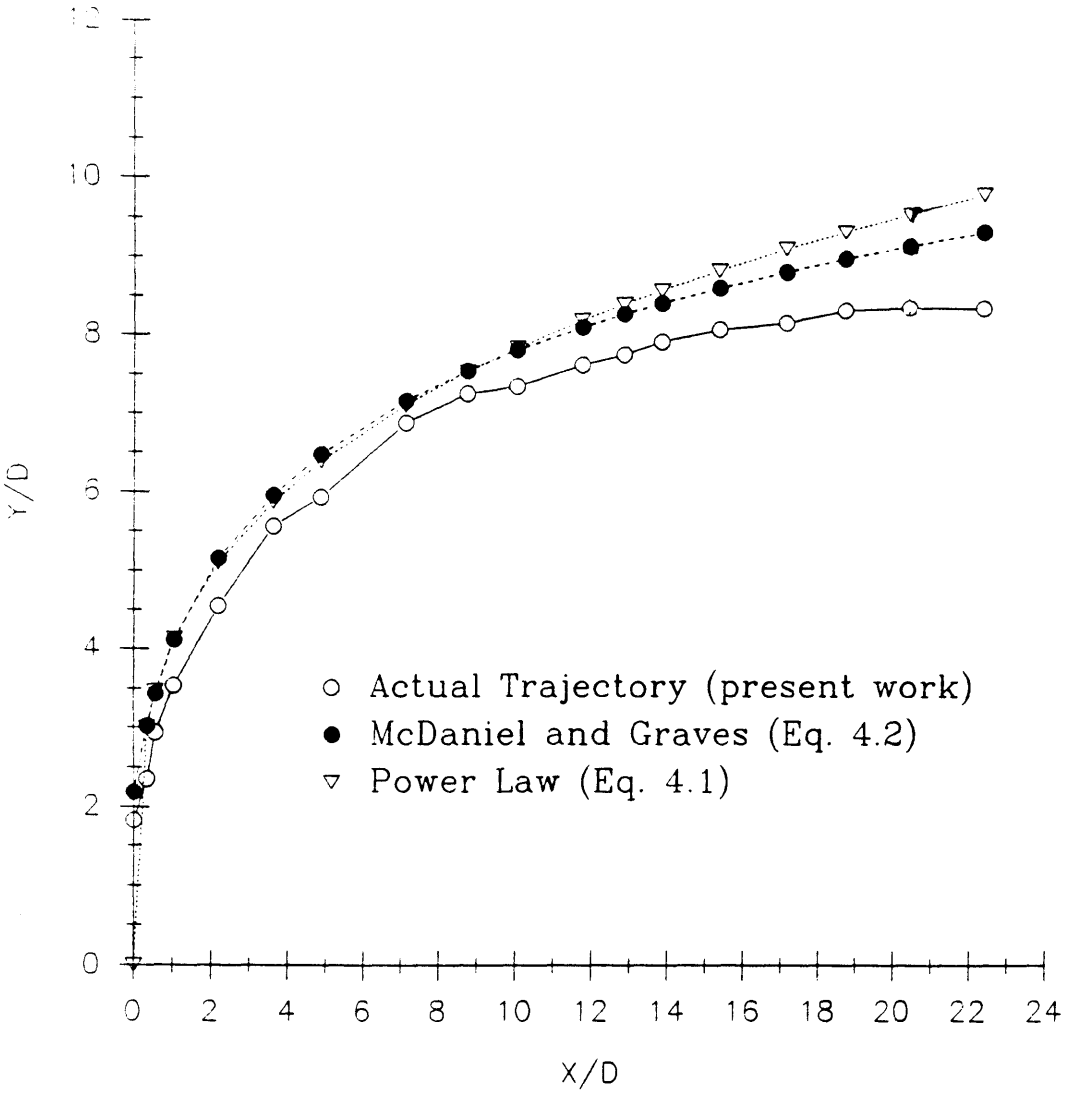

Figure 4-8 (continued), q = 9.8

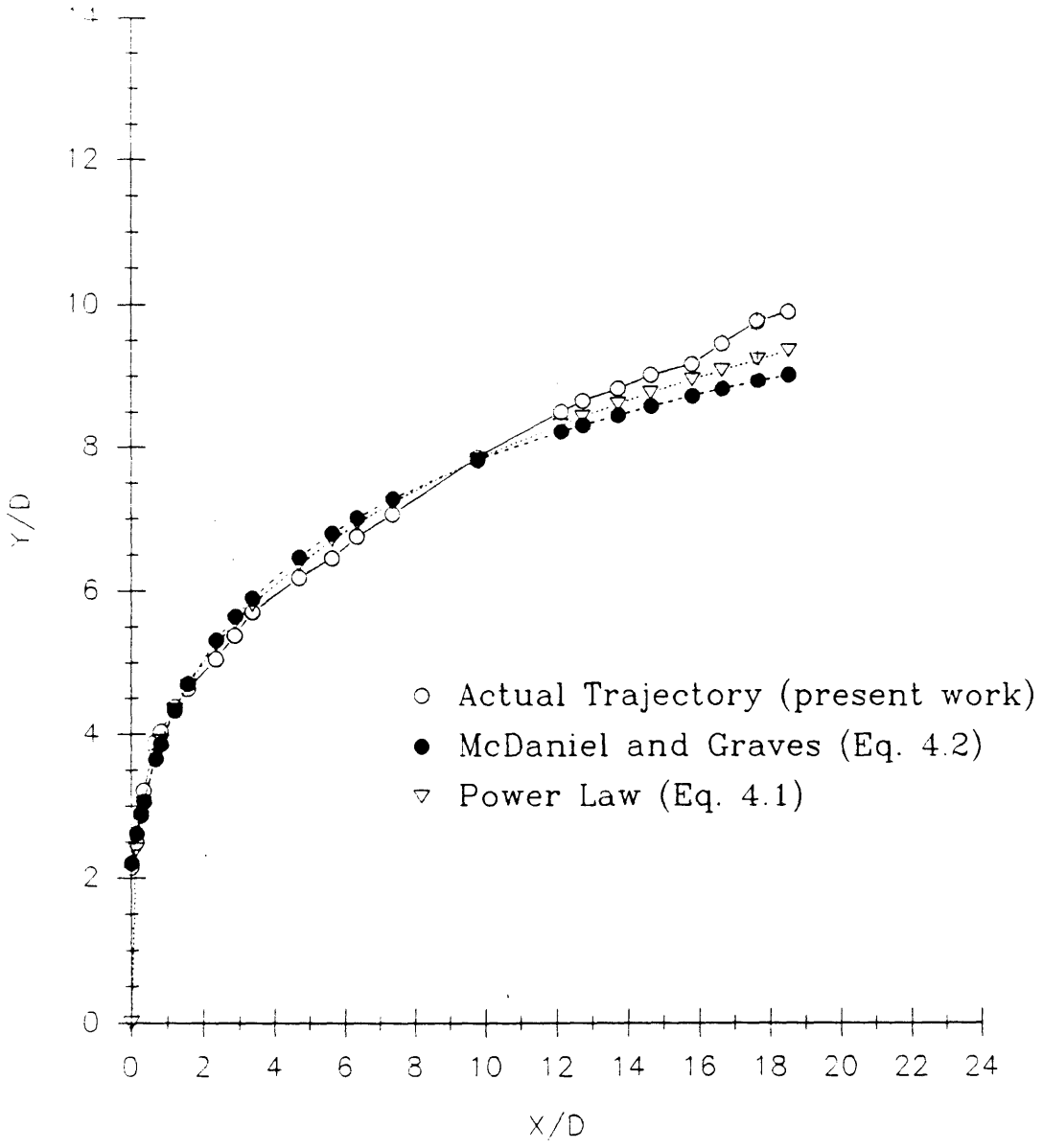

Figure 4-8 (continued), q = 10.1

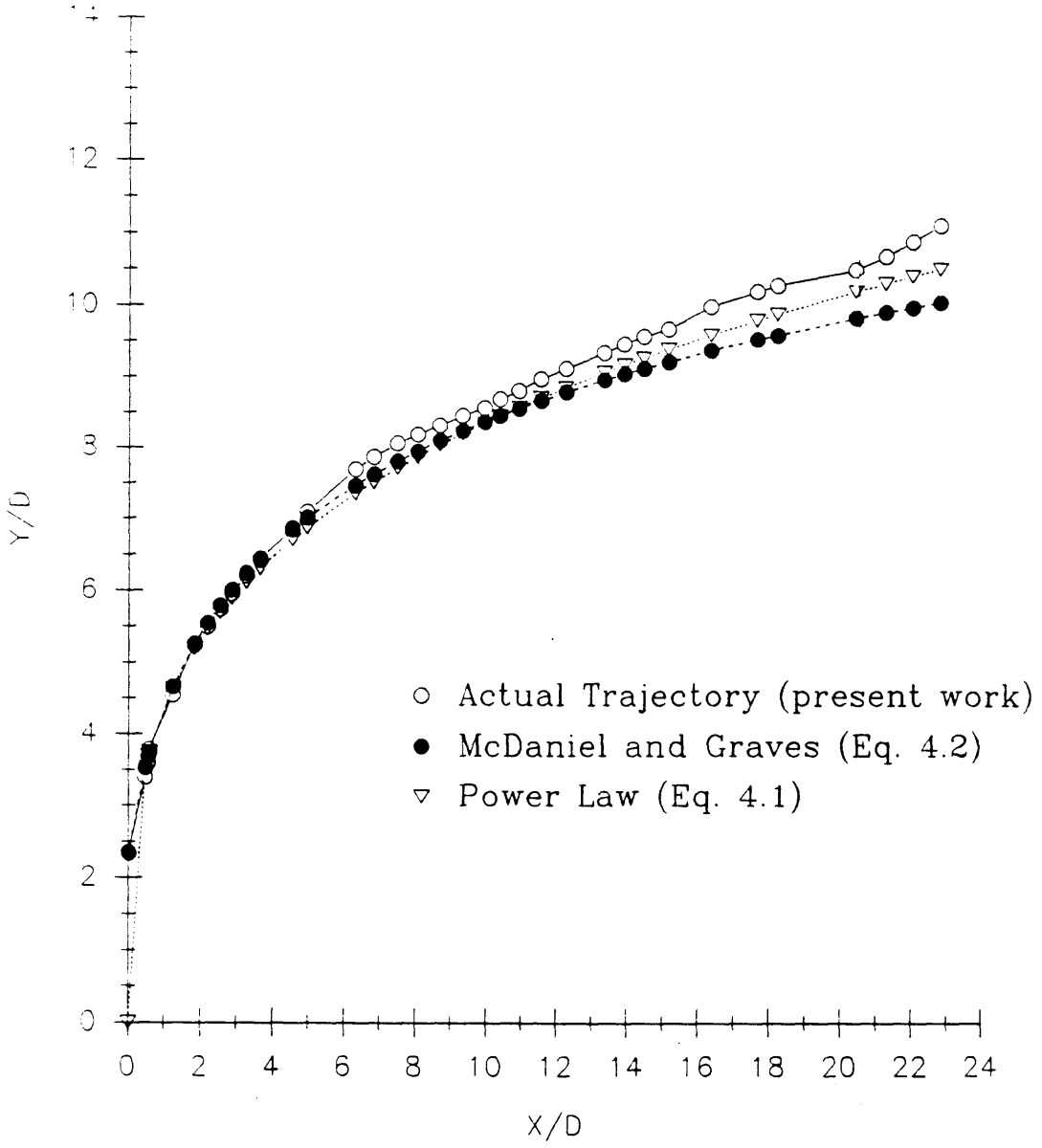

Figure 4-8 (continued), $q = 12.5$

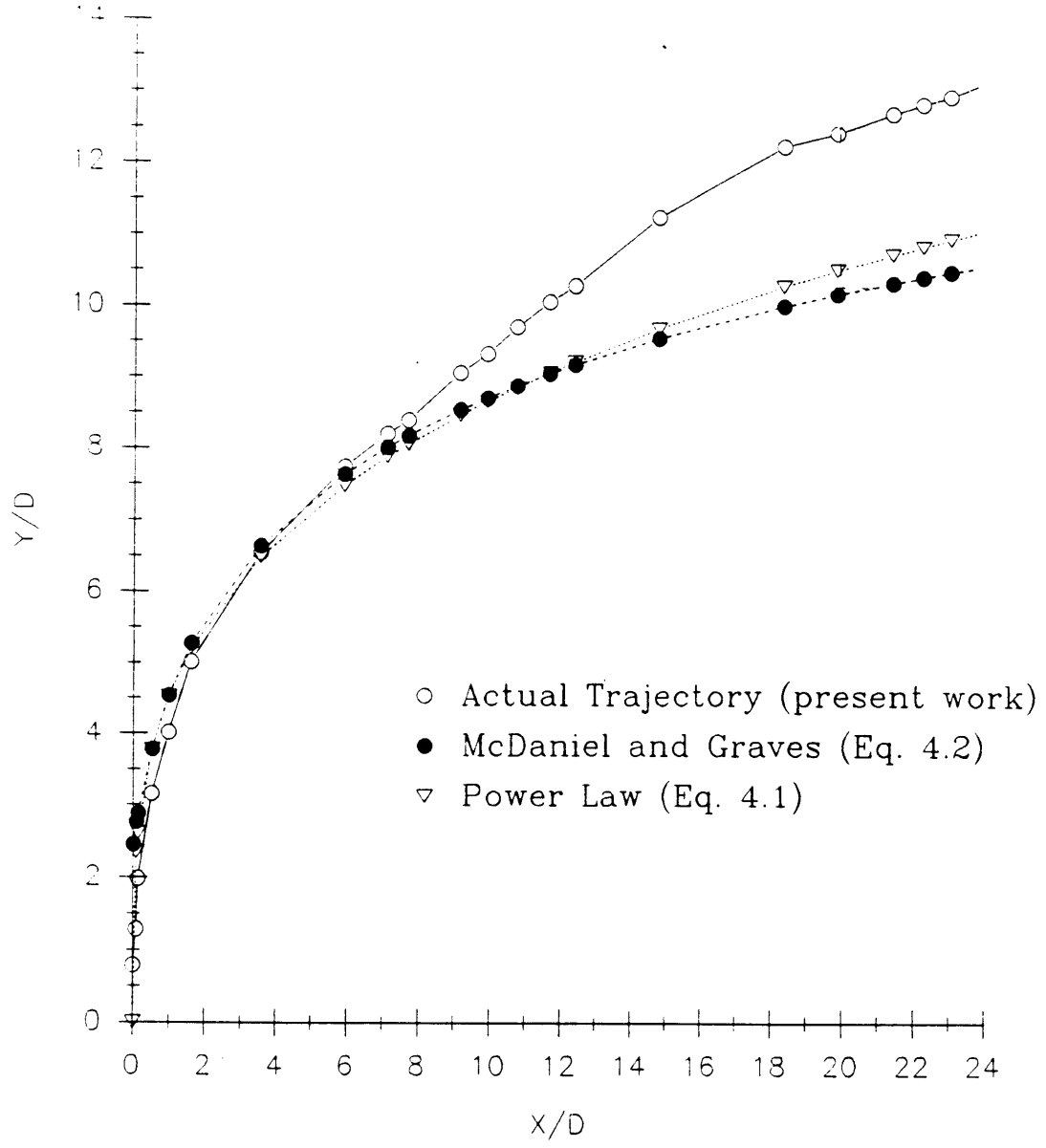

Figure 4-8 (continued), q = 14.3

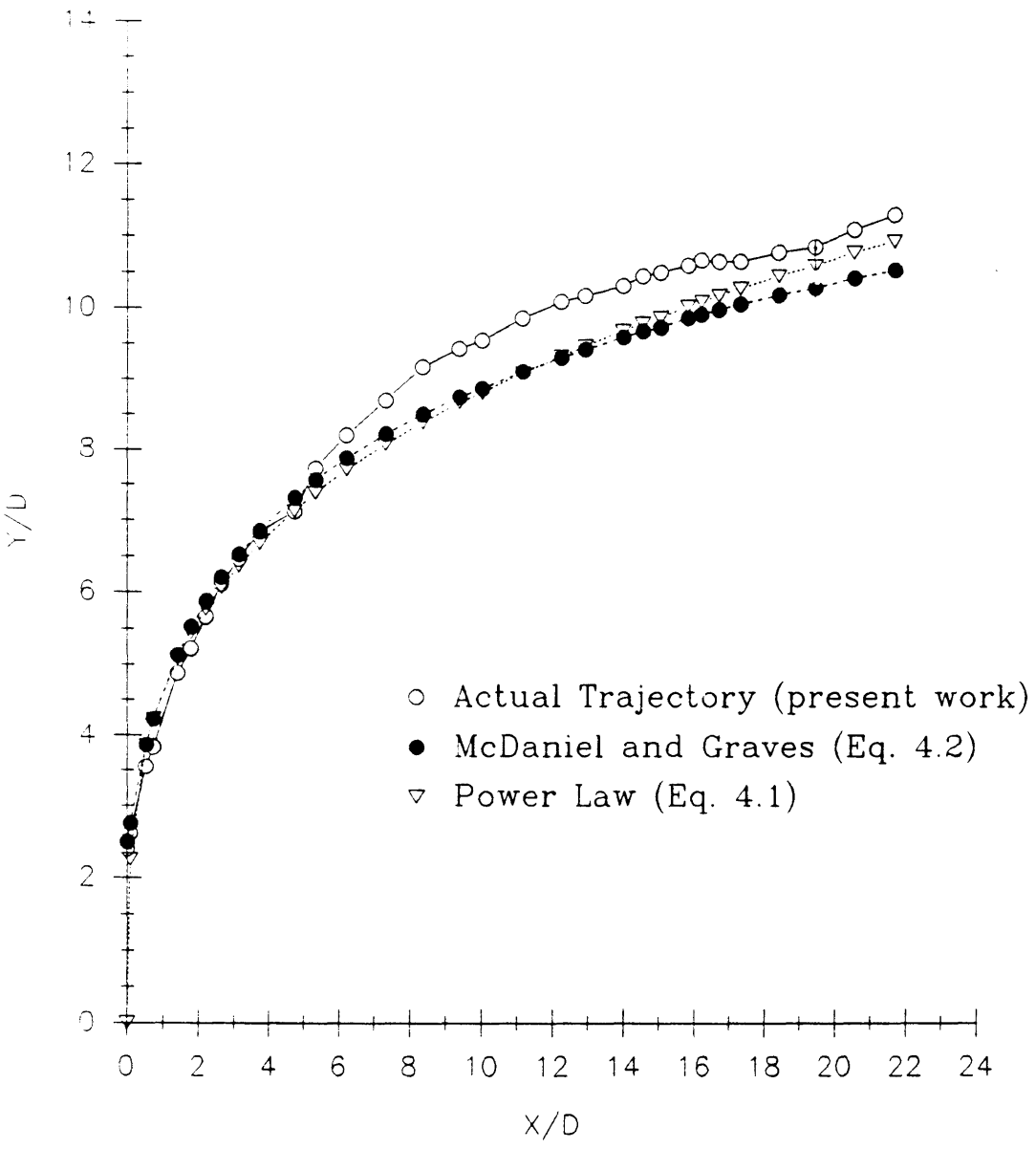

Figure 4-8 (continued), q = 15.1

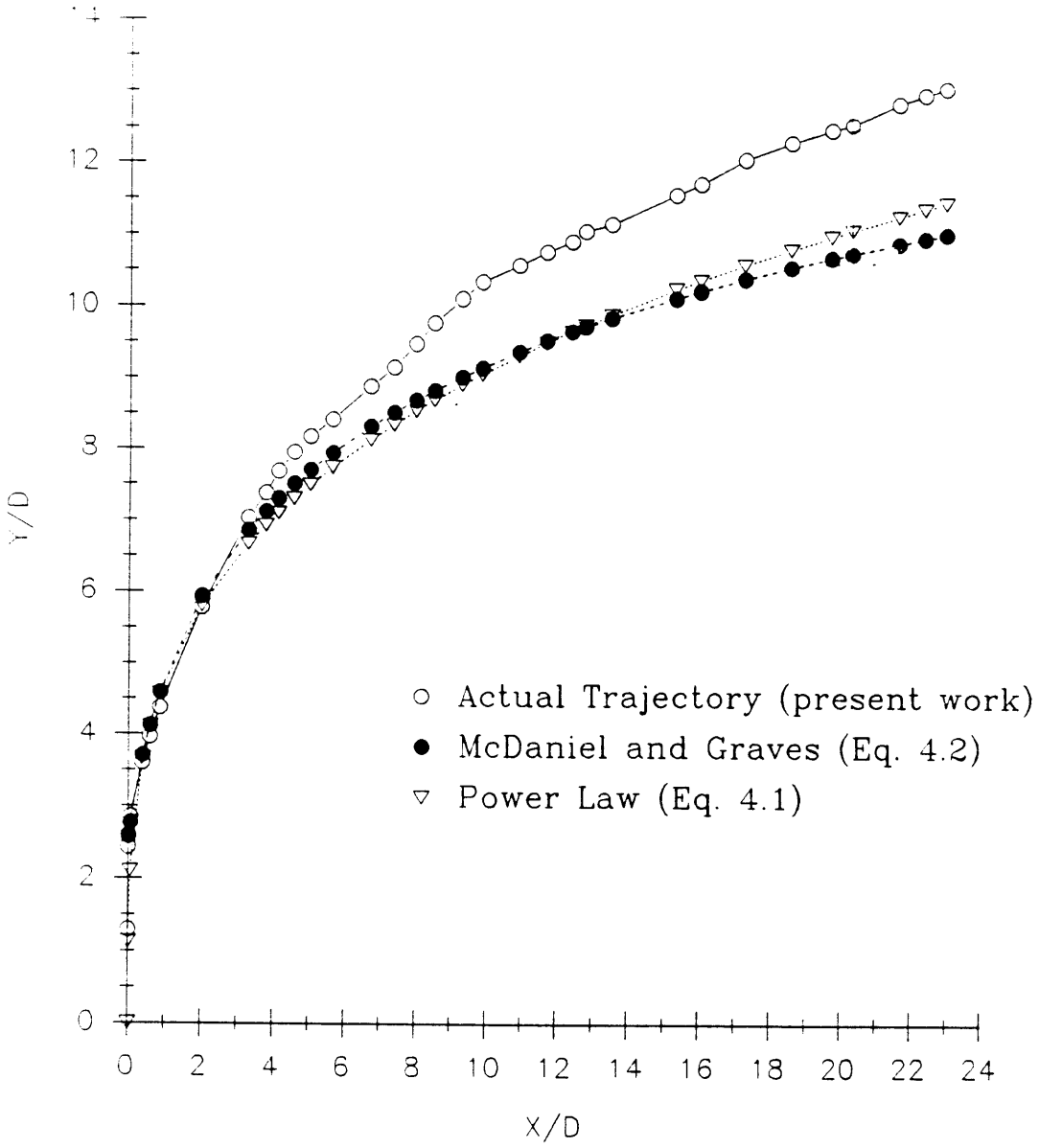

Figure 4-8 (continued), q = 16.9

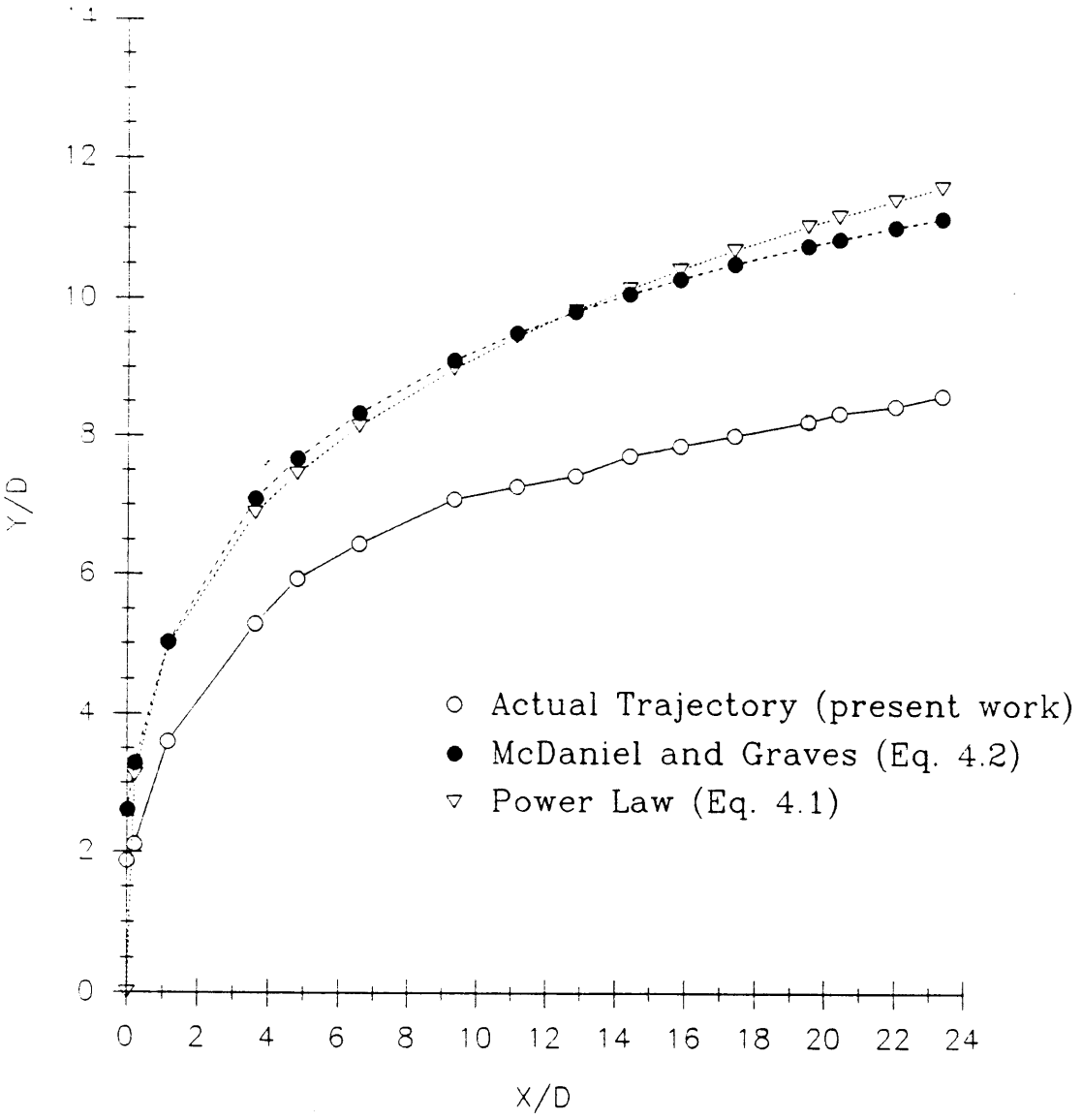

Figure 4-8 (continued), q = 17.4

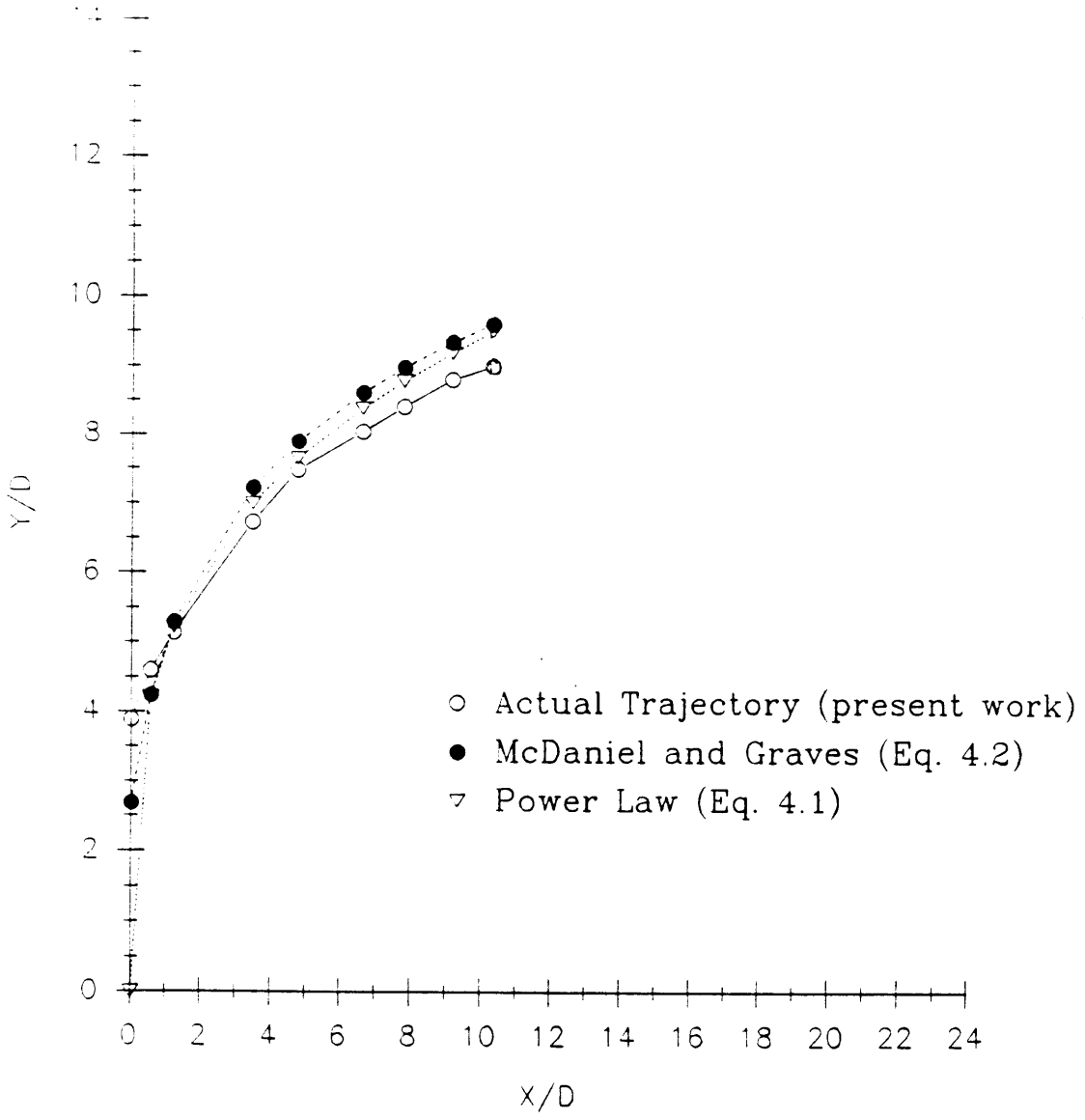

Figure 4-8 (continued), q = 19.3

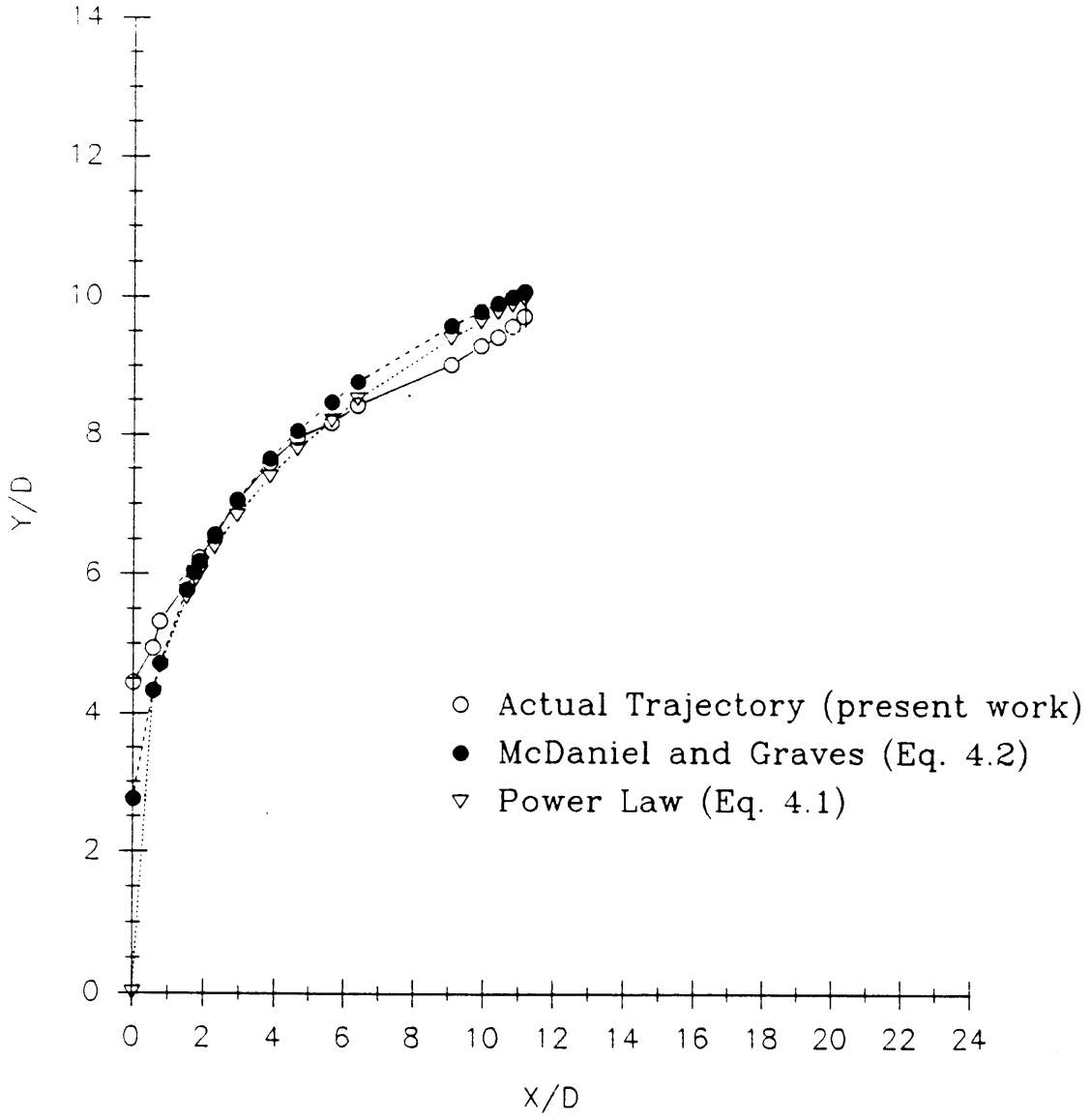

Figure 4-8 (continued), $q = 21.2$

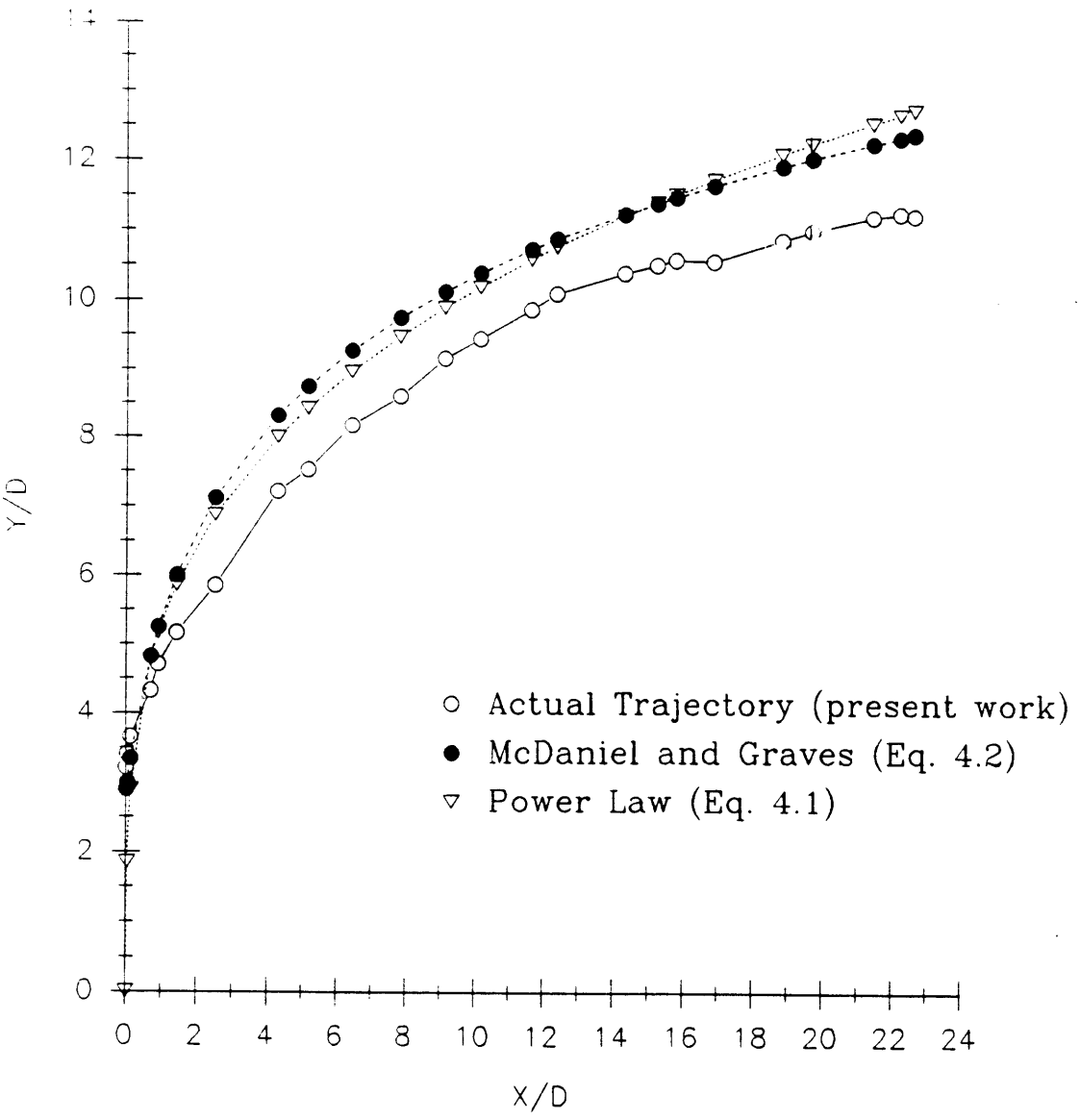

Figure 4-8 (continued), $q = 25.1$

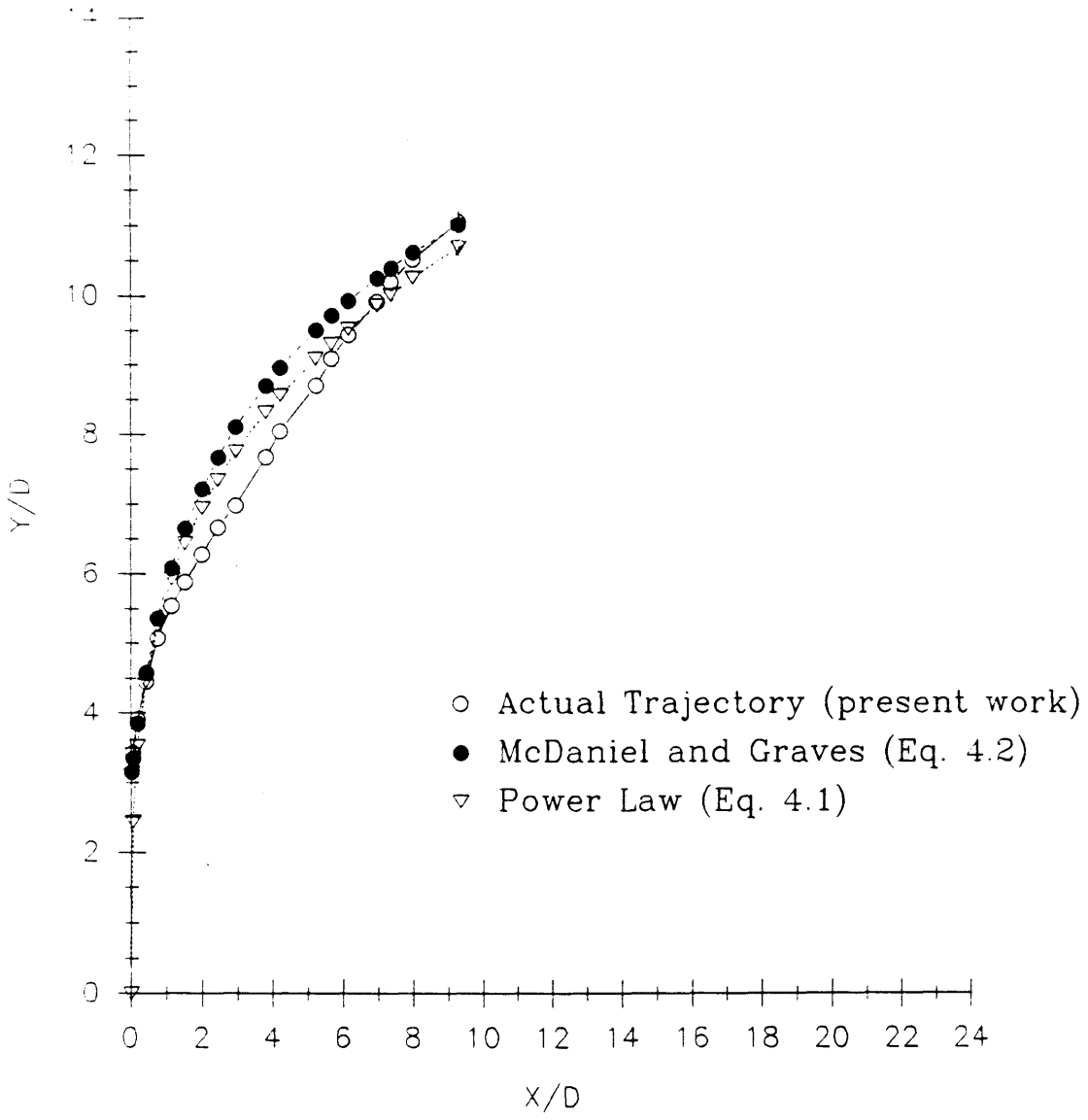

Figure 4-8 (continued), $q = 32.8$

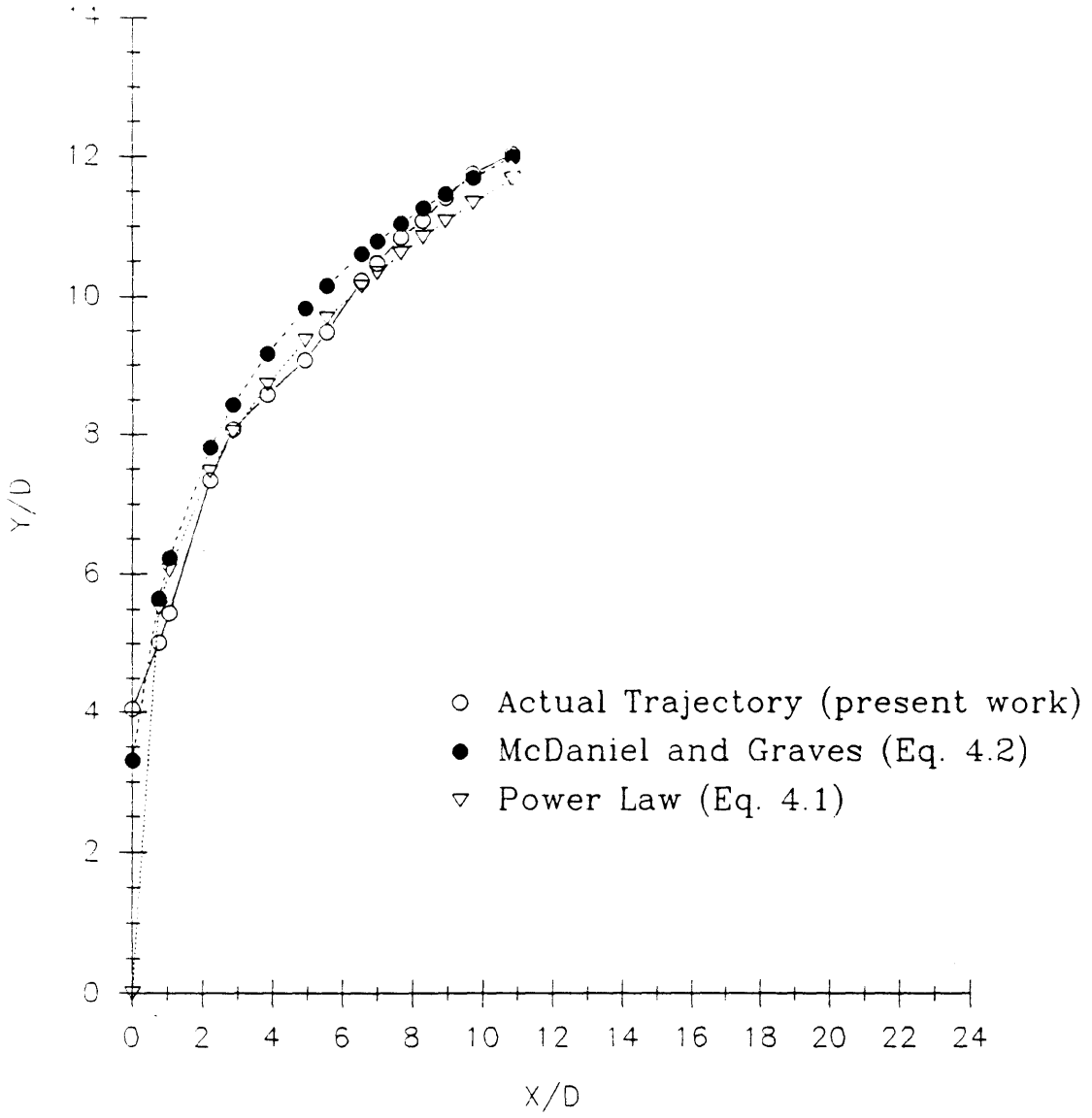

Figure 4-8 (continued), q = 38.6

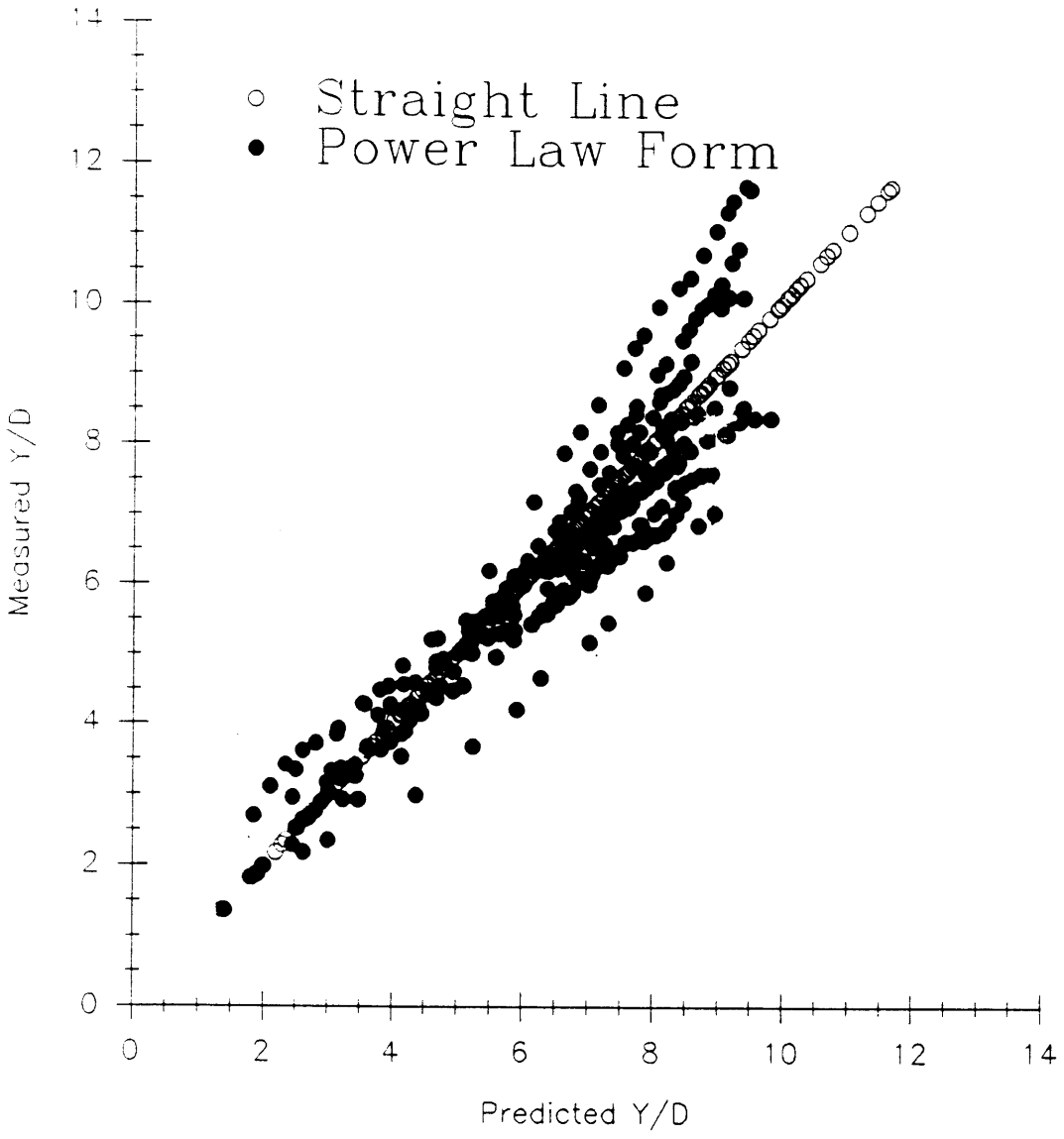

Figure 4-9: Empirical Predictions Compared to Measured Jet Trajectories, Equation 4.2 q >17, ±3%

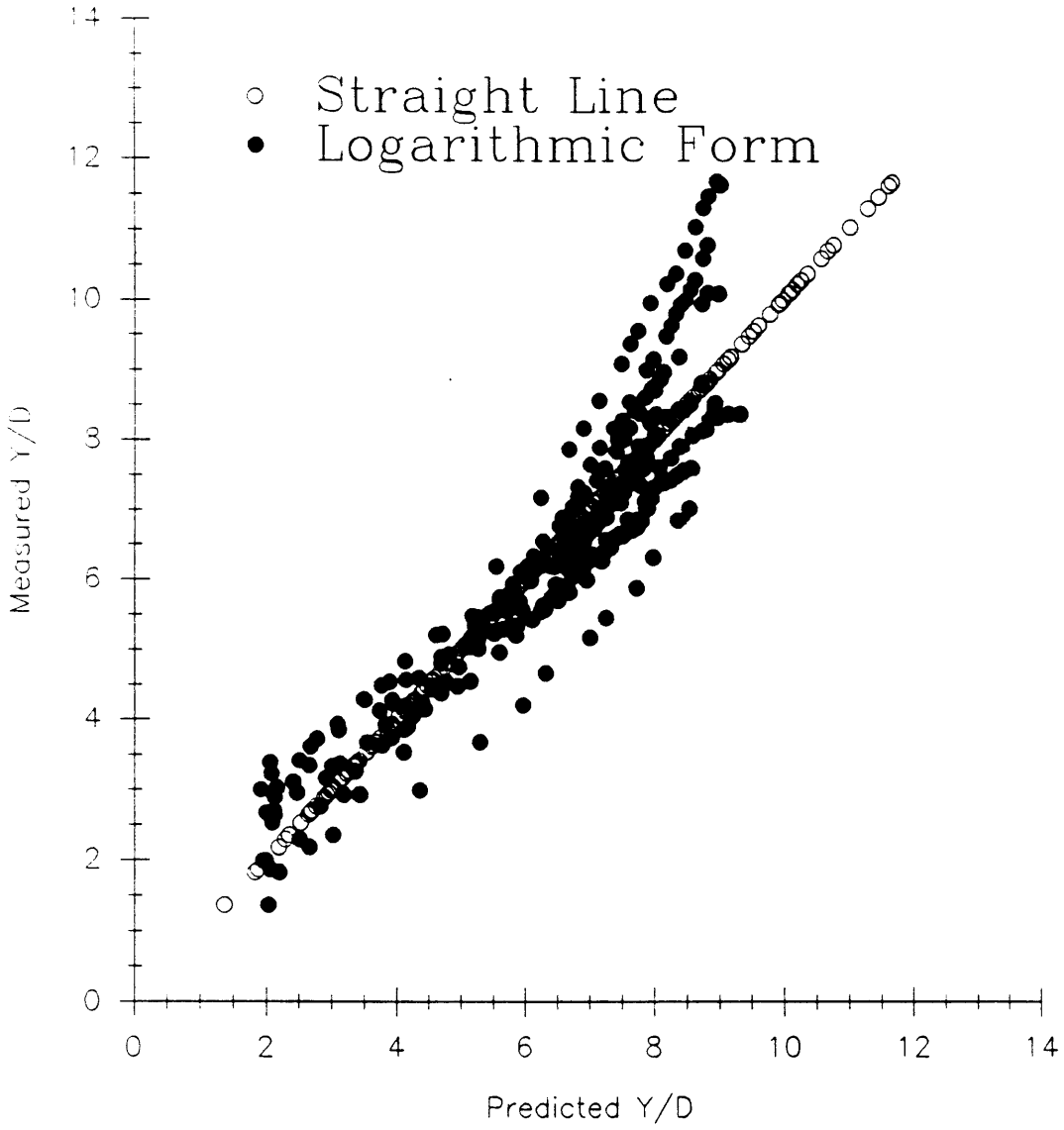

Figure 4-9 (continued), **Equation** 4.1, $q > 17$

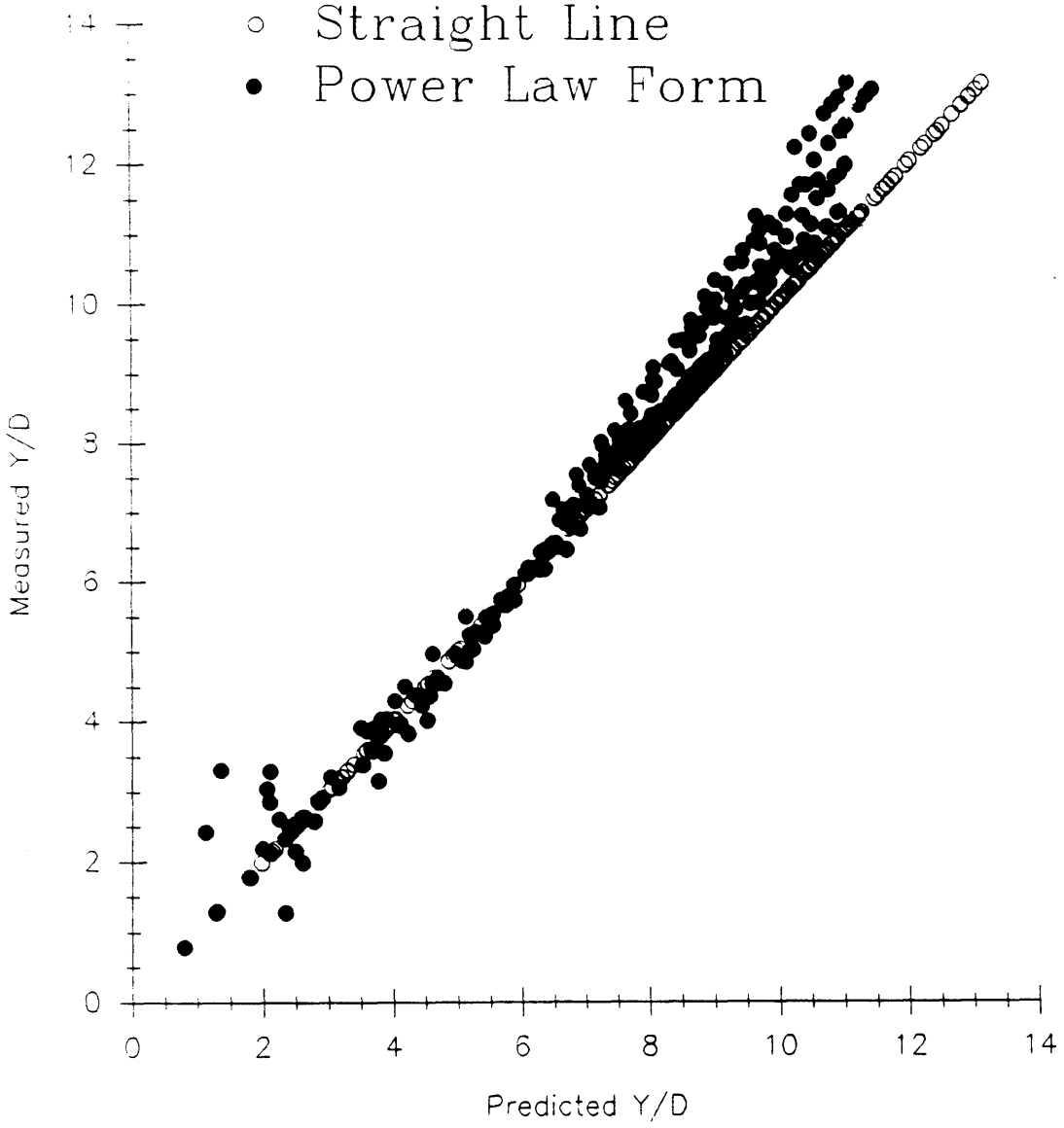

Figure 4-9 (continued), Equation 4.2, $10 < q < 17$

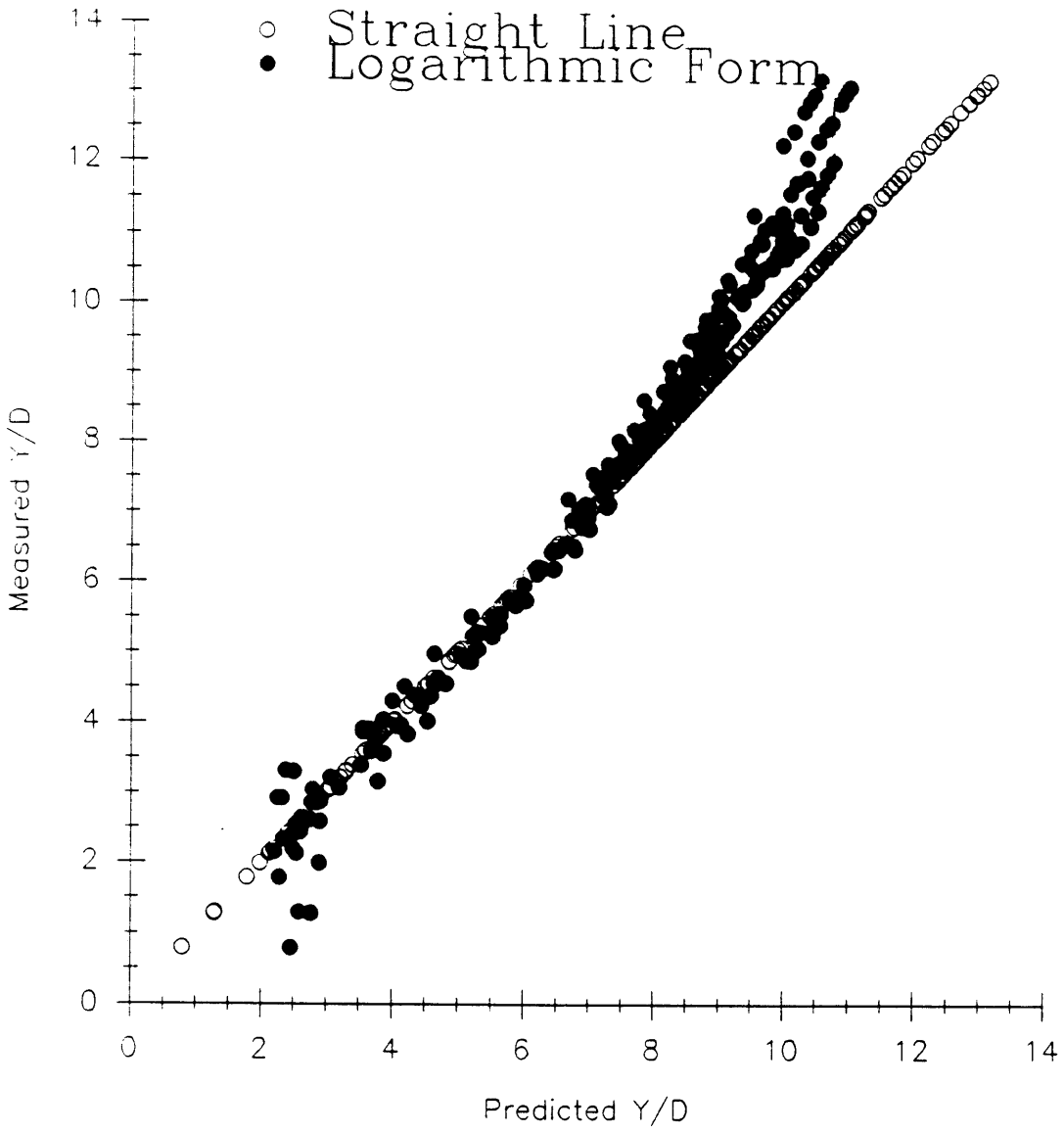

Figure 4-9 (continued), Equation 4.1, $10 < q < 17$

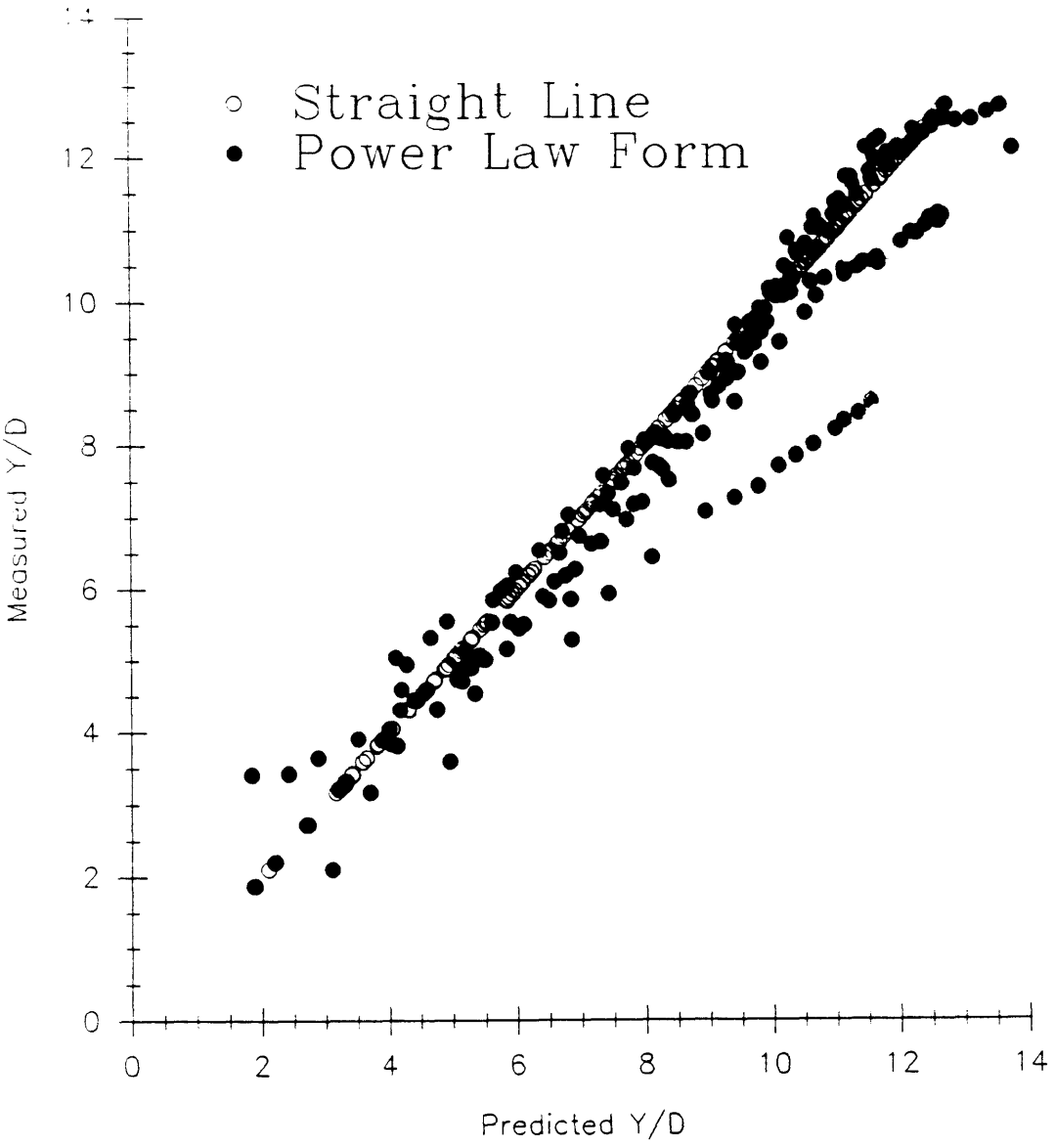

Figure 4-9 (continued), Equation 4.2, $10 < q$

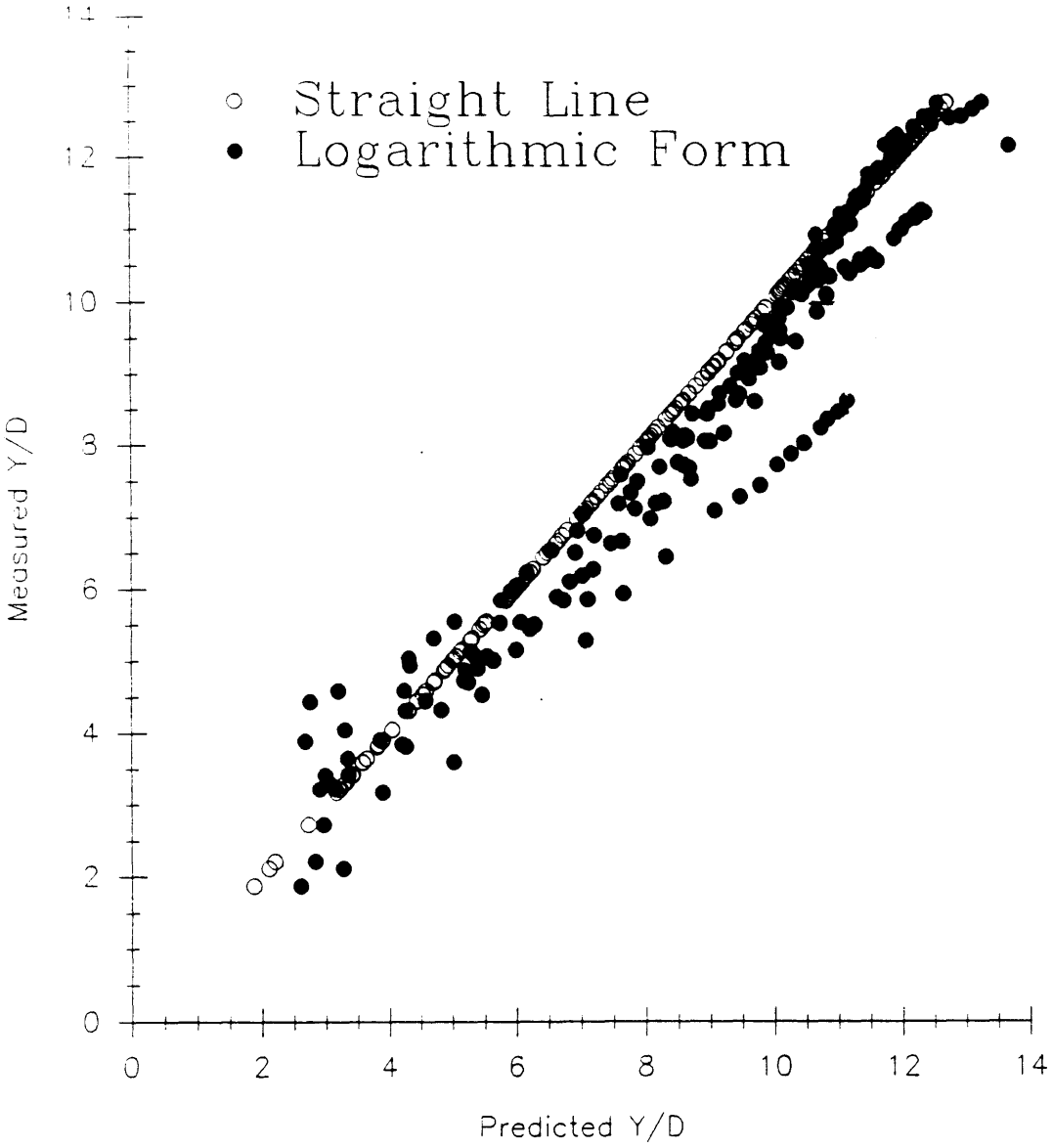

Figure 4-9 (continued), Equation 4.1, $10 < q$

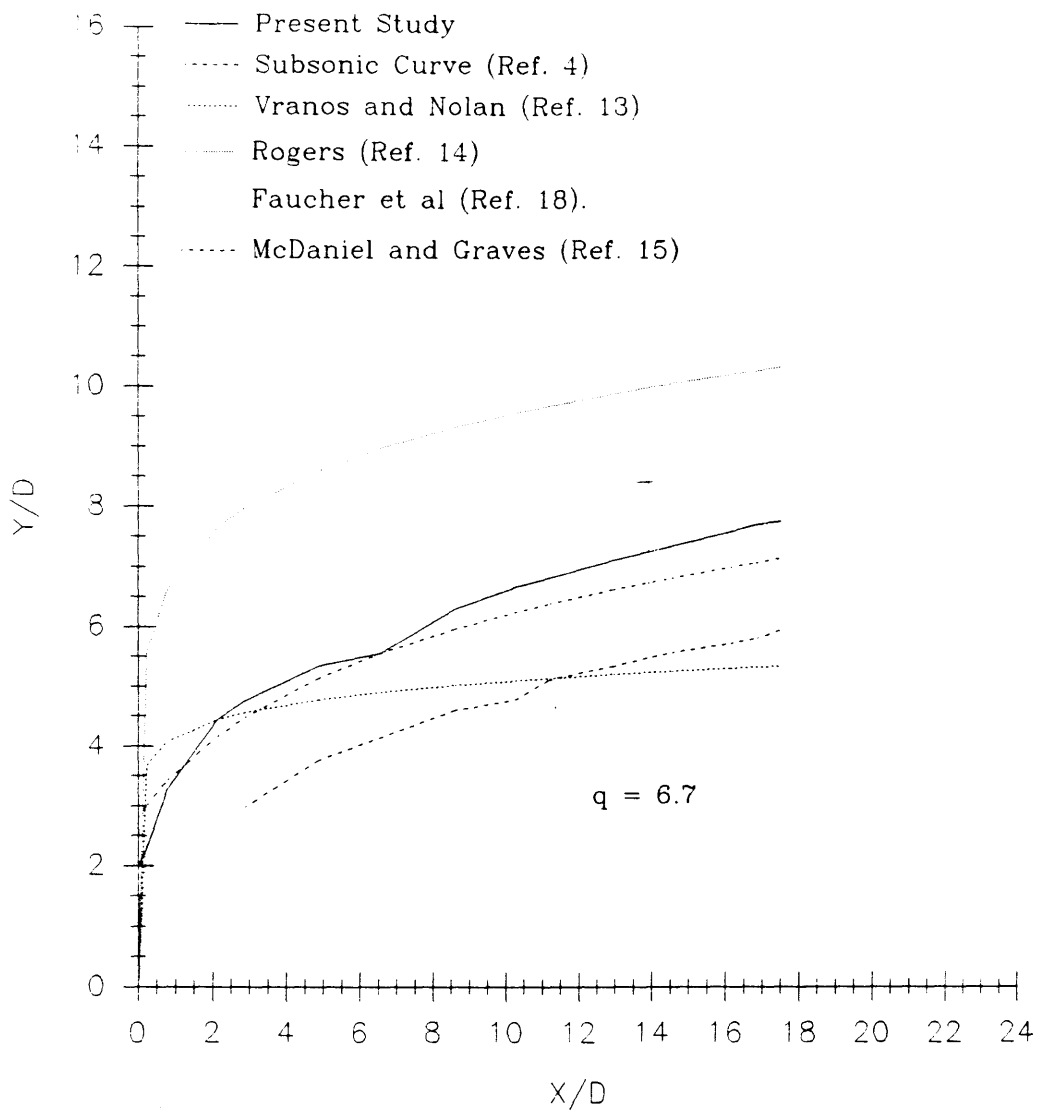

Figure 4-10: Measured Trajectories vs. Empirical Curves from Previous Research, q = 6.7, Measured Trajectory ±3%

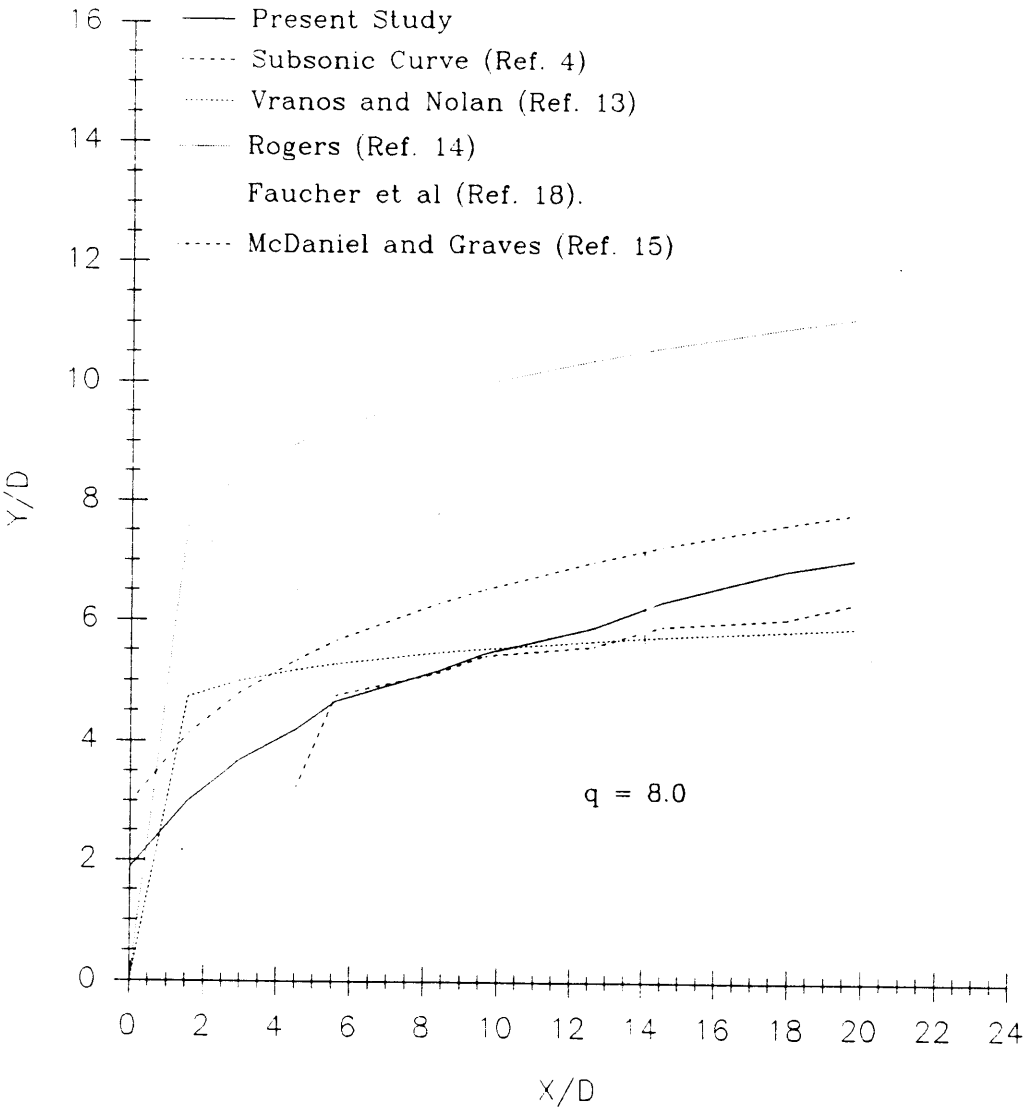

Figure 4-10 (continued), q = 8.0

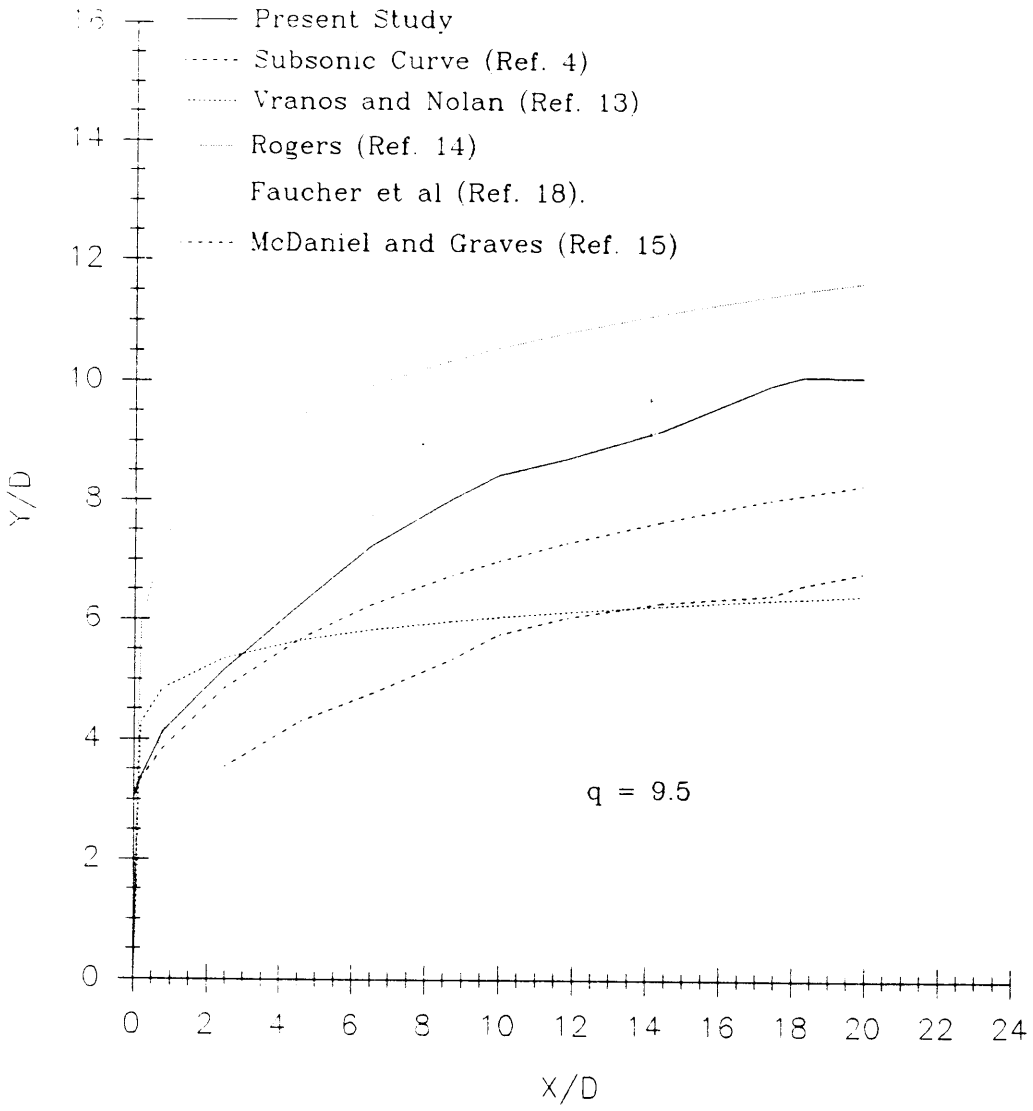

Figure 4-10 (continued), $q = 9.5$

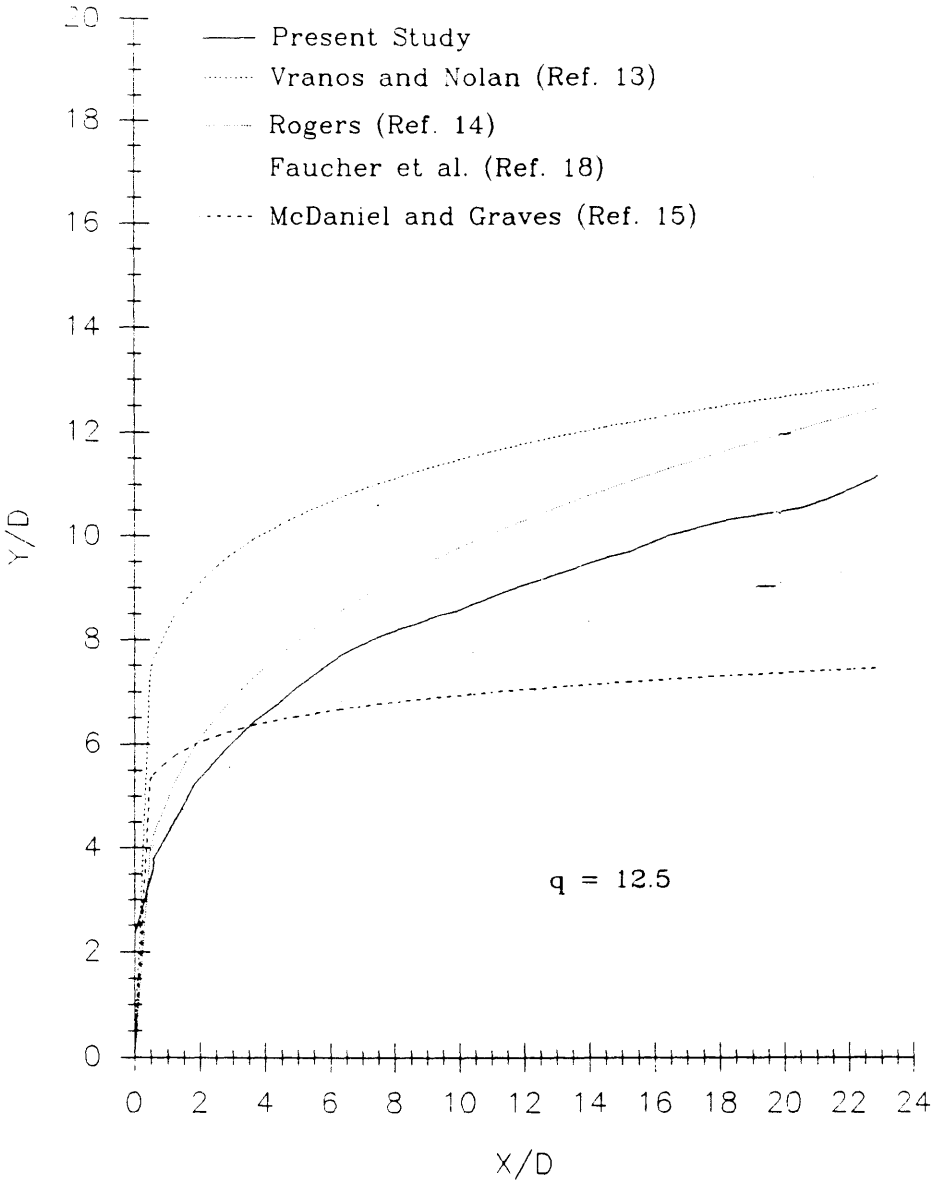

Figure 4-10 (continued), $q = 12.5$

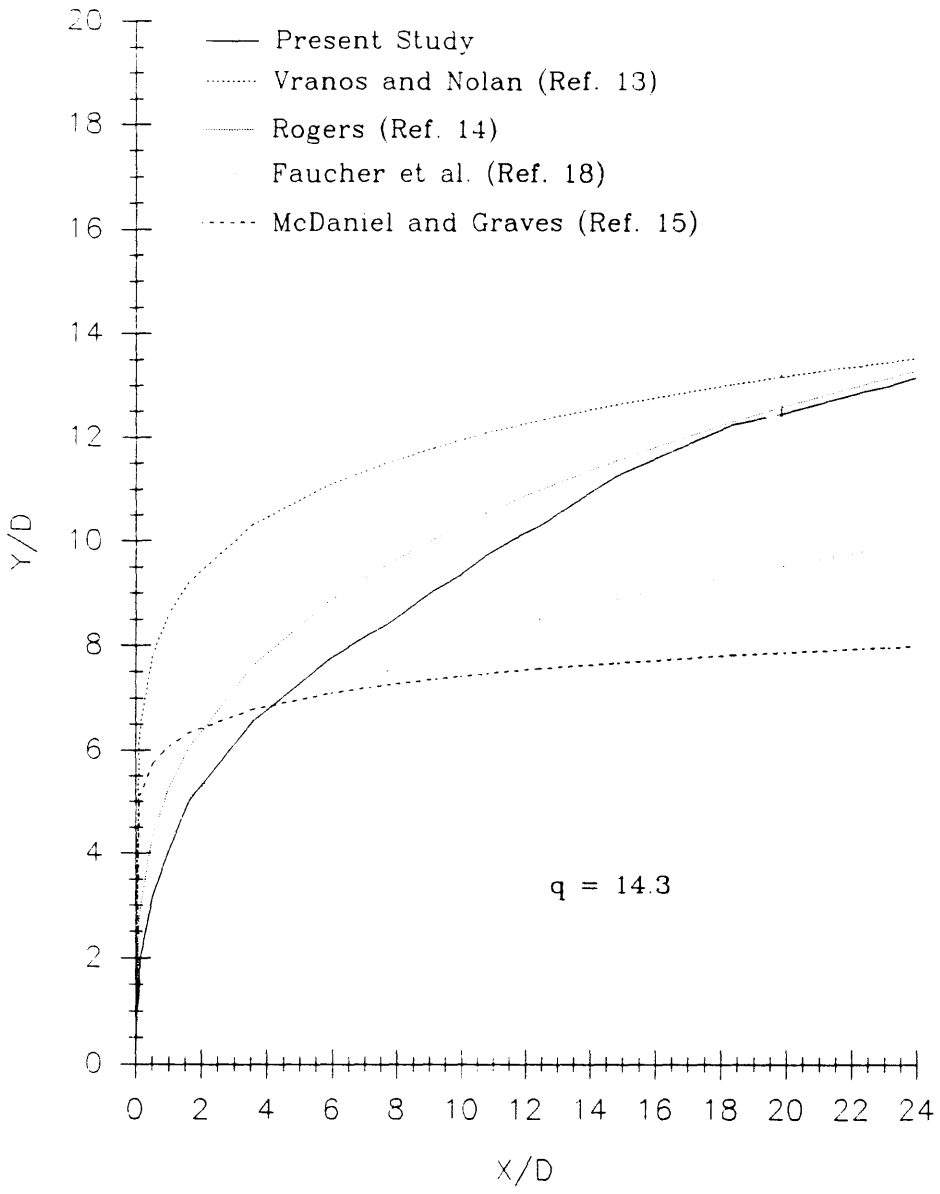

Figure 4-10 (continued), $q = 14.3$

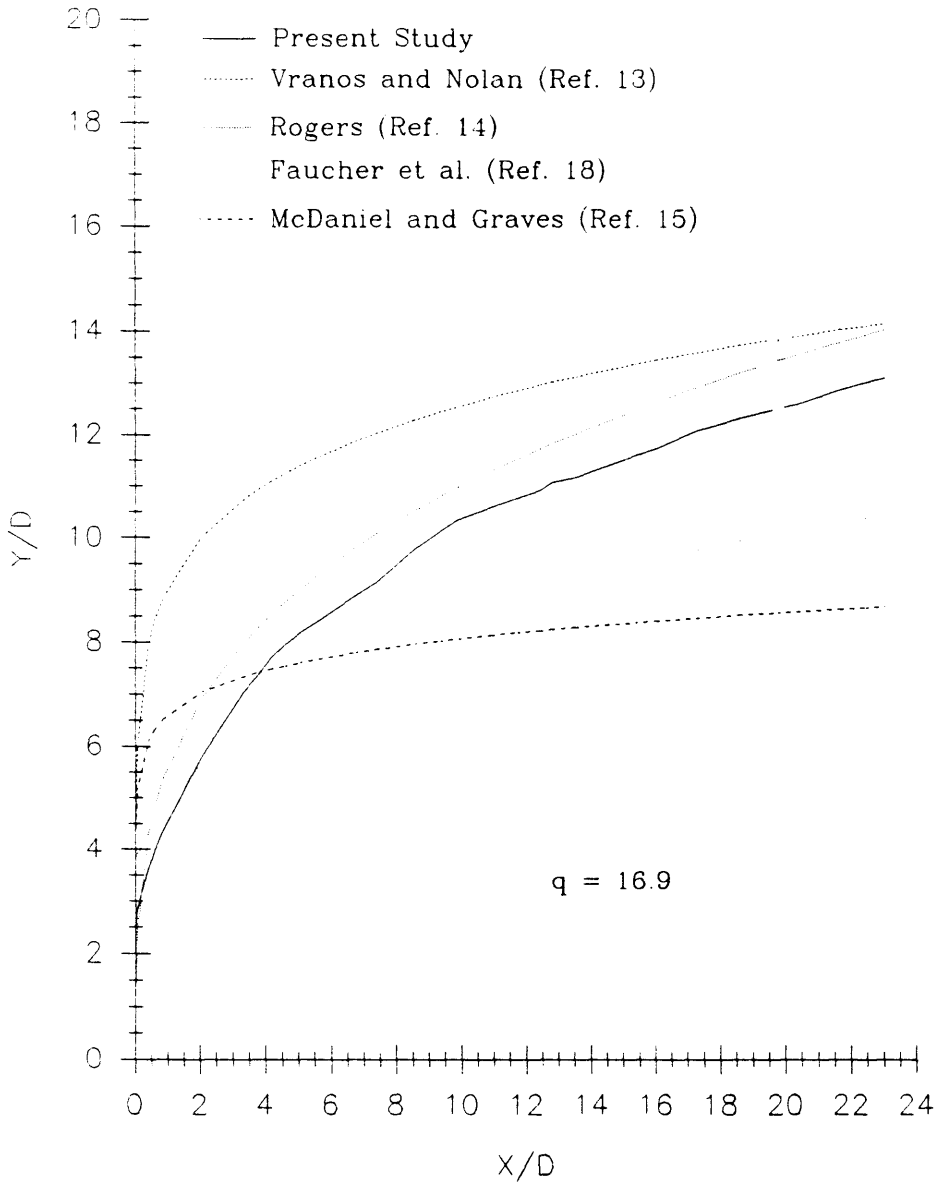

Figure 4-10 (continued), $q = 16.9$

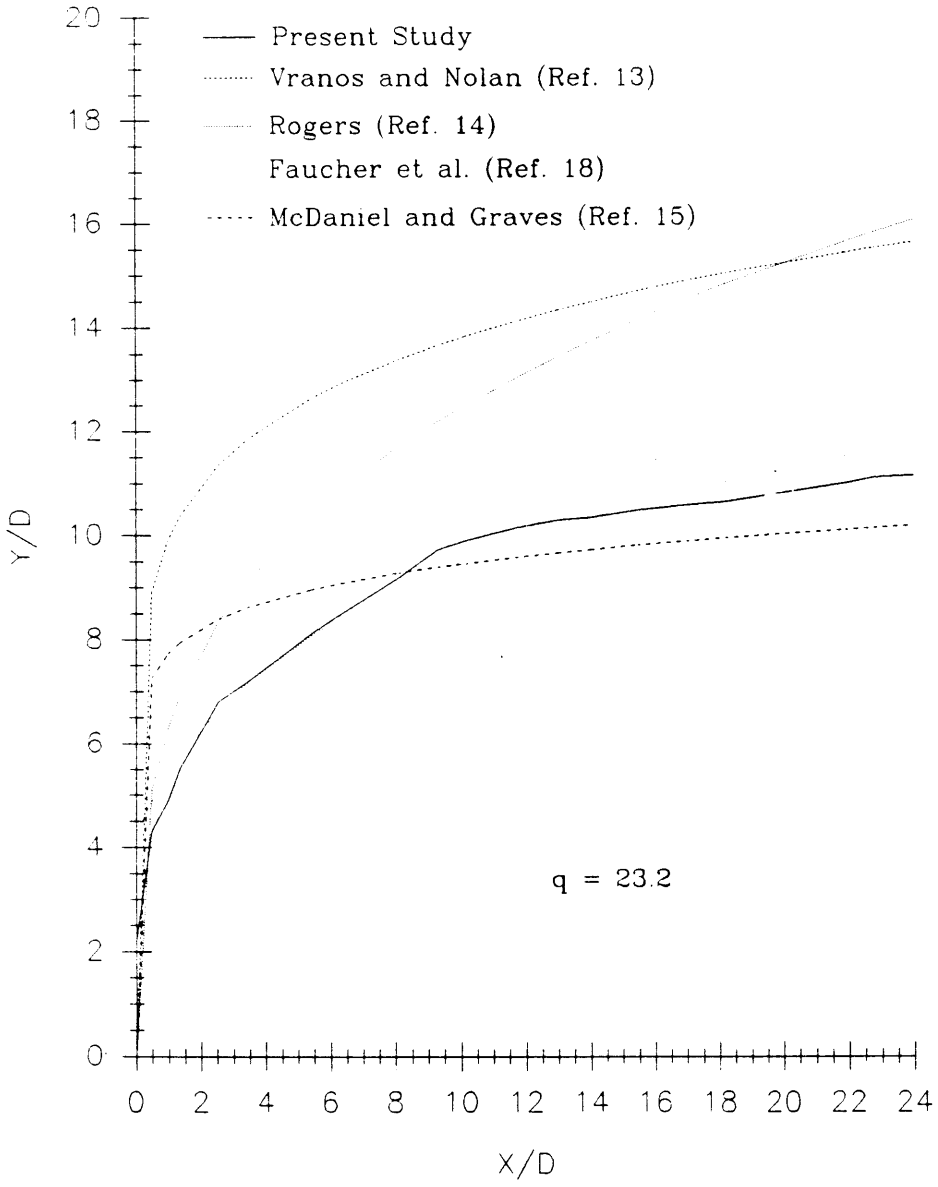

Figure 4-10 (continued), $q = 23.2$

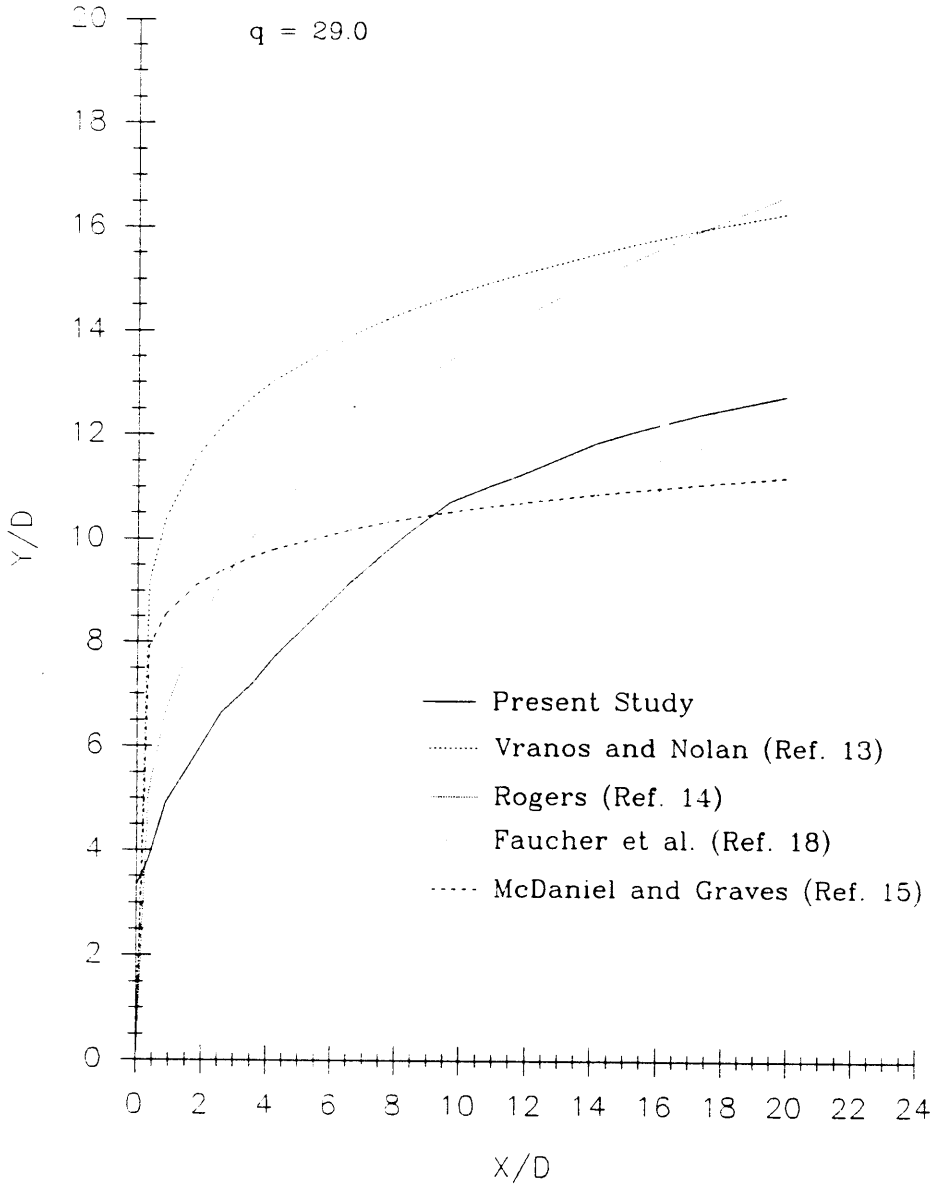

Figure 4-10 (continued), q = 29.0

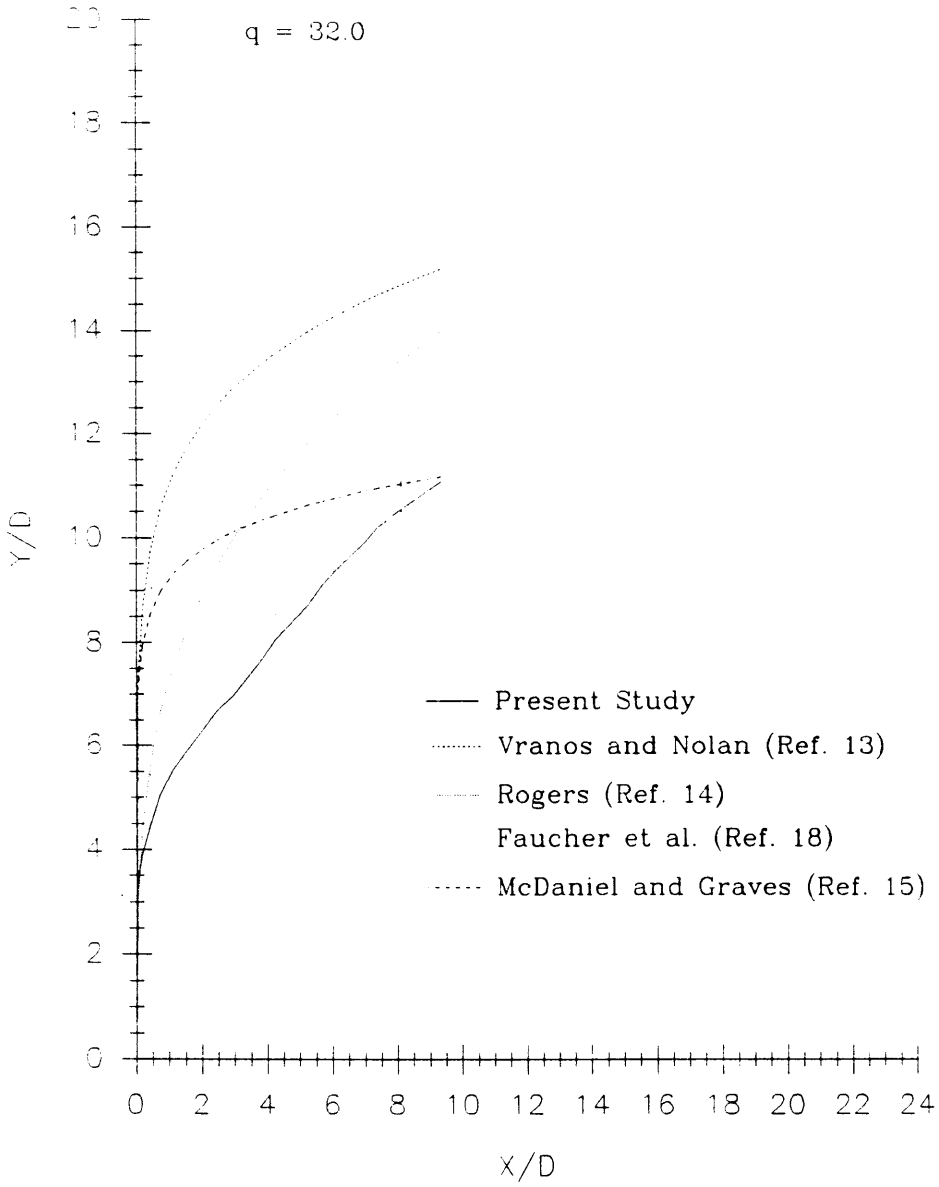

Figure 4-10 (continued), q = 32.0

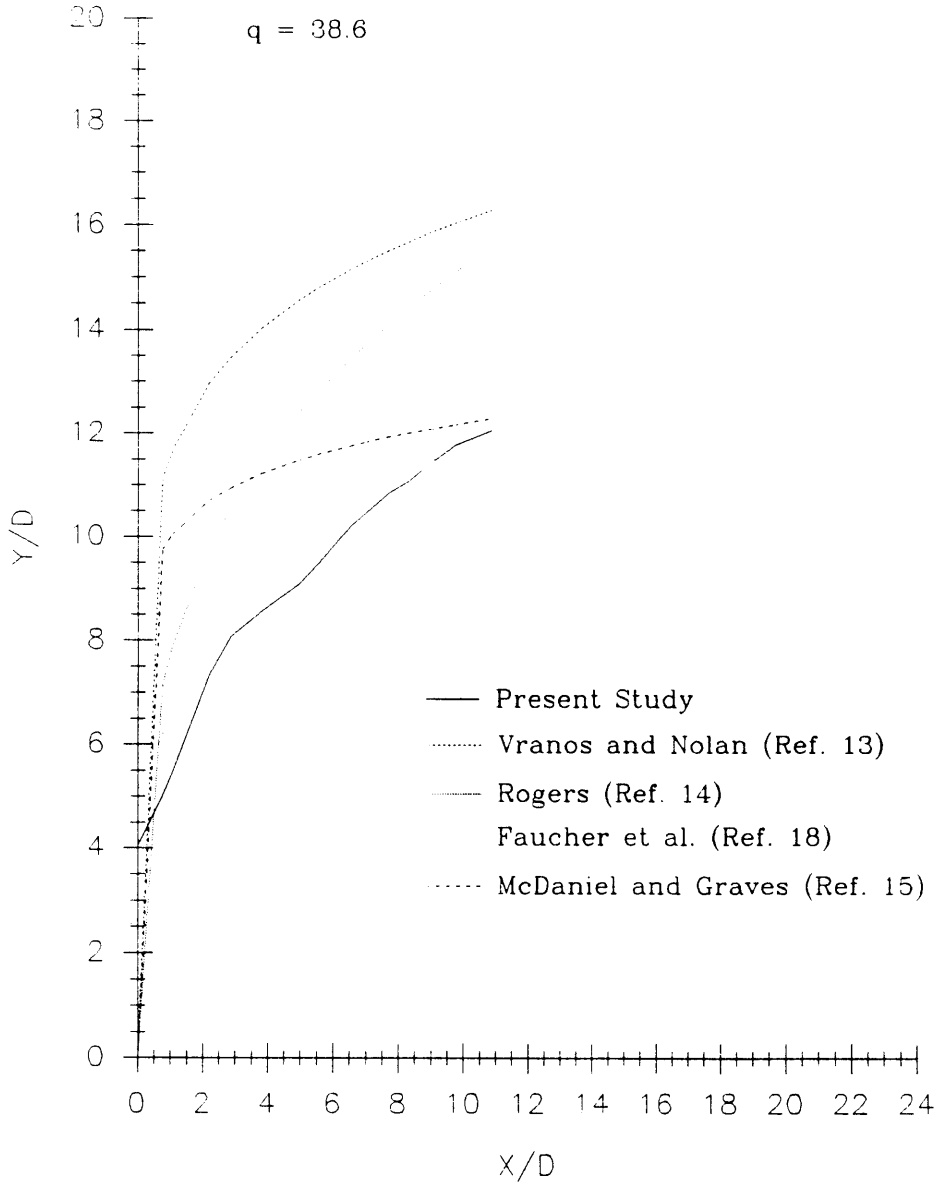

Figure 4-10 (continued), $q = 38.6$

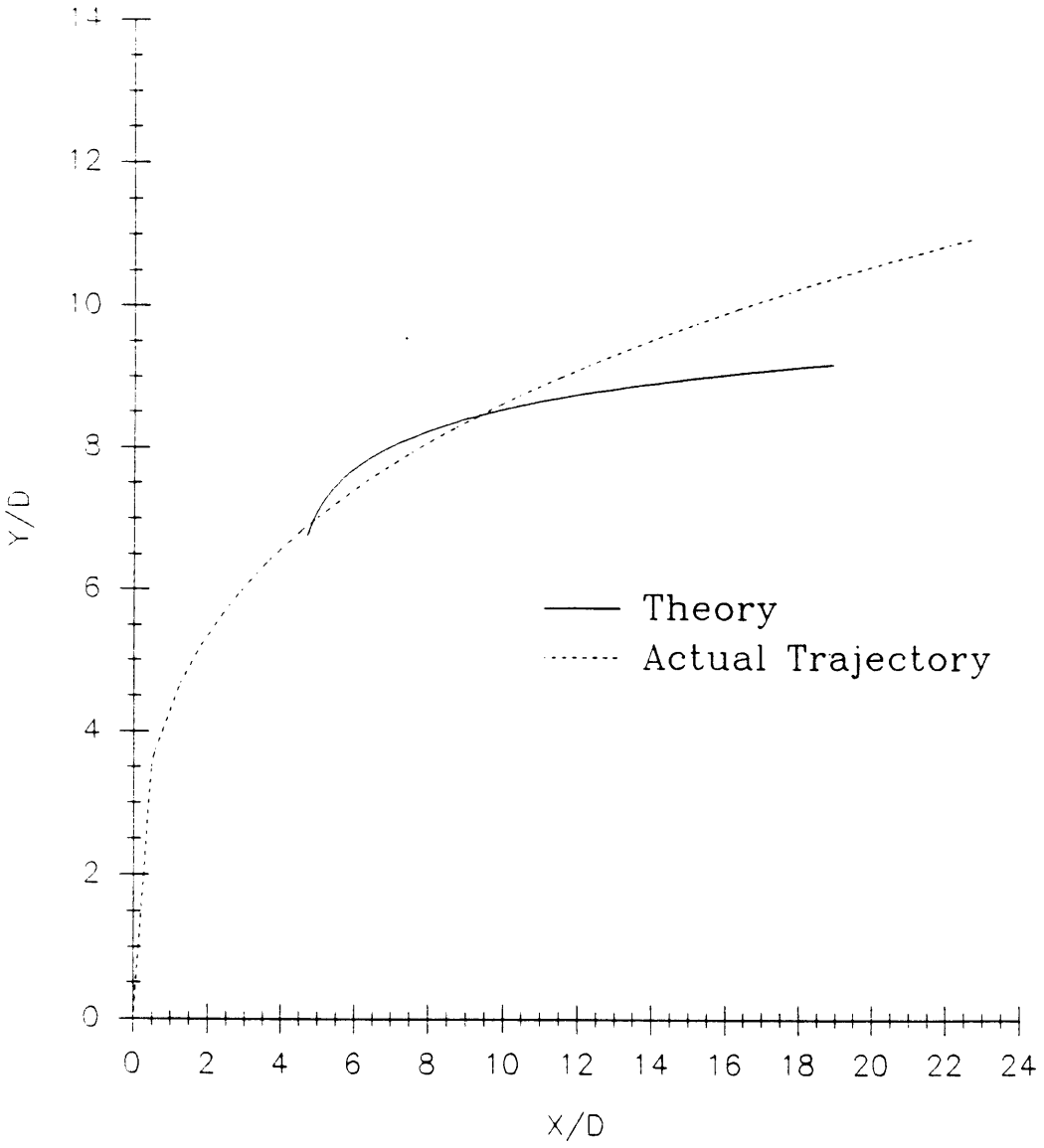

Figure 4-11: Theoretical vs. Actual Trajectory (±3%)

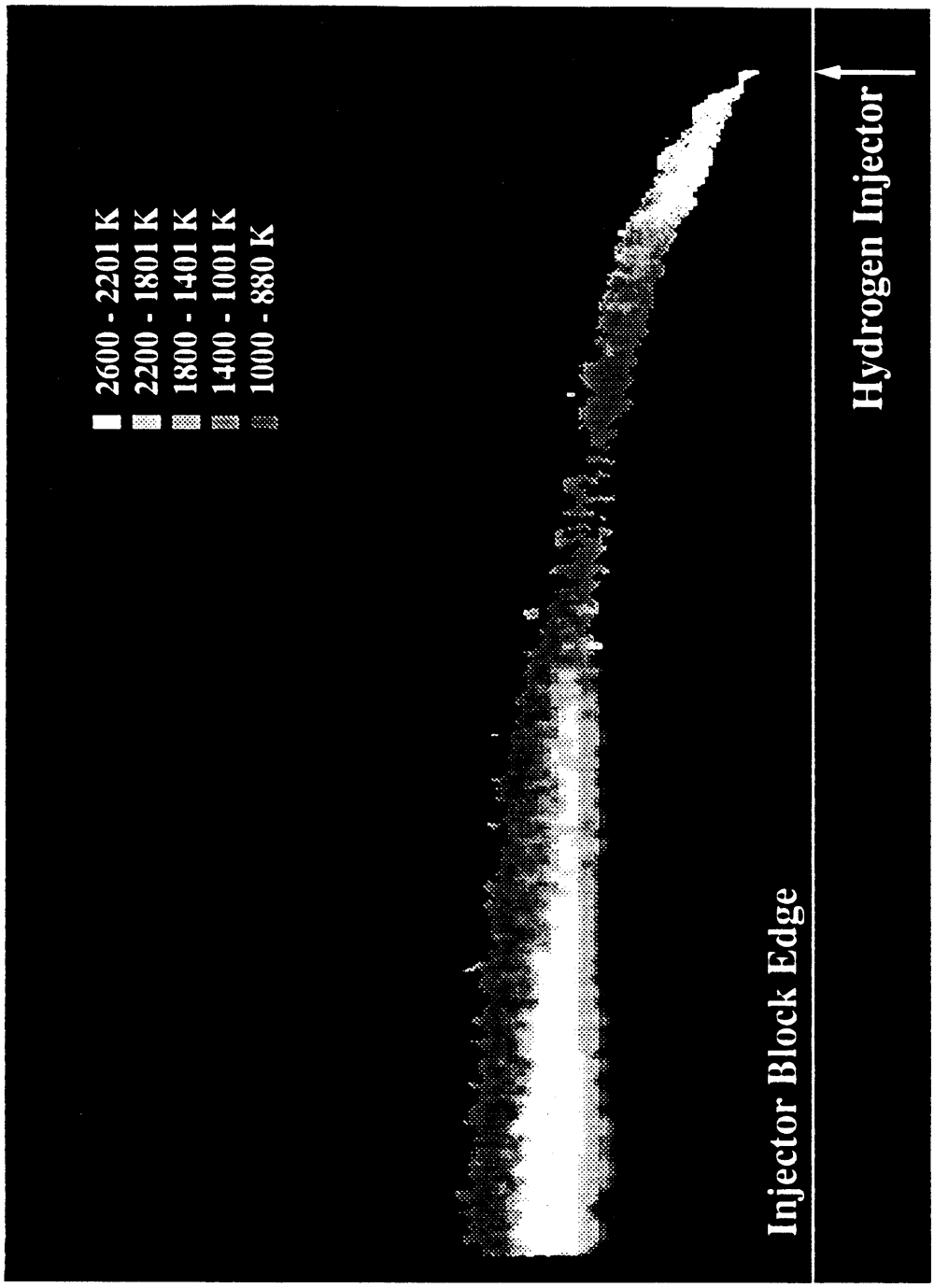

Figure 4-12: Grey Scale Image of the Temperature Distribution in the Entire Combustion Region, P_{H2}=700 torr, P_{FS}=26 torr

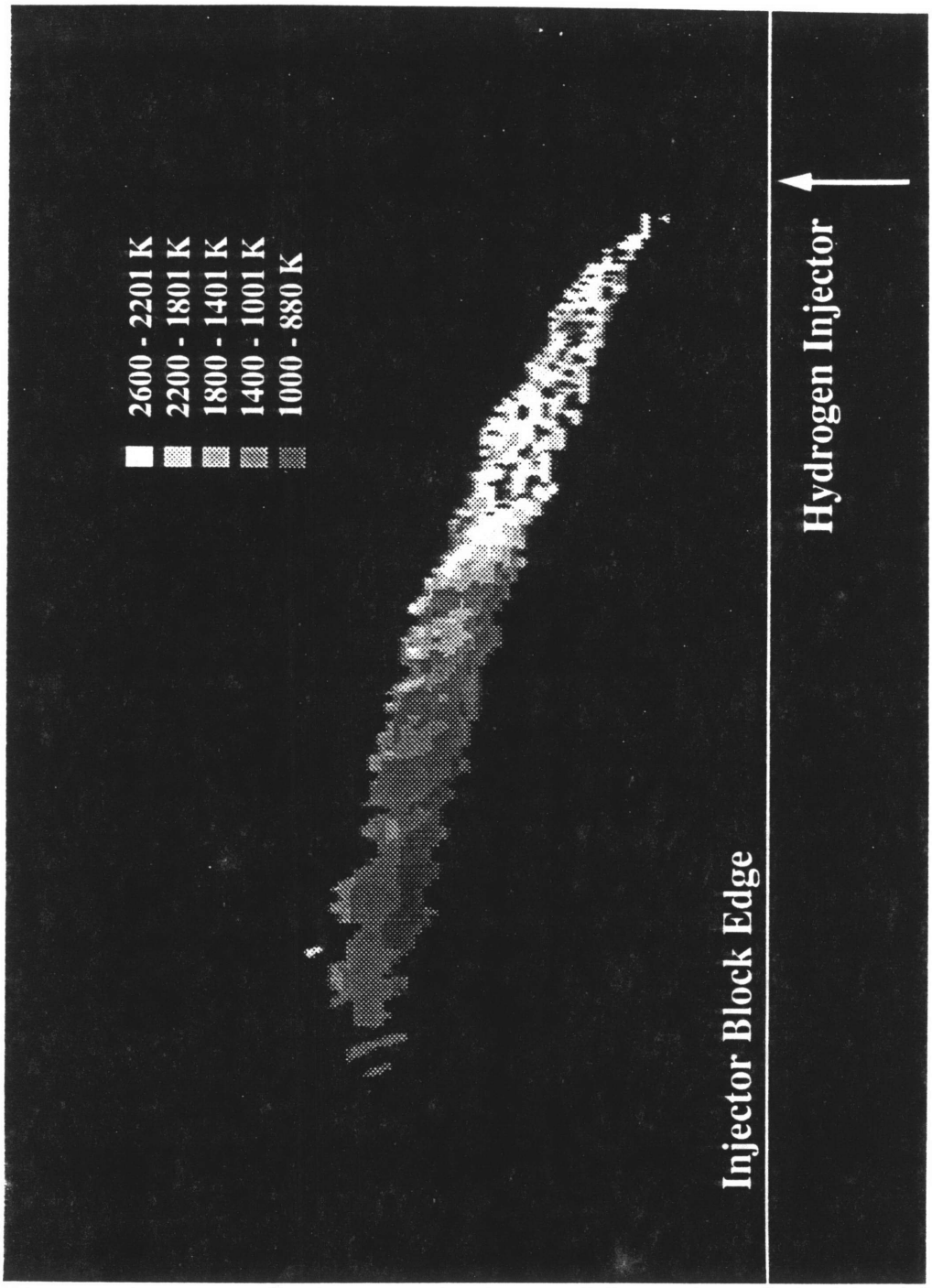

Figure 4-13: Grey Scale Image of the Temperature Distribution in the Combustion Region Close to the Injection Orifice. P_{H2}=700 torr, P_{FS}=26 torr

Appendix A

Error Analysis

There are two measurements done for the current study in which there is uncertainty. There was a pressure drop of about 10% in the hydrogen injection pressure over the course of the 0.5 sec injection pulse. This measurement is used in determining q. The digitizing of the PLIF image and the subsequent translation from the image dimensions to physical distance measurements also has some uncertainty. The former of these two errors does not affect the measured jet trajectories. It does influence the accuracy of the empirical curve fits however. The error in the physical measurements (the digitizing process) is estimated have an error of 1%. Converting the image dimensions to x/d_i and y/d_i values is assumed to be accurate to within 2%.

The affect that the 10% uncertainty in q has on the predicted trajectories can be analyzed as follows: in the equation,

$$\frac{y}{d_i} = 2.173 q^{0.276} \left(\frac{x}{d_i}\right)^{0.281}, \tag{A.1}$$

the two source of uncertainty are the values of q and x/d_i. The error in $y/d_i, \sigma_{y/d}$, can be written as,

$$\sigma_{y/d} = \left[\left(\frac{\partial(y/d_i)}{\partial q}\sigma_q\right)^2 + \left(\frac{\partial(y/d_i)}{\partial(x/d_i)}\sigma_{x/d_i}\right)^2\right]^{\frac{1}{2}}, \tag{A.2}$$

where σ_z denote the uncertainty in the variable z.

The free stream pressure is known to ± 2 torr, but the jet pressure dropped by 10% over the course of the 0.5 sec injection pulse. Because the PLIF images could have been taken anytime during the 0.5 sec pulse, the jet pressure (and hence q) can only be determined to within 10%. It is estimated that x/d_i is known to within ± 0.5. With these assumptions, and at $x/d_i = 20$, the above equation yields an

error in y/d_i between 0.2 and 0.3 (for the various values of q). The same type of analysis can be done on the logarithmic equation form, resulting in errors of comparable size.

Appendix B

Supersonic Nozzle Modelled as a Volume Varying with Time

The gas is accelerated from $\approx$ 10 m/s (in the stagnation region) to Mach 1 at the nozzle's throat. The inlet area is 0.9516 cm^2 and the throat area is 0.3696 cm^2. The speed of sound at the throat is found (by using $a = \sqrt{\gamma RT}$) to be 871.8 m/s (with a static temperature at the throat of 1688 K). The distance between the inlet and the throat is 1.143 cm.

The exit area of the nozzle is 0.4774 cm^2, and there is 1.905 cm between the throat of the nozzle and the exit plane. The speed of sound at the exit is 714.3 m/s, and the isentropic Mach number is 1.71. All of the walls in the nozzle (both the subsonic and the supersonic sections) are straight.

Using the assumption that,

$$\frac{d(Vol)}{dt} = A(x)\frac{dx}{dt}, \tag{B.1}$$

where $A(x)$ is the area as a function of downstream distance. $A(x)$ is easily found from the geometry of the nozzle, and dx/dt is assumed to vary linearly between the three stations at which it is known. The velocity was thus approximated by the following equations:

$$v = \begin{cases} 1000 + 3.3 \times 10^9 t & \text{for } t \leq 2.6 \times 10^{-5} \text{ sec} \\ 3.596 \times 10^4 + 1.97 \times 10^9 t & \text{for } t > 2.6 \times 10^{-5} \text{ sec.} \end{cases} \tag{B.2}$$

Using these assumptions, the gas "reaches" the throat in 2.6×10^{-5} sec. The equations used for the

volume as a function of time were:

$$Vol = \begin{cases} [0.952 - 0.509(1000t + 1.7 \times 10^9 t^2)] \cdot \\ \quad (1000 + 3.3 \times 10^9 t) & t \leq 2.6 \times 10^{-5} \text{ sec} \\ [0.37 + 0.057(3.6 \times 10^4 t + 9.9 \times 10^8 t^2 - 1.6)] \cdot \\ \quad (3.6 \times 10^4 + 2.0 \times 10^9 t) & t > 2.6 \times 10^{-5} \text{ sec} \end{cases} \tag{B.3}$$

Appendix C

Temperature Calculating Computer Program

```
REM ******************************************************
REM *                  Variable list :                   *
REM *  Q_filename : the file in which the pixel          *
REM *     intensities from the fluorescence emitted      *
REM *     subsequent to exciting the Q line are stored   *
REM *     in decimal form                                *
REM *                                                    *
REM *  R_filename : equivalent to Q_filename, but        *
REM *     contains pixel intensities from the R line     *
REM *                                                    *
REM *  OUTPUT_filename : file to which the temperatures  *
REM *     (normalized to be displayed with only 256      *
REM *     grey levels) are output                        *
REM *                                                    *
REM *  i : counts the x position in the files (which     *
REM *     contains 696x240 pixels)                       *
REM *                                                    *
REM *  j : count the y position                          *
```

```
REM *
REM *  q : stores the current value of the pixel       *
REM *     intensity from the file Q_filename           *
REM *
REM *  r : store the current R_filename value          *
REM *
REM *  t : calculated temperature, from 3.4 in         *
REM *     Procedures section                           *
REM *
REM *  t_out : normalized temperature (to compress the *
REM *     temperature from up around 2000 down to      *
REM *     about 200 so that t_out can be read into the *
REM *     imaging software as pixel intensities) that  *
REM *     is printed to OUTPUT_filename                *
REM ************************************************


OPEN "I", #1, "Q_filename"
OPEN "I", #2, "R_filename"
OPEN "O", #3, "OUTPUT_filename"

FOR j = 0 to 239
  FOR i = 0 to 695

INPUT #1, q
INPUT #2, r

IF q<>0 AND r<>0 THEN
   t = 2615.4 / (ln(r/q) - 1.02)
ELSE t = 0
END IF
t_out = INT((t/11) + 0.5)
   PRINT #3, t_out;
  NEXT i
```

```
NEXT j

CLOSE #1
CLOSE #2
CLOSE #3

END
```

Bibliography

[1] A.C. Eckbreth, P.A. Bonczyk, and J.F. Verdieck. Combustion diagnostics by lasar Raman and fluorescence techniques. *Prog. Energy Combust. Sci.*, 5:253–322, 1979.

[2] J.A. Schetz and F.S. Billig. Penetration of gaseous jets injected into a supersonic stream. *J. Spacecraft*, 3(11):1658–1665, 1966.

[3] S. Hoerner. *Fluid Dynamic Drag.* publisher by author, 1958.

[4] G.N. Abramovich. *The Theory of Turbulent Jets*, chapter 12. Massachusetts Institute of Technology Press, 1963. Sect. 4.

[5] R.C Orth, J.A. Schetz, and F.S. Billig. *The Interaction and Penetration of Gaseous Jets in Supersonic Flow.* Technical Report CR-1386, NASA, 1969. John Hopkins Univ., Applied Physics Laboratory.

[6] F.S. Billig, R.C. Orth, and M. Lasky. A unified analysis of gaseous jet penetration. *AIAA J.*, 9(6):1048–1058, 1971.

[7] J.A. Schetz, R.A. Weinraub, R.E. Mahaffey, and Jr. Supersonic transverse injection into a supersonic stream. *AIAA J.*, 6(5):933–934, 1968.

[8] J.A. Schetz, P.F. Hawkins, and H. Lehman. Structure of highly underexpanded trasverse jets in a supersonic stream. *AIAA J.*, 5(5):882–884, 1967.

[9] S. Crist, P.M. Sherman, and D.R. Glass. Study of the highly underexpanded sonic jet. *AIAA J.*, 4(1):68–71, 1966.

[10] J.A. Schetz, H.E. Gilreath, and S.C. Lubard. Fuel injection and mixing in a supersonic stream. In *12th Symposium (International) on Combustion*, pages 1141–1149, The Combustion Institute, Pittsburgh, Pennsylvania, 1969.

[11] L.S. Cohen, L.J. Coulter, W.J. Egan, and Jr. Penetration and mixing of multiple gas jets subjected to a cross flow. *AIAA J.*, 9(4):718–724, 1970.

[12] E.E. Zukoski and F.W. Spaid. Secondary injection of gases into a supersonic flow. *AIAA J.*, 2(10):1689–1696, 1964.

[13] A. Vranos and J.J. Nolan. Supersonic mixing of a light gas and air. In *AIAA Joint Propulsion Specialists Conference*, Colorado Springs, Colorado, 1965.

[14] R.C. Rogers. *A Study of the Mixing of Hydrogen Injected Normal to a Supersonic Airstream.* Technical Report TN D-6114, NASA, Hampton, Virginia, March 1971. Langley Research Center.

[15] J.C. McDaniel, J. Graves, and Jr. Laser-induced-fluorescence visualization of transverse gaseous injection in a nonreacting supersonic combustor. *J. Propulsion*, 4(6):591–597, 1988.

[16] D. Papamoschou, D.G. Hubbard, and M. Lin. *Observations of Supersonic Transverse Jets.* Technical Report AIAA paper no. 91-1723, Honolulu, Hawaii, June 1991. AIAA 22nd Fluid Dynamics, Plasma Dynamics, & Lasers Conference.

[17] S.D. Heister and A.R. Karagozian. Gaseous jet in supersonic crossflow. *AIAA Journal*, 28(5):819–827, 1990.

[18] J.E. Faucher Jr., S. Goldstein, and E. Tabach. *Supersonic Combustion of Fuels Other than Hydrogen for Scramjet Application.* Technical Report AFAPL-TR-67-12, US Air Force, 1967.

[19] H. Wilhelmi, J.P. Baselt, and K. Beir. Experiments on the propogation of mixing and combustion injecting hydrogen transversely into hot supersonic streams. In *14th Symposium (International) on Combustion*, pages 585–593, The Combustion Institute, Pittsburgh, Pennsylvania, 1975.

[20] K. Beir, G. Kappler, and H. Wilhelmi. Experiments on the combustion of hydrogen and methane injected transversely into a supersonic air stream. In *13th Symposium (International) on Combustion*, pages 675–682, The Combustion Institute, Pittsburgh, Pennsylvania, 1973.

[21] M.P. Lee, B.K. McMillin, J.L. Palmer, and R.K. Hanson. *Two-Dimensional Imaging of Combustion Phenomena in a Shock Tube Using Planar-Laser Induced Fluorescence.* Technical Report AIAA paper no. 91-0460, Reno, Nevada, January 1991. 29th Aerospace Sciences Meeting.

[22] M. Takahashi and A.K. Hayashi. *Numerical Study on Mixing and Combustion of Injecting Hydrogen Jet in a Supersonic Air Flow.* Technical Report AIAA paper no. 91-0574, Reno, Navada, January 1991. 29th Aerospace Sciences Conference.

[23] M. Mao, D.W. Riggins, and C.R. McClinton. *Numerical Simulation of Transverse Fuel Injection.* Technical Report NASP Contractor Report 1089, NASA, Hampton, Virginia, May 1990. Analytical Services & Materials, Inc.

[24] R.K. Hanson. Planar laser-induced fluorescence imaging. *J. of Quant. Spectrosc. Radiat. Transfer*, 40(3):343–362, 1988.

[25] G. Kychakoff, P.H. Paul, I van Cruyningen, and R.K. Hanson. Technical Report WSS/CI 86-15, The Combustion Institute, Tuson, Arizona, 1986.

[26] R.K. Hanson, J.M. Seitzman, and P.H. Paul. Planar laser-fluorescence imaging of combustion gases. *Applied Physics B*, 50:441–454, 1990.

[27] Katharina Kohse-Hoinghaus. Quantitative laser-induced fluorescence: some recent developments in combustion diagnostics. *Appl. Phys. B*, 50:455–461, 1990.

[28] J.W. Daily. Use of rate equations to describe laser excitation in flames. *Applied Optics*, 16(8):2322–2327, 1977.

[29] A. Yariv. *Quantum Electronics.* Wiley, New York, 1975.

[30] W. Demtroder. *Laser Spectroscopy.* Springer, Berlin, 1982.

[31] A.C. Eckbreth. *Laser Diagnostics for Combustion Temperature and Species.* Abacus Press, Cambridge, Massachusetts, 1988.

[32] E.H. Piepmeier. Theory of laser-saturated atomic resonance fluorescence. *Spectrochimica Acta*, 27B:431–443, 1972.

[33] R.P. Lucht, D.W. Sweeney, and N.M. Laurendeau. Balanced cross-rate model for saturated molecular fluorescence in flames using a nanosecond pulse length laser. *Applied Optics*, 19:3295–3300, 1980.

[34] J.O. Berg and W.L. Shackleford. Rotational redistribution effect on saturated laser-induced fluorescence. *Applied Optics*, 18(13):2093–2094, 1979.

[35] A.P. Baronavski and J.R. McDonald. Application of saturation spectroscopy to the measurement of C_2,$^3\,\Pi_u$ concentrations in oxy-acetylene flames. *Applied Optics*, 16:2093–2094, 1977.

[36] P. Anderson, A. Bath, W. Groger, H.W. Lulf, G. Meijer, and J.J. ter Meulen. Laser-induced fluorescence with tunable excimer lasers as a possible method for instantaneous temperature field

measurements at high pressures: checks with an atmospheric flame. *Applied Optics*, 27(2):365–378, 1988.

[37] D. Stepowski and M.J. Cottereau. Direct measurement of OH local concentration in a flame from the fluorescence induced by a single pulse. *Applied Optics*, 18:354–356, 1979.

[38] N.S. Bergano, P.A. Jaanimagi, M.M. Salour, and J.H. Bechtel. Picosecond laser-specroscopy measurements of hydroxyl fluorescence lifetime in flames. *Optics Letters*, 8:443–445, 1983.

[39] N.L. Garland and D.R. Crosley. On the collisional quenching of electronically excited OH, NH, and CH in flames. In *21st Symposium (International) on Combustion*, pages 1693–1702, The Combustion Institute, Pittsburgh, Pennsylvania, 1986.

[40] R.J. Cattolica and S.R. Vosen. In *20th Symposium (International) on Combustion*, pages 1273–1282, The Combustion Institute, Pittsburgh, Pennsylvania, 1984.

[41] K. Kohse-Hoinghaus, P. Koczar, and T.H. Just. Absolute concentration measurements of OH in low-pressure hydrogen-oxygen, methane-oxygen, and acetylene-oxygen flames. In *21st Symposium (International) on Combustion*, pages 1719–1727, The Combustion Institute, Pittsburgh, Pennsylvania, 1986.

[42] K. Kohse-Hoinghaus, R. Heidenreich, and T.H. Just. Determination of absolute OH and CH concentrations in a low pressure flame by laser-induced saturated fluorescence. In *20th Symposium (International) on Combustion*, pages 1177–1185, The Combustion Institute, Pittsburgh, Pennsylvania, 1984.

[43] D. Stepowski and M.J. Cottereau. Study of OH-saturated laser-induced fluorescence in low-pressure flame. In , Poitiers, France, July 1983. 9th ICODERS conference.

[44] R.P. Lucht, D.W. Sweeney, and N.M. Laurendeau. Laser-saturated fluorescence measurements of OH concentrations in flames. *Combustion and Flame*, 50:189–205, 1983.

[45] M.C. Drake, R.W. Pitz, M. Lapp, C.P. Fenimore, R.P. Lucht, D.W. Sweeney, and N.M. Laurendeau. Measurements of superequilibrium hydroxyl concentrations in turbulent nonpremixed flames using saturated fluorescence. In *20th Symposium (International) on Combustion*, pages 327–335, The Combustion Institute, Pittsburgh, Pennsylvania, 1984.

[46] R.P. Lucht, D.W. Sweeney, and N.M. Laurendeau. Laser-saturated fluorescence measurements of OH in atmospheric pressure $CH_4/O_2/N_2$ flames under sooting and non-sooting conditions. *Combution Science and Technology*, 42:259–281, 1985.

[47] T. Ni-Imi, T. Fujimoto, and N. Shimizu. Method for planar measurement of temperature in compressible flow using two-line laser-induced iodine fluorescence. *Optics Letters*, 15(16):918–920, 1990.

[48] B.K. McMillin, J.L. Palmer, and R.K. Hanson. *Two-Dimensional Temperature Measurements of Shock Tube Flows Using Planar Laser-Induced Fluorescence Imaging of Nitric Oxide.* Technical Report AIAA paper no. 91-1670, Honolulu, Hawaii, June 1991. AIAA 22nd Fluid Dynamics, Plasma Dynamics, & Lasers Conference.

[49] P.H. Paul and R.K. Hanson. *Application of Planar Laser-Induced Fluorescence to Reacting Flows.* Technical Report AIAA paper no. 90-1848, Orlando, Fl, July 1990. 26th Joint Propulsion Conference.

[50] R.A. Copeland, M.J. Dyer, and D.R. Crosley. Rotational level dependent quenching of $A^2\Sigma^+$OH and OD. *J. of Chemical Physics*, 82:4022, 1985.

[51] N.M. Laurendeau. *Progress in Energy and Combustion Science*, 14:147–170, 1988.

[52] A. C. Eckbreth. Recent advances in laser diagnostics for temperature and species concentration in combustion. In *18th Symposium (International) on Combustion*, pages 1471–1487, The Combustion Institute, Pittsburgh, Pennsylvania, 1981.

[53] M.B Long, B.F. Webber, and R.K. Chang. Instantaneous two-dimensional concentration measurements in a jet flow by Mie scattering. *Appl. Phys. Lett.*, 34(1):22–24, 1979.

[54] M.C. Escoda and M.B. Long. Rayleigh scattering measurements of the gas concentration field in turbulent jets. *AIAA J.*, 21(1):81–84, 1983.

[55] M. Aldén, H. Edner, G. Holmstedt, S. Svanberg, and T. Hogberg. Single-pulse laser-induced OH fluorescence in an atmospheric flame, spatially resolved with a diode array detector. *Applied Optics*, 21(7):1236–1240, 1982.

[56] M.J. Dyer and D.R. Crosley. Two-dimensional imaging of OH laser-induced fluorescence in a flame. *Optics Letters*, 7(8):382–384, 1982.

[57] G. Kychakoff, R.D. Howe, R.K. Hanson, and J.C. McDaniel. Quantitative visualization of combustion species in a plane. *Applied Optics*, 21(8):3225–3227, 1982.

[58] L.A. Melton and J.F. Verdieck. Vapor/liquid visualization for fuel sprays. *Combust. Sci. and Tech.*, 42:217–222, 1985.

[59] M. Allen, K. Donohue, and S. Davis. *Species and Temperature Imaging in Liquid-Fueled Spray Flames.* Technical Report AIAA paper no. 90-2440, Orlando, Florida, July 1990. 26th Joint Propulsion Conference.

[60] G. Kychakoff, R.K. Hanson, and R.D. Howe. Simultaneous multiple-point measurements of OH in combustion gases using planar laser-induced fluorescence. In *20th Symposium (International) on Combustion*, pages 1265–1272, The Combustion Institute, Pittsburgh, Pennsylvania, 1984.

[61] J.B. Jefferies, R.A. Copland, G.P. Smith, and D.R. Crosley. Multiple species laser-induced fluorescence in flames. In *21st Symposium (International) on Combustion*, pages 1709–1718, The Combustion Institute, Pittsburgh, Pennsylvania, 1986.

[62] M.P. Lee, P.H. Paul, and R.K. Hanson. Laser-fluorescence imaging of O_2 in combustion flows using an ArF laser. *Optics Letters*, 11(1):7–9, 1986.

[63] G.S. Diskin, W.R. Lempert, and R.B. Miles. *Species and Velocity Visualization of Unseeded Heated Air and Combustion Hydrogen Jets Using Laser and Flashlamp Source.* Technical Report AIAA paper no. 90-1849, Orlando, Fl, July 1990. 26th Joint Propulsion Conference.

[64] P.H. Paul. *The Application of Intensified Array Detectors to Quantitative Planar Laser-Induced Fluorescence Imaging.* Technical Report AIAA paper no. 91-2315, Sacramento, Ca, June 1991. 27th Joint Propulsion Conference.

[65] P.H. Paul, I. van Cruyningen, R.K. Hanson, and G. Kychakoff. High resolution digital flowfield imaging of jets. *Experiments in Fluids*, 9:241–251, 1990.

[66] D. Stepowski, D. Puechberty, and M.J. Cottereau. Use of laser-induced fluorescence of OH to study the perturbation of a flame by a probe. In *18th Symposium (International) on Combustion*, pages 1567–1574, The Combustion Institute, Pittsburgh, Pennsylvania, 1981.

[67] J.D. Abbitt, III, R.J. Hartfield, and J.C. McDaniel. *Mole Fraction Imaging of Transverse Injection in a Ducted Supersonic Flow.* Technical Report AIAA paper no. 89-2550, Monterey, California, July 1989. 25th Joint Propulsion Conference.

[68] J.C. Hermanson and M. Winter. *Imaging of a Transverse, Sonic Jet in Supersonic Flow.* Technical Report AIAA paper no. 91-2269, Sacremento, California, June 1991. 27th Joint Propulsion Conference.

[69] R.S. Barlow and A. Collignon. *Linear LIF Measurements of OH in Nonpremixed Methane-Air Flames: When Quenching Corrections Are Unnecessary.* Technical Report AIAA paper no. 91-0179, Reno, Nevada, January 1991. 29th Aerospace Sciences Meeting.

[70] J.F. Verdieck and P.A. Bonczyk. Laser-induced saturated fluorescence investigations of CH, CN, and NO in flames. In *18th Symposium (International) on Combustion*, pages 1559–1566, The Combustion Institute, Pittsburgh, Pennsylvania, 1981.

[71] M. Mailander. Determination of absolute transition probabilities and particle densities by saturated fluorescence excitation. *J. of Applied Physics*, 49:1256–1259, 1978.

[72] K. Kohse-Hoinghaus, W. Perc, and T Just. Laser-induced saturated fluorescence as a method for the determination of radical concentrations in flames. *Ber. Buns. Phys. Chem.*, 87:1052–1057, 1983.

[73] R.P. Lucht, D.W. Sweeney, and N.M. Laurendeau. Laser-saturated fluorescence measurements of OH concentrations in flames. *Comb. Flame*, 50:189–205, 1983.

[74] M. Allen, S. Davis, and K. Donohue. *Planar Measurements of Instantaneous Species and Temperature Distribution in Reacting Flows: A Novel Approach to Ground Testing Instrumentation.* Technical Report AIAA paper no. 90-2383, Orlando, Florida. July 1990. 26th Joint Propulsion Conference.

[75] J.M. Seitzmann, G. Kychakoff, and R.K. Hanson. Instantaneous temperature field measurements using planar laser-induced fluorescence. *Optics Letters*, 10(9):439–441, 1985.

[76] R.J. Hartfield Jr., S.D. Hollo, and J.C. McDaniel. Planar temperature measurements in compressible flows using laser-induced iodine fluorescence. *Optics Letters*, 16(2):106–108, 1991.

[77] B.K. McMillin, M.P. Lee, P.H. Paul, and R.K. Hanson. *Planar Laser-Induced Fluorescence Imaging of Nitric Oxide in a Shock Tube.* Technical Report AIAA paper no. 89-2566, Montery, California, July 1989. 25th Joint Propulsion Conference.

[78] J.L. Palmer, B.K. McMillin, and R.K. Hanson. *Planar Laser-Induced Fluorescence Imagaing of Underexpanded Free Jet Flow in a Shock Tunnel Facility.* Technical Report AIAA paper no. 91-1687, Honolulu, Hawaii, June 1991. 22nd Fluid Dynamics, Plasma Dymanics, & Lasers Conference.

[79] M.P. Lee, P.H. Paul, and R.K. Hanson. Quantitative imaging of temperature field in air using planar laer-induced fluorescence of O_2. *Optics Letters*, 12(2):75–77, 1986.

[80] R. Rhodes and D. Keefer. *Numerical Modeling of a RF Plasma in Argon.* Technical Report AIAA paper no. 88-0726, 1988.

[81] P.J. Wantuck and H. Watanabe. *Radio Frequency (RF) Heated Supersonic Flow Laboratory.* Technical Report AIAA paper no. 90-2469, Orlando, Florida, July 1990. 26th Joint Propulsion Conference.

[82] P.J. Wantuck and D.E. Hull. *Experimental Measurements in a Radio-Frequency Discharge Heated Supersonic Flow: Evaluation of a Potential Electric Propulsion Thruster.* Technical Report AIAA paper no. 91-3615, Cleveland, OH, September 1991. AIAA/NASA/OAI Conference on Advanced SEI Technologies.

[83] A.E. Lutz, R.J. Kee, and J.A. Miller. *SENKIN: A Fortran Program for Predicting Homogeneous Gas Phase Chemical Kinetics With Sensitivity Analysis.* Technical Report SAND87-8248, Sandia National Laboratories, Livermore, California, 1987.